SURFACE INTEGRITY IN DIAMOND MACHINING GERMANIUM FOR INFRARED OPTICS

by

Nicholas E. Sizemore

A dissertation submitted to the faculty of
The University of North Carolina at Charlotte
in partial fulfillment of the requirements
for the degree of Doctor of Philosophy in
Mechanical Engineering

Charlotte

2020

Approved by:

_____

Dr. Matthew A. Davies

_____

Dr. Christopher J. Evans

_____

Dr. Youxing Chen

_____

Dr. Thomas J. Suleski

ABSTRACT

NICHOLAS E. SIZEMORE. Surface integrity in diamond machining germanium for infrared optics. (Under the direction of DR. MATTHEW A. DAVIES)

Ultra-precision manufacturing is a deterministic method of producing optical-grade components. Continuous and interrupted machining operations are the main focus of this research with the goal of improving the manufacturing community's knowledge. The original contributions of this research are: (a) a comprehensive analysis of the cutting mechanics of single-crystal germanium, specifically studying the effects of major crystal orientation and cutting speed; (b) methodology for producing flat, damage-free test samples in single-crystal germanium; and (c) machine learning models for estimating surface finish parameters Sa, Sq, and Sz in SPDT of single-crystal germanium and oxygen-free high-conductivity copper. As a final product of this research, a pair of collimating lenses were produced for an external collaborator.

DEDICATION

I would like to dedicate this work to my wife, Jiang, and my brother, Christopher, who have supported me through graduate school. I could not have done this without them.

ACKNOWLEDGEMENTS

TABLE OF CONTENTS

LIST OF TABLES

LIST OF FIGURES

LIST OF ABBREVIATIONS

α Tool rake angle

Ω Spindle speed

a_{doc} Depth of cut

f_r Feed per revolution

R Tool nose radius.

S_o Stepover

Sa Average areal surface roughness

Sq Root mean squared areal surface roughness

Sz Peak-to-valley

t_c Chip thickness

V_c Cutting speed

v_f Feedrate

CHAPTER 1: Motivation and Background

Complexities in component design have driven the need for more deterministic higher- degree-of-freedom manufacturing processes. Ultra-precision machine tools have enabled production of advanced optical prescriptions that do not have a rotational axis of symmetry. [1][2][3]. Optics with such surfaces are known as freeform optics. Freeform optic design can greatly improve existing or new systems by combining the optical function of several classical axisymmetric optics into a single element. This allows simplification of optical systems, allowing for more compact, and lightweight designs that require less assembly. Multi-axis (>2 axes) techniques, such as coordinated-axis turning, milling, multi-axis flycutting, grinding, and MRF can be used to produce freeform surfaces.

Freeform optics are enabling significant innovations in imaging, surveillance, fiber optics, solar cells, and military defense applications [4][5]. Because of the more forgiving tolerances, IR systems may provide the most immediate opportunities for freeform optics. A brittle IR material that is extensively used in imaging and military defense systems is single-crystal germanium (Ge) which has been utilized as an IR lens material since the late 1940's [6]. Materials that are transmissive in the IR can be more difficult to machine due to their brittle nature and require a fundamental understanding of material behavior and cutting mechanics. Compared to the cutting mechanics of ductile metals, the behavior of brittle materials is not well understood. Particularly in high-speed machining, the behavior of brittle materials such as Ge still requires significant research. Improvements in productivity, tool life and surface quality by deterministic prediction of optimal machining parameters is a subject of current research [7][8]. Limited research on the high-speed machining of Ge exists [9]. In this

dissertation, new research into the cost-effective machining of Ge are presented for both continuous and interrupted cutting operations.

The use of Ge in IR applications stems from its high index of refraction ($\sim$4) and (ideally) isotropic optical properties. A high index of refraction leads efficient redirection of light as is demonstrated in the final chapter of this work in the machining of compact fast-axis collimators. However because of its mechanical material properties, production of optics in Ge requires ultra-precision machining. Freeform optics in particular require more complex geomtries that make machining and cutting mechanics more complex.

Ge has a diamond-cubic crystal structure that naturally resists the flow of dislocations. Glide or slip can occur on {111} plane in the <110> direction. Machining Ge can be described as brittle-dominated or ductile-dominated. For decades, our understanding of diamond turnable ductile and brittle materials has been the subject of many research studies [10][11][12][13][14][15][16][17][18][19]. Plastic flow in Ge has been at the center of the literature. Originally, it seemed impractical to machine Ge since there is a natural resistance to plastic deformation; however, if the scales are small enough, such as in diamond turning and micro-machining, ductile flow can occur [20]. Studies by Furukawa et al. [21], Blake et al. [22], and Nakasuji et al. [23] set the modern groundwork for understanding ductile-dominated machining of Ge and other brittle materials.

Two critical geometric properties of the tool in machining Ge are the rake angle (α) and the tool nose radius (R). These control material loading mechanics and chip geometry and make ductile-dominated machining a more favorable deformation mode. The rake angle (α) controls the hydrostatic pressure imposed by the tool on the deformation zone in single-point diamond turned (SPDT), milling, and flycutting. As α becomes more negative (-15, -25, -45), the compressive force increases and tensile force decreases. Several researchers have shown an increased compressive

force will suppress crack formation and reduce subsequent surface degradation due to fracture and pitting in diamond machining operations [10][24][25]. The radius R in combination with the depth of cut (a_{doc}) and feed per revolution (f_r) are the main contributors to defining the chip geometry. Because the transition from a surface free of fracture to one with significant fracture can occur over a small range of f_r, researchers postulated that there was a transition from ductile-to-brittle machining at a critical chip thickness at which an abrupt ductile-to-brittle transition occurs [24][26]. Realistically, the tool geometry is not constant, thereby making it difficult to describe a true point in the chip thickness that defines a brittle-to-ductile transition. More likely, the transition can occur over a range of machine parameters, and the transition begins to occur more gradually, first in the sub-surface which eventually is manifested in what appears to be a dramatic change in the surface character.

It has been postulated that phase transformations in Ge allow the apparently brittle material to deform plastically. Phase transformations occurring due to the compound effect of hydrostatic pressure and rapid loading/unloading during continuous machining operations could promote ductile-dominated behavior. Oliver et al. described rate-dependent phase transformation in nano-indentated Ge [27]. Several other studies support this observation in both Ge and silicon [28][29][30][31][32][33]. Of great interest for machining is the transformation from diamond cubic Ge (dc-Ge) to a the metallic β-tin phase. The β-tin metallic phase has a greater number of slip systems and thus could contribute to observed ductile behavior in machining. However, the β-tin phase is meta-stable and, thus, transforms back to dc-Ge and amorphous-Ge upon unloading. Deshmukh et al. described an explosive crystallization nature under mechanical impact driving the remaining transformation of β-tin Ge to dc-Ge [34]. Phase transformations could account for ductile-dominated material removal in both continuous and interrupted cutting operations.

Chemo-mechanical polishing Ge and other brittle IR materials is a well-known

method for producing low damage wafers and pucks. This research found that there was a lack of flat, damage-free commercially available Ge needed for diamond machining experiments. Most chemo-mechanically polished Ge is in wafer form and is used in the electronics industry. The wafers have controlled thickness but are thin and typically not "flat". Alternatively, diamond machining can be used to manufacture "flat" samples with controlled thickness, but the surfaces have machining-induced damage. A challenge of this research was that the experiments designed to study the damage induced in interrupted cutting required a surface that was both "flat" (to better than 100 nm) and damage-free.

To better understand the mechanics of machining, all previous damage induced into the workpiece should be removed prior to completing a cutting experiment. Of course, there is no such thing as a perfect lattice without disorder or imperfection. This research has set to produce flat, damage-free Ge through first single-point diamond turning and finishing with chemo-mechanical polishing. This method is then compared to others that use a combination of diamond turning and magneto-rheological finishing or only involved diamond turning. Thus, an ancillary result of the sample preparation undertaken in this research was the comparison of damage generated in diamond turning, MRF, and chemo-mechanical polishing.

To assist in the understanding of the mechanics of single-point diamond turning and polishing, methods such as confocal Raman and Rutherford Backscattering Spectroscopy (RBS) were used to evaluate subsurface disorder and damage. RBS and confocal Raman are common methods for characterizing lattice disorder within ductile and brittle materials [35][36][37]. Subsurface damage produced by single-point diamond turning is expected to be dependent on machining parameters. Lattice disorder in the form of residual stress (tension or compression) and dislocation formation is left in the wake of the diamond tool. Residual stress causes birefringence which can degrade optical performance [38]. Ge samples with final surface preparations from

single-point diamond turning, chemo-mechanical polishing, and magneto-rheological finishing were examined using both confocal Raman and RBS in the channeling configuration.

Because of the complexity of physically modeling the dependence on surface and subsurface characteristics on machining parameters, more complex modeling methods were investigated. Recently, data-driven models in engineering applications have demonstrated potential in predicting machine parameters. For instance, predicting surface roughness has shown improved accuracy over physics-based analytical or traditional statistical models [39] [40] [41]. Classic physics-based models require an in-depth understanding of the physical system to develop closed-form mathematical models or physics-based simulations. However, data-driven models do not require the same in-depth understanding of the physics. Data-driven models can also provide insight into the physics of material behavior by identifying links between parameters not previously suspected. It is necessary to have a fundamental understanding of the behavior of the physical system. Yet, unlike an uncertainty analysis, having knowledge of the probability distributions is not a prerequisite for data-driven machine learning models. More often, data-driven models reveal incomplete specifications of physical models, which can identify regimes where observed behavior deviates from current understanding [42]. Chapter 3 will cover more detail into the specific types of machine learning models that are utilized in this research.

As previously mentioned, brittle IR materials have many applications in the commercial and defense industries. The research in this dissertation was used in a practical demonstration - the production of fast-axis (FACs) and slow-axis collimators (SACs) for a high-power diode laser systems [43]. The base form of these lenses is a cylinder. FACs are an essential element in high-power diode laser systems as they have a high-numerical aperture and short focal length (around 200 μm) for focusing the beam. The lenses are also fixed to the heat sink to help dissipate heat generated

during operation [44]. The function of a SACs is to use an array of lenslets that correct error from the FACs with slow-axis collimation of the beam. As a final product of this research, a pair of collimating lenses were produced for a defense application.

The original contributions of this research are: (a) a comprehensive analysis of the cutting mechanics of single-crystal germanium, specifically studying the effects of major crystal orientation in germanium and cutting speed; (b) a methodology for producing flat, damage-free test samples in single-crystal germanium; (c) a quantitative comparison of the damage induced by diamond turning, MRF and CMP, and (d) a machine learning model for estimating surface finish parameters Sa, Sq, and Sz for SPDT of single-crystal germanium and oxygen-free high-conductivity copper.

CHAPTER 2: EXPERIMENTAL SETUP AND EQUIPMENT

2.1   Introduction

2.2   Machine, Tools, Cutting Configurations, Parameters

A Moore Nanotechnology 350FG machine tool was used to machine Ge and copper (Cu). Two machining configurations were used in this research: single-point diamond turning (SPDT) and flycutting.

2.2.1   Single-Point Diamond Turning

SPDT for this research is a face turning operation. Figure 2.1 shows how the machine input parameters dictate the position and motion of the the diamond tool as the workpiece is cut. In a perfect scenario, the SPDT operation imparts a cusp pattern, as seen in Figure 2.1, which is a geometric replication of the the tool nose radius (R) and feed per revolution (f_r). This simple geometric surface model is useful to assist machine operators in estimating the final surface roughness after SPDT. This surface roughness estimate and others are discussed later in the Experimental Results section.
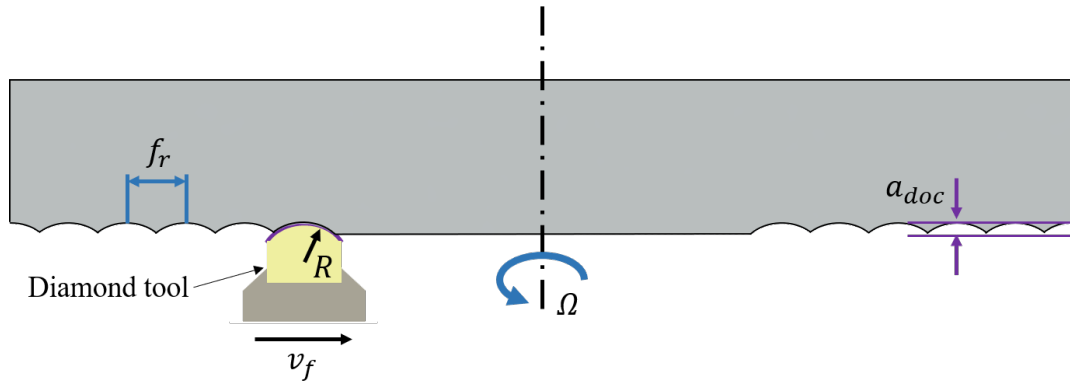
Figure 2.1: Surface generation from SPDT facing operation.

2.2.1.1   Machining Parameters for Machine Learning

The information reported in this section was used from [42] and copyright permission was provided by the publisher. See Appendix A for the supporting documents.

Ge and Cu were SPDT with a variety of input parameters to produce a two datasets for predictive models using machine learning methods. Table 2.1 summarizes the tools and selected input parameters for the datasets. The diamond tool used in the Cu experiments included tool no.1. The Ge experiments were conducted with tools no.2, no.3, and no.4.

Table 2.1: SPDT parameters used to produce dataset for predictive machine learning models.

Tool	R (mm)	α (deg)	f_r (μm/rev)	a_{doc} (μm)	V_c (m/sec)
no.1	0.25	0	0.1 - 40	1, 10	0.3, 3.0
no.2	0.5	-15, -25, -45	0.1 - 5.0	5, 25	0.5, 2.0, 6.0
no.3	1.0	-15, -25, -45	0.1 - 6.5	5, 25	0.5, 2.0, 6.0
no.4	5.0	-15, -25, -45	0.3 - 10	5, 25	0.5, 2.0, 6.0

Other parameters, such as Ω and v_f, are calculated based on the parameters provided in Table 2.1. Eq 2.1 and Eq 2.2 are used to calculate these parameters.

$$\Omega = \frac{2V_c}{\pi r} \qquad (2.1)$$

$$v_f = \Omega f_r \qquad (2.2)$$

2.2.1.2   Sample Surface Preparation for Uncertainty Analysis

The Ge sample under test was SPDT on an ultra-precision machine tool. The tool used was a single-crystal diamond with a 5.0 mm, controlled waviness nose radius and a -25 degree rake angle. The nominal depth of cut for generating surfaces was

25 μm, and the commanded feeds were 1, 10, 25 μm/rev. The resulting surfaces were measured using a CSI to collect surface roughness information. Table 2.2 below shows a summary of the commanded input parameters for the machining operation, as well as, the analytically estimated surface roughness.

Table 2.2: Commanded machine parameters and predicted surface roughness.

R (mm)	f_r (μm/rev)	a_{doc} (μm)	Ω (rpm)	Sa_{pred} (nm)
5	1	25	2000	0.006
5	10	25	2000	0.642
5	25	25	2000	2.566

A SiC-CVD optical reference flat standard (serial no. 990784043) for the Zygo NexView was used as a baseline surface. The naming convention for this surface is SiC-CVD. It served to assist in quantifying how surface texture influences the uncertainty of the measurement. The optical reference flat has a near perfect surface. Figure 2.2 shows the height map for the SiC-CVD surface. The mean Sa and Sq of 50 measurements is 0.1 nm and 0.2 nm, respectively. Surface processing included a plane removal and an 80 μm FFT filter.
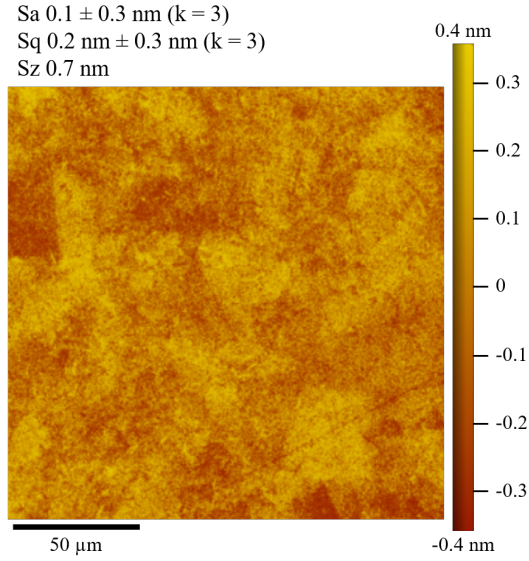
Figure 2.2: SiC-CVD height map.

The CSI with a 50x objective (1x zoom) was used to collect surface data from each of the surfaces. The samples were setup up such that less than 5 nm of tilt remained in the setup misalignment. Thus the uncertainty associated with tilt misalignment was considered negligible. The measurement mode was set to: (1) CSI; (2) high z-resolution; (3) 1 average. The surfaces were post-processed by removing a plane. A total of 50 measurements were collected per site of interest.
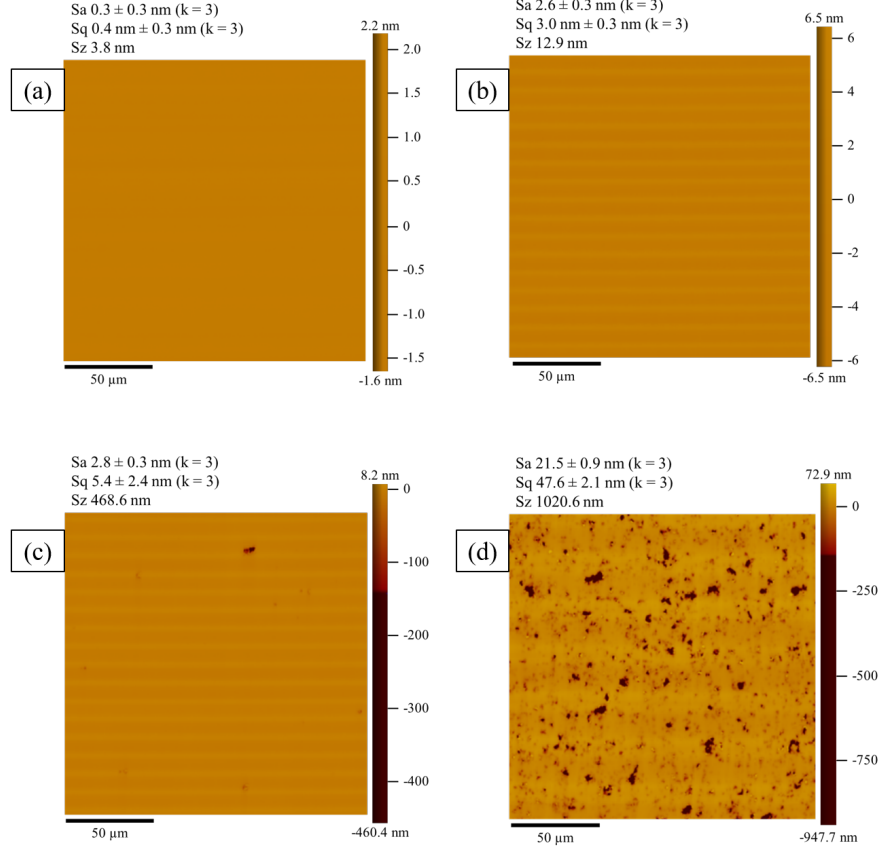
Figure 2.3: Height maps for (a) Ge-1; (b) Ge-2.1; (c) Ge-2.2; (d) Ge-3.

Ge-1, Ge-2.1, Ge-2.2, and Ge-3 indicate the nomenclature for the 1 μm/rev, 10 μm/rev, 10 μm/rev, and 25 μm/rev surfaces, respectively. The surfaces in Ge were measured along the assumed crystal orientation <011>, which is a known cleavage direction that exhibits more surface fracture than other orientations [23]. The surface Ge-2.1 was approximately clocked 22.5 degrees with respect to <011>. Figure 2.3 shows a height map for each of the surfaces. Table 2.3 provides the mean Sa and Sq values for each surface.

Table 2.3: Mean Sa and Sq measured values of 50 measurements per surface.

	SiC-CVD	Ge-1	Ge-2.1	Ge-2.2	Ge-3
Mean Sa (nm)	0.1	0.3	2.7	2.9	21.6
Mean Sq (nm)	0.2	0.4	3.1	5.0	47.6

2.2.1.3   Sample Preparation for Magneto-Rheological Finishing

The two samples for this study are Ge with a major crystal orientation of (100) that were grown with a known miscut in the crystal orientation of $\pm$ 1 degree. The two Ge pucks were prepared by SPDT and post-processed with either MRF polishing or the MRF spotting technique. The MRF spotted sample was later etched to reveal more information within the surface of the Ge pucks. The MRF setup and results are discussed in Chapter 2 and 4, respectively.

Single point diamond turning on an ultra-precision machine tool was utilized for the project to manufacture the parts under test. The machine tool used was a Moore Nanotechnology 350FG located in an environmentally controlled lab which is kept at a traceable 20 degrees Celsius. A single-crystal diamond tool with a R of 3.0 mm and an α of -25 degrees was used. Figure 2.1 illustrates the function of a turning operation using a single point diamond tool.

The machining parameters for this study included are summarized in Table 2.4. The part was centered on the main spindle of the machine tool and the tool positioning was setup from the samples surface. The initial turning parameters for creating a relatively damage free surface and subsurface were as follows: a_{doc} of 0.5 μm, f_r of 0.5 μm/rev. Table 2.4 describes the turning parameters used to create a highly damaged surface. These parameters were determined from a sub-study where a Ge puck was SPDT with an array of different f_r values. The effect of constant surface speed is neglected.

Table 2.4: Diamond turning parameters.

R (mm)	f_r (μm/rev)	a_{doc} (μm)	Ω (rpm)	v_f (mm/min)
3.0	35	10	1000	35

The two samples are identified as follows: (1) sample 1 - MRF spotting technique; (2) sample 2 - MRF full aperture polish. Sample 1 was used to estimate the subsurface

damage present in the sample after SPDT. Sample 2 was used to evaluate the MRF machines ability for removing damage and mitigating mid-spatial frequencies from the SPDT workpiece.

2.2.1.4   Sample Preparation for Surface Integrity Study

This section discusses the sample preparation for surface integrity study. A puck of Ge with a major crystal orientation of (100) was diamond milled to produce mini-pucks with an alignment flat that identified a preferred cutting orientation where surface fracture is minimized. Identification of the preferred orientation was based on [23]. These 8 mm diameter mini-pucks, as shown in Figure 2.4, were then turned off-axis with a single-point diamond tool that had a R of 3.0 mm and a α of -25 degrees. The off-axis turning operations were completed such that the cutting direction was approximately parallel to the flat. The nominal depth of cut was 10 μm for all turning processes. As-cut surfaces that were produced using f_r values of 0.3, 1, 5, 9, and 20 μm/rev were investigated.
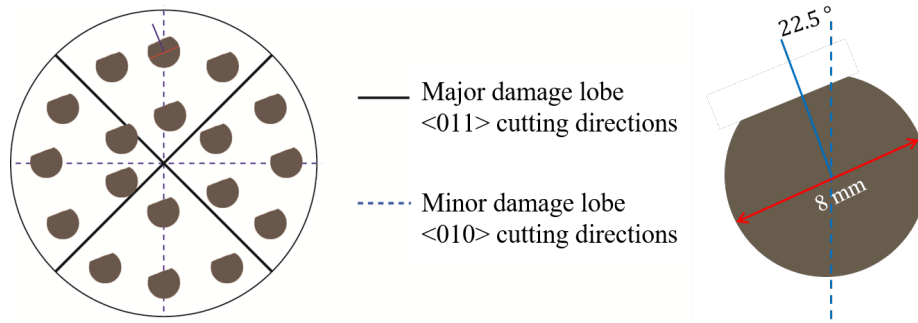
Figure 2.4: Layout of the surface of Ge with mini-pucks.

Three additional surfaces were generated with a f_r of 9 μm/rev and were subsequently finished with a chemo-mechanical polishing (CMP) or magneto-rheological finishing (MRF) polishing process. Specifically, these processes included MRF, CMP, and CMP followed by chemical etching. The MRF process used a D10 slurry with an average diamond particle size of ~150 nm and a material removal rate of about 8

μm/min. The CMP process consisted of a diluted-bleach and Ultra-Sol S39 (110 nm diameter colloidal silica) slurry using a urethane polishing pad. The material removal rate of the CMP process was about 6.3 μm/hr. Approximately 18 μm was removed from the surface during both the CMP and MRF processes. Etching was performed with 3% hydrogen peroxide for 2.5 min at room temperature. Based on reported etching rates in the literature, this would indicate a minimum of $\sim$50 nm of material removal.

2.2.2   Flycutting

A high speed air-bearing spindle was used with a flycutter arbor. The spindle's air supply enters the machine at approximately 24 °C. Thus, the spindle is cooled via chillers to 20 ±0.1 °C. The spindle is mounted on a granite boss for thermal and vibration isolation. Figure 2.5 shows the high speed spindle with the axis configuration of the Moore Nanotechnology 350FG.

High speed air-bearing spindle

Flycutter arbor

Ω

Y

Z

X
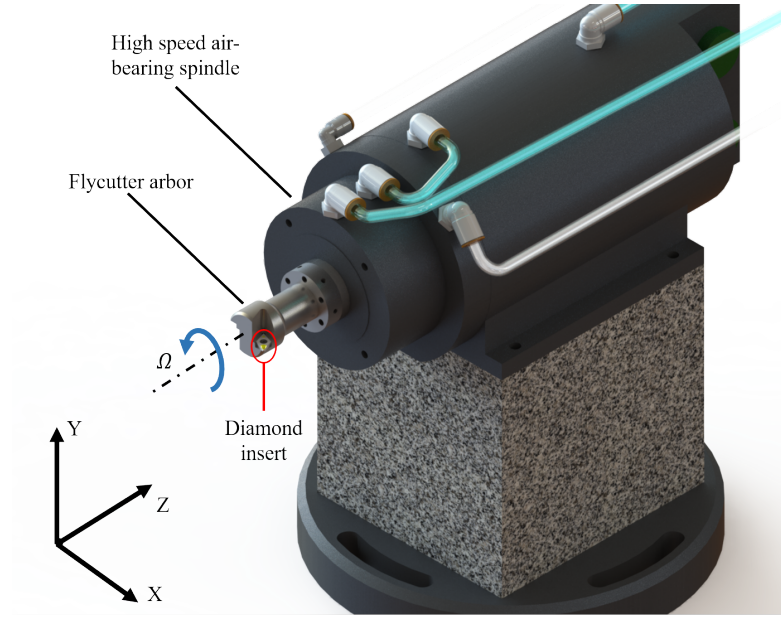
Diamond insert

Figure 2.5: High speed air-bearing spindle with flycutting arbor.

Uni-directional raster flycutting was used in this research with a single tooth interaction. Figure 2.6 shows the flycutting configuration using a single-crystal diamond insert. The stepover (S_o) drives the surface finish with ductile-dominated cuts are achieved. The f_r has a small significance for introducing brittle dominated cuts due to the sweeping direction of the flycutter.
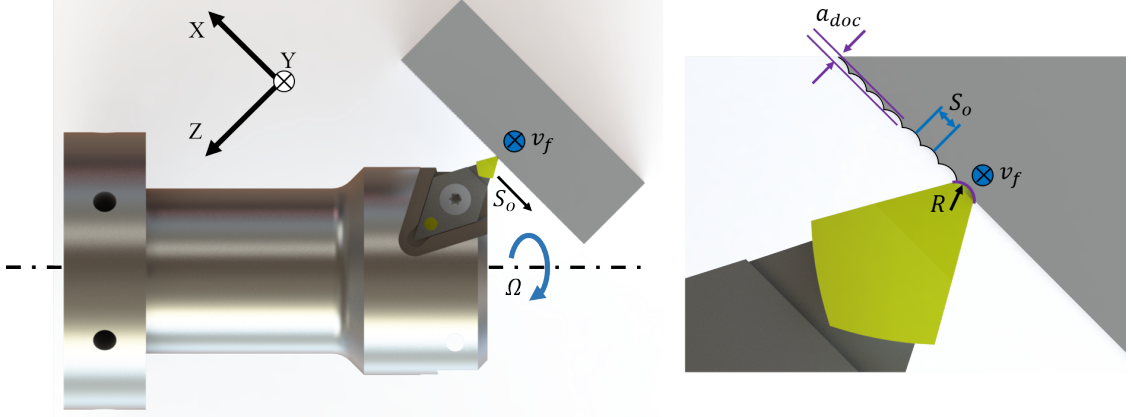
Figure 2.6: Surface generation from raster flycutting operation.

2.2.2.1   Flycut Tool Arrangement and Parameters for Application

This section describes the part preparation and flycutting configuration for the application of machining of two IR optics (fast- and slow-axis lenses). The results for the application are discussed in Chapter 6. The manufacturing procedures for producing each lens is as follows: (1) an initial turning operation, (2) a flycutting operation with a raster path along the cylinder axis, (3) a rough dicing operation, and (4) an edge finishing to final dimensions. Non-contact and contact metrology methods were used to verifying surface quality and prescriptions. The setup and methodologies used in metrology will be discussed in a later section. All manufacturing and metrology were completed in temperature controlled labs (20 ±0.1 C).

Targets for surface roughness and form error (departure from prescription) were 10 nm Sa and ±300 nm, respectively. Waviness or so-called mid-spatial frequency errors have not yet been specified. However, based on experience, we expect these errors to be on the order of ±150 nm with a spatial wavelength that is dependent on the cutting parameters. The sources of these errors are thermal and are result from cycles in the machine temperature control systems which have a temporal period of less than 10 minutes.

The Ge workpieces used in the application had a major crystal orientation of (100). They were first diamond turned to identify the preferred cutting direction for the flycutting operation. The preferred cutting direction allows for a higher material removal rate while maintaining a ductile-dominated cut. The final prepared surfaces were diamond turned using a 5 μm depth of cut and a 0.5 μm/rev feed to preserve a high-quality surface integrity. Figure 2.7 shows the diamond turning operation. Spray mist with odorless mineral spirits used to evacuate chip and lubricate the cutting operation.
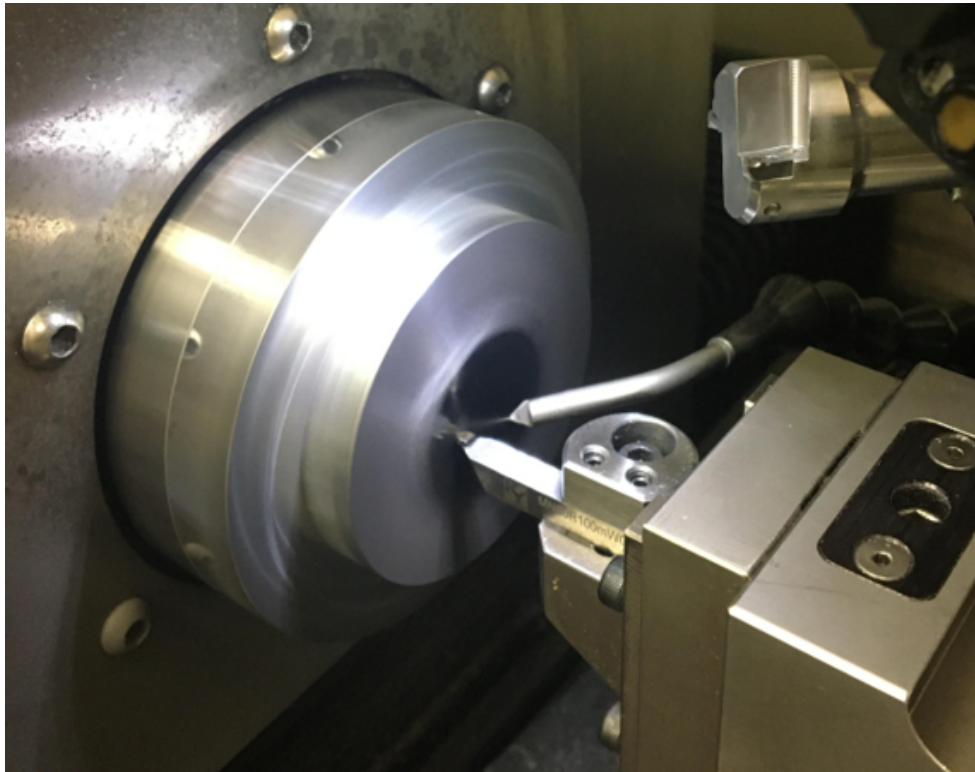
Figure 2.7: Single-point diamond turning Ge.
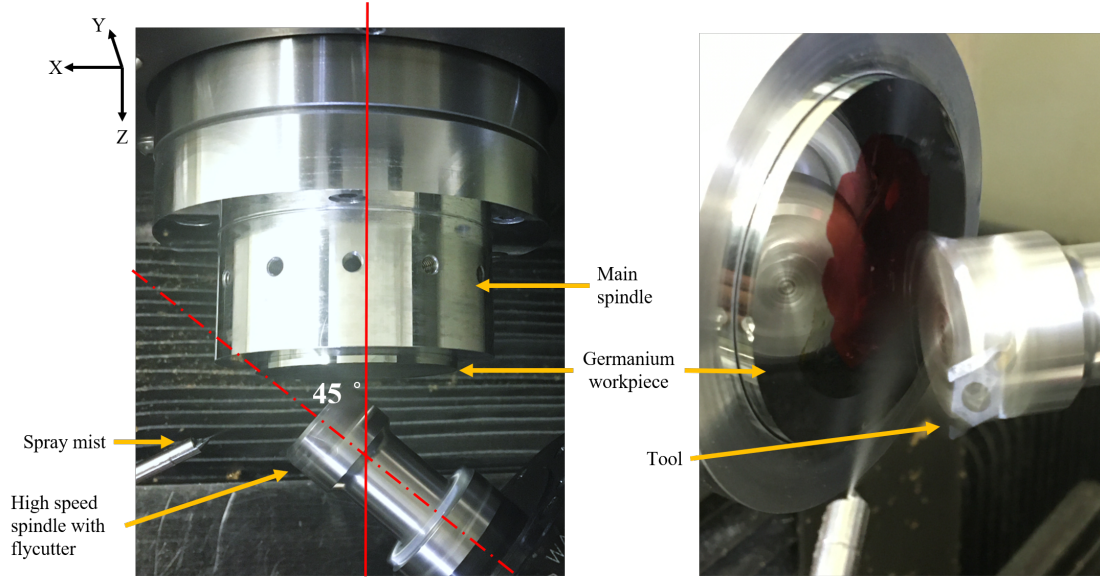
Figure 2.8: Single-point diamond turning Ge.

The flycutter apparatus was setup using the high speed spindle mounted on the z-carriage and clocked at a 45 degree angle relative to the z-axis of the machine. Figure 2.8 shows the setup of the flycutter. The Ge workpiece was held by vacuum on the main spindle. C-axis mode was enabled to hold the workpiece in a specific orientation during the flycutting operations. The flycutting operation can be observed in Figure 2.8, where the spindle was set to 30,000 rpm. Both the fast- and slow-axis lenses were cut oversize in the lateral dimensions (XY) to ensure no residual damage was left from the dicing operation.

The fast-axis surface was machined using a single-crystal diamond insert with a nominal R of 250 μm and a α of -25 degree. The insert was mounted to a 25 mm diameter arbor on a 60,000 rpm milling spindle in a flycutting configuration, as previously described in 2.8. The spindle was balanced better than 6 nm following error. Errors in the actual position of the diamond tip and true nose radius led to a correction of the tool nose radius to 229 μm. The nose radius correction was completed by machining a cylindrical artifact in Ge and verifying the radius of the artifact with a tactile profilometer. Table 2.5 shows the machine input parameters.

Table 2.5: Machine input parameters for cutting fast-axis surface.

Machine parameter	rough	medium	finish
a_{doc} (μm)	25	10	5
v_f (mm/min)	500	500	300
S_o (μm)	15	15	5

The slow-axis surface was machined using the same flycutting configuration as previously mentioned and following the same balancing requirement. The diamond insert had a nominal R of 10 μm and a α of -25 degree. The corrected tool nose radius was 10.02 μm. Table 2.6 shows the machine input parameters for cutting the slow-axis surface.

Table 2.6: Machine input parameters for cutting slow-axis surface.

Machine parameter	medium	finish
a_{doc} (μm)	5	5
v_f (mm/min)	500	300
S_o (μm)	5	2

The lenses were diced oversized from a larger Ge workpiece using a milling operation. A milling tool with a 2.536 mm cutting diameter and a zero rake angle was used. The zero rake angle left residual damage on the edges of the part. The damage from the milling operation was subsequently removed during last stage that brought the optics to their final lateral dimensions. Figure 2.9 (left) shows the mounting configuration of the lenses for the lateral trimming operation. Figure 2.9 (right) shows the flycutting arrangement rotated such that axis of rotation is perpendicular to the parts surface.
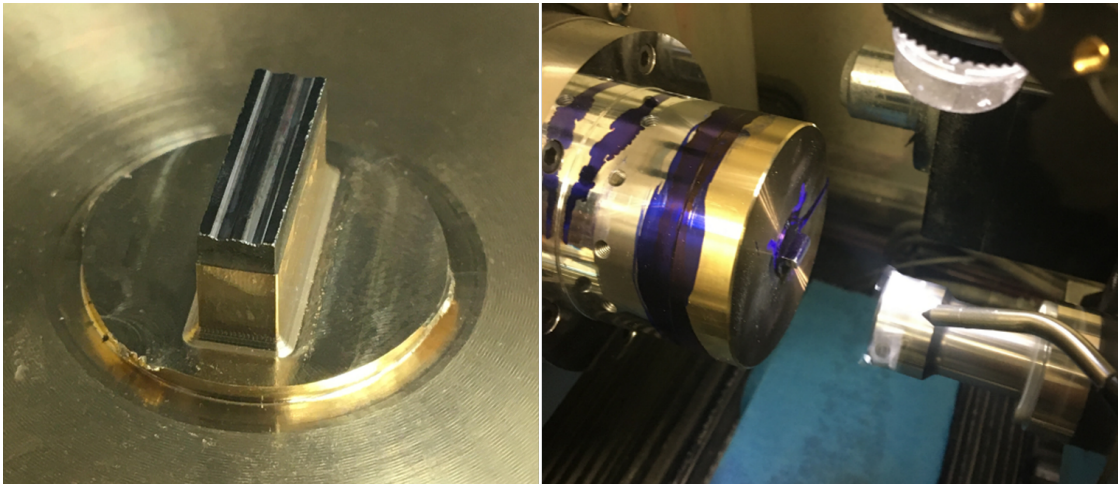
Figure 2.9: (left) Extended boss for lateral trimming; (right) flycutting arrangement.

2.3   Polishing

Two polishing methods were used in this research: (1) chemo-mechanical polishing (CMP) and (2) magneto-rheological finishing (MRF). The following sub-sections will the discuss the equipment and process for each method.

2.3.1   Chemo-Mechanical Polishing

A CMP process was developed to produce flat, damage-free samples for diamond machining experiments. The results from this study are reported in Chapter 4, section 4. The CMP equipment can be seen in Figure 2.10. The polishing fluid was a mixture containing a 1:1:10 dilution in the following ratio: (a) 200 g of Ultra-Sol S39, a colloidal silica solution, (b) 200 g of bleach, and (c) 2000 g of deionized water. The polishing pad used was a polyurethane impregnated polyester felt pad (Suba$^{\text{TM}}$ 600) with the following specifications: (a) compressibility of 4%, (b) Shore D hardness of 80, and (c) thickness of 1.27 mm. The mass holding the Ge down was 150 g. The rotation speed was set at 55 rpm.
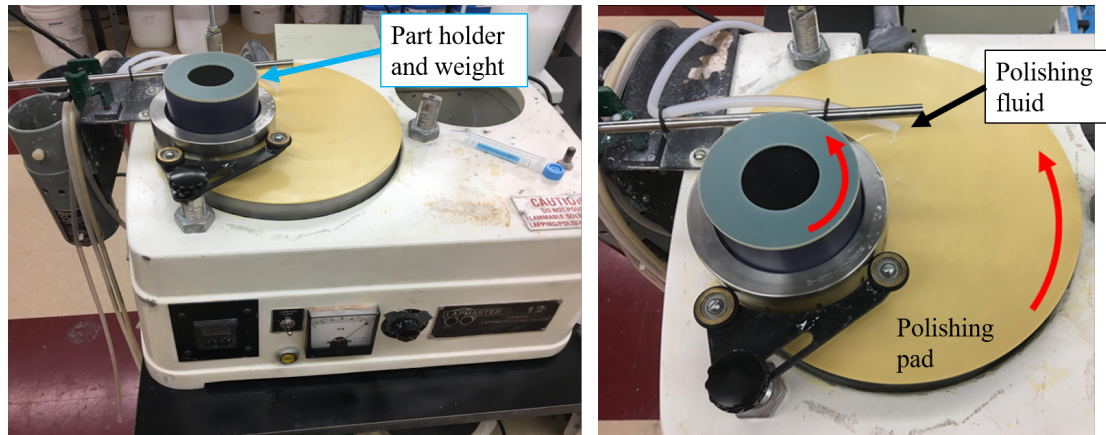
Figure 2.10: CMP equipment for polishing germanium.

2.3.2 Magneto-Rheological Finishing

The magneto-rheological finishing (MRF) spotting technique and full aperture polish were performed on the QED Q22-XE machine. The MRF fluid D10 was used for this study. D10 fluid is composed of a non-magnetic abrasive (diamond), a magnetic carbonyl iron, and a stabilizer (sodium hydroxide). The MRF fluid loses moisture as the fluid is circulated. Deionized (DI) water was used to control the viscosity of the fluid. The non-magnetic abrasive in D10 fluid is 150 nm sized diamond. The magnetic carbonyl iron allows for the fluid to be ejected from the pump system via a nozzle onto a rotating wheel. A permanent magnet at the wheel assembly creates a magnetic field around the rotating wheel, such that, the carbonyl iron aligns and forms a stiff ribbon. The abrasive is pushed to the outer surface of the ribbon. The workpiece can then be mounted to a multi-axis arm and polished by the MRF ribbon. The MRF machine function is as depicted in Figure 2.11.
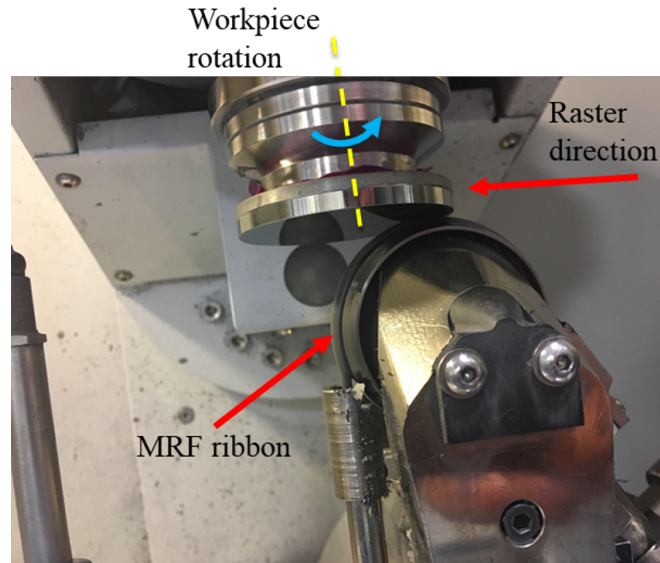
Figure 2.11: MRF equipment for polishing germanium.

In order to setup the MRF machine for polishing, the material removal rate for Ge needed to be characterized using the D10 fluid. Four spots located 90 degrees from each other were statically polished (i.e. a single location on the workpiece). The

polishing time was 5 seconds. A Fizeau Verifire was used to measure the surface. Figure 2.12 shows the resulting spots for characterizing the material removal rate. The material removal rate of Ge using D10 fluid with a viscosity of 76 cP was 8 μm/min. The ribbon height was 1.8 mm, the depth of penetration into the ribbon by the workpiece was 0.7 mm.
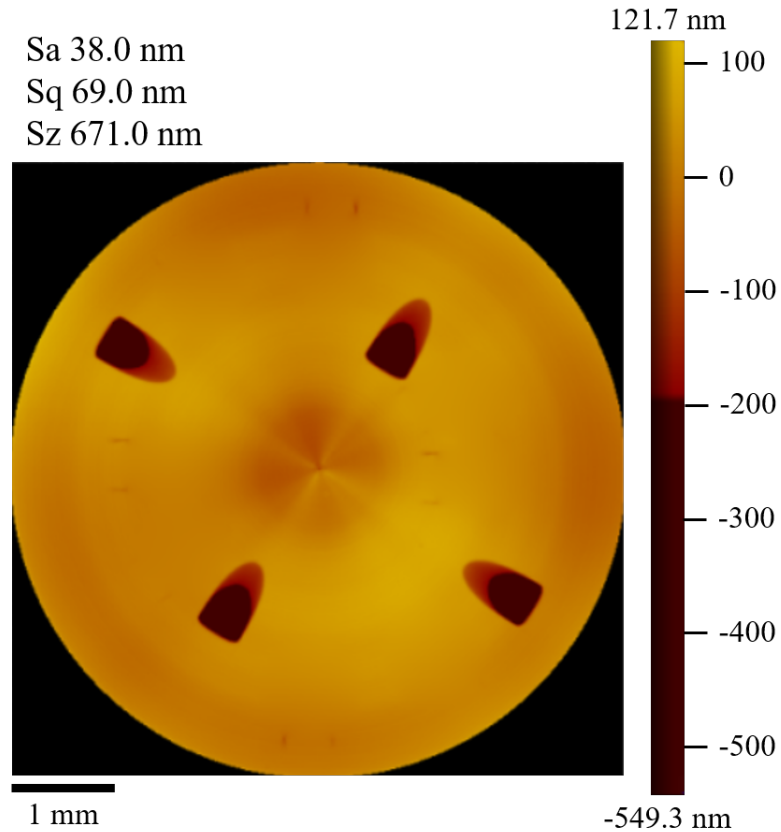
Figure 2.12: MRF - spot characterization.

Table 2.7: MRF spot information.

Spot no.	Time (sec)	Angle (deg)	Viscosity (cP)
1	3	0	85.0
2	6	20	85.4
3	9	40	85.9
4	12	60	86.0
5	15	80	86.9
6	18	100	86.9
7	21	120	87.3
8	24	140	86.8
9	27	160	86.9
10	30	180	86.7
11	33	200	86.8
12	42	220	82.3
13	51	240	86.2
14	60	260	87.2
15	69	280	85.9
16	78	300	86.4
17	87	320	81.5
18	96	340	85.1

The MRF spotting technique was completed on sample 1. There were 18 spots polished into the surface at defined time intervals and specific locations on the workpiece. This information is summarized in Table 2.7.

Table 2.8: MRF full aperture polish.

Iteration	Removal step (μm)	Total amount removed (μm)
1	0.5	0.5
2	0.5	1.0
3	0.5	1.5
4	0.5	2.0
5	0.5	2.5
6	0.5	3.0
7	1.0	4.0
8	1.0	5.0

The MRF full aperture polish was completed on sample 2. In order to observe the removal of damage and mitigation of mid-spatial frequencies from the SPDT process, the workpiece was polished in steps. The polishing steps removed 500 nm of material at each iteration until 3.0 μm were removed in total. The next step size was 1 μm of material removed until 5 μm were removed in total. Table 2.8 shows the breakdown of these iterations.

2.4   Materials, Crystal Orientations

Single-crystal Ge and oxygen-free high-conductivity copper were used in this research. The following sections provide background information for the two materials.

2.4.1   Single-crystal Germanium

Ge is most extensively used as an IR optical material in thermal imagining, spectrometers, and quantum cascade laser applications. Ge is (ideally) optically isotropic with an excellent range in IR transmission (3-12 μm), high index of refraction (n = 4.003), and its high hardness in terms of Knoop hardness (HK = 780) [38]. Due to it's high index of refraction, Ge transmits approximately 45% of the IR light that passes through it. Imperfections in the crystal lattice during growth or subsequent manufacturing stage will ultimately determined the effectiveness in optical performance and optical isotropy. High-purity Ge (99.999% pure) is preferred for optical applications, and it is important that residual stresses are minimized to reduces the effects of birefringence. Birefringence can lead to anisotropic optical qualities within surface that impart differences in the polarity and refractive index. This minimizes the impedance on optical performance from the bulk material. Subtractive manufacturing methods, such as SPDT, will impart damage and disorder into the surface. Understanding how to minimize the effects in the kinetic and dynamics of the machining operation will only enhance the efficiency. Table 2.9 provides a summary of the mechanical properties for Ge. Ge has a thermal conductivity of 0.58 W/(cmC) and a melting temperature at approximately 938.2 C.

Table 2.9: Mechanical properties of single-crystal germanium.

Young's modulus	Shear modulus	Bulk modulus	Poisson ratio
103 GPa	41 GPa	75 GPa	0.26

2.4.2   Oxygen-free High-conductivity Copper

Oxygen-free high-conductivity (OFHC) copper is a diamond turnable material [45]. It exhibits minimal grain relief from the turning operation, i.e. the material is ideal for producing optical-grade surface finish, with minimal digs from grain pull-out. OFHC copper is commonly utilized in high-intensity laser applications [46]. The research conducted for this dissertation used OFHC copper in the machine learning study, discussed in Chapters 3 and 5, because of its well-behaved material response when diamond turned.

2.5   Surface Measurements and Metrology Equipment

Surface finish of machined and polished parts were measured using a Zygo NexView coherence scanning interferometer (CSI). Surface measurements that report surface finish are processed by removing a plane and applying an Fast-Fourier-Transform (FFT) band-pass filter (2.5 to 80 μm unless otherwise specified). Uncertainty measurements were completed on the CSI to examine the effects of cusp patterns from diamond machining and anisotropic surface fracture. The results from the uncertainty analysis are reported in Chapter 4 under the section heading Surface Measurement Uncertainty.

2.5.1   Measurement Procedure for MRF Study

This section discusses the measurement procedure for the MRF spotting technique and full aperture polish study. Prior to measuring on the CSI, the samples were thoroughly cleaned using a mixture of DI water and Dawn dish soap to remove any MRF fluid remaining on the surfaces after polishing and spotting. The samples were then carefully drag wiped with acetone and ethanol, respectively.

The CSI was used to measure samples 1 and 2 for characterization and analysis of the surface topography. Sample 1 and sample 2 were measured using the 20x objective on the NexView. The field of view for this objective is 418x418 μm, with a numerical aperture of 0.40. The 2.75x objective was also used to measure sample 2 for a PSD analysis of the surfaces. The field of view of this objective 3.0x3.0 mm, with a numerical aperture of 0.08. Samples 1 and 2 were marked with fiducials to ensure repeatability of the measurement locations.
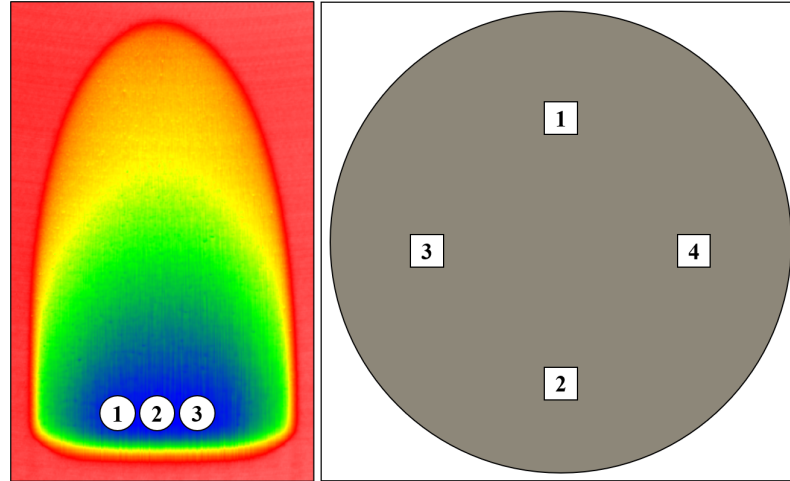
Figure 2.13: MRF - measurement locations (left) MRF spot and (right) MRF full aperture polish.

Sample 1 - MRF spotting technique - was measured at the deepest area in the spots in three locations, as shown in Figure 2.13(left). Every height map produced was an average of three measurements, and all three locations were averaged to provide surface roughness parameters for further analysis of each spot. In addition, three measurements were taken on the original diamond turned surface for comparison.

Sample 2 - MRF full aperture polish - was measured at four locations as depicted in Figure 2.13(right). Again, each height map produced was an average of three measurements. The four locations were evaluated independently, and the surface roughness parameters produced were averaged.

All height maps evaluated for surface roughness parameters had the following post-processing steps: (1) removed piston and tilt; (2) filter areal data with a FFT high-pass filter with a period of 80 μm; (3) the surface roughness parameters Sa, Sq, and Sz were reported. All height maps used for PSD analysis had a piston and tilt term removed.

2.5.2   Metrology Procedures for Verifying Application Parts

A NexView CSI was used to verify the surface quality for both lenses and the radius of the slow-axis cylinders. Surface roughness results, such as Sa and Sq, were

processed by removing a cylinder and applying an FFT band-pass filter in accordance with ISO 10110-8:2010. All measurements were taken in a temperature controlled lab (20 ±0.1 C).

A Mahr Marsurf LD 260 with a diamond tip probe was used to verify test artifacts and the prescription of the fast-axis lens. The diamond tip probe has a nominal radius of 2 μm. Figure 2.14 below depicts the process for scanning the surfaces. The scan direction was made perpendicular to the acylinder axis. Data processing included trimming and leveling of trace data. The trace of the acylinder from the fast-axis surface was compared to the optical prescription. All measurements were taken in a temperature controlled lab (20 ±0.1 C).
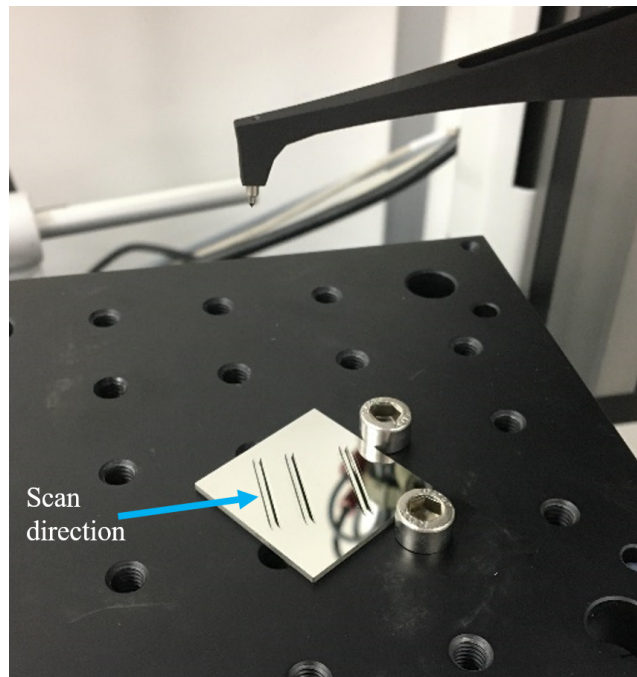
Figure 2.14: Mahr profilometer measurement.

2.6   Surface Integrity Measurements

The subsurface damage from polishing and machining of Ge were completed at Oklahoma State University and Los Alamos National Laboratory. The instruments used to examine the subsurface of the parts under test are a confocal Raman micro-

scope and a Rutherford back-scattering spectrometer. Both of these instruments are non-destructive in nature; however, if the laser intensity is not well tuned in confocal Raman, the surface and subsurface can be heated to recrystallize the local area. Thus, the recrystallization will erase the history of machining or polishing.

A confocal Raman microscope in the back-scattering configuration was used a 532 nm wavelength laser with a spot size of approximately 1 μm that had a probing depth of 10-30 nm. Confocal Raman is traditionally used for material, chemical and life sciences. This research uses confocal Raman microscopy to measure damage from ultra-precision machining and polishing applications. Here low-frequency vibrational modes in the material lattice of the part under test are examined to reveal subsurface integrity information. Incident photons from the laser will strike the crystal lattice and back-scatter to a detector. The back-scattered photons provide insight on residual stress within the lattice which is indicated by a shifts in the peak. Broadening of the peak can indicate lattice disorder, such as cracks or dislocations like twinning.

Rutherford backscattering spectroscopy was used to examine the surface integrity of polished and SPDT Ge. The subsurface damage of the surfaces was investigated with channeling RBS, performed at Los Alamos National Laboratory. The channeling RBS beam was collimated with 2 MeV ^{4}He$^+$ ions, a spot size of approximately 1 mm^2, and kept in a vacuum chamber at 4-5x10^{-7} Torr. The backscattered particles were collected by a solid state detector. Surface response was quantified by the spectra of backscattered particles versus backscattered energy. Usefulness of the data collected is typically limited to the first micrometer ($\sim$1 μm) of the surface under test.

2.7 Cutting Measurements and Dynamometer Equipment

The cutting forces of the machining operations were measured using multi component transducer-based dynamometers. Micro-cutting force measurements require high fidelity and resolution data capture. Prior to all force measurements, the dynamometers were reset to zero to ensure good repeatability from the piezoelectric measurement technology. This minimized the errors from thermal drift.

A Kistler mini-dynamometer (mini-dyn) - model 9256C1 - was used to measure forces during SPDT operations. The mini-dyn and charge amplifier can be seen in Figure 2.15. The natural frequency of the mini-dyn is approximately 5 kHz prior to adding the mass from a part under test. The mini-dyn provided cutting (tangential) and thrust (normal) force information. Resultant force F and angular Θ information were calculated from the collected data.

Figure 2.15: (left) Kistler mini-dynamometer - model 9256C1 and (right) Kistler charge amplifier.

A Kistler micro-dynamometer (micro-dyn) - model 9109AA - was used to measure forces during flycutting operations. The micro-dyn and charge amplifier can be seen in Figure 2.16 The micro-dyn provided a higher natural frequency (15 kHz) to combat with the high tooth passing frequency of a flycutting operation. Thus improving the accuracy of the data collected. The micro-dyn has the capability of measuring forces from spindle speeds up to 120,000 rpm.

Figure 2.16: (left) Kistler micro-dynamometer - model 9109AA and (right) Kistler charge amplifier.

2.7.1 Data Acquisition and Analysis

Force data was monitored and collected from the mini- and micro-dyn via a custom virtual instrument (VI) LabVIEW program. The VI-LabVIEW program read the force data through a NI USB-6251 BNC data acquisition (DAQ) board. The force data was save and post-processed in MATLAB®, version 2019/2020.

CHAPTER 3: UNCERTAINTY ANALYSIS, BASIC MECHANICS, AND

MACHINE LEARNING

3.1 Surface Measurement Uncertainty Analysis

Measurement uncertainties are important to identify and quantify such that a more reasonable and reliable characterization is provided with the measurand. Furthermore, an estimate of the uncertainty in the measurement for the measurand will provide higher confidence in reporting measured values. In the case of this study, the measurands are output parameters from a CSI measurement. These measurands are Sa and Sq. Note that the result of a measurement is an estimate of the true value of the measurand [47], where the true value can never really be known. A prediction of the analytically estimated value for surface roughness can be calculated by using Eq 3.1.

$$Sa_{pred} = \frac{f_r^2}{9\sqrt{12}R} \tag{3.1}$$

Sa_{pred} is the prediction of the surface roughness for a single-point diamond turned surface, f_r is the feed per revolution in μm, and R is the radius of the tool in μm [42]. However, this prediction of the surface roughness has proven to be an insufficient method of providing reasonable values of the measurand. This is noticeable when f_r is a very low or high value. The actual measurement of the surface roughness can deviate orders of magnitude due to temperature variations during the cutting operation, or due to material characteristics [48]. As previously mentioned, Ge can have a brittle response to machining if parameters are not carefully selected. When Ge is diamond turned with aggressive machining parameters, the result is unfavourable fracture on

the surface, as well as, a fair amount of subsurface damage. Surface fracture observed from diamond turning can also be considered an inhomogeneous surface topography.

In order to provide a proper formulation of uncertainty, the GUM states that the measurand definition and equation must be well defined, such that all input quantities involved in the measurement are captured. The GUM also indicates that each input quantity should be evaluated using a Type A or Type B evaluation. Type A evaluations of the input quantity is completed using statistical methods, and a Type B evaluation uses other methods than statistical ones. Monte Carlo simulations provide the best approach when doing a Type B evaluation [49]. Additionally, Type B evaluations require a good understanding of the input quantities because probability density functions are used. Either method is used to determine the standard measurement uncertainty, which will be used later when determining the combined measurement uncertainty. All uncertainty evaluations should report a coverage factor when reporting the expanded uncertainty of the measurement.

There are many papers and publications focusing on the uncertainties associated with profile measurements [48, 49, 50]. However, there seems to be a lack in literature that includes the effects of surface texture inhomogeneity in areal surface measurements using a CSI. Surface texture inhomogeneities for profile measurements are largely degraded when the user applies the appropriate filtering [50]. Such filtering can include an FFT high pass filter. Homogeneity of the surface has been reported as a major contributing factor in the uncertainty of measurement [51]. CSI measurements of rough surfaces can also be known to lead to artefacts in the measurement from steep topography [52]. These artefacts can be observed as large spikes location in or around a fracture on the surface that can increase the measured values. Because of this, it can be very useful to compare the measurements results of one instrument to another. For instance, the measurement from a CSI can be compared to that of an a AFM (atomic force microscopy).

3.1.1   Uncertainty Model

3.1.1.1   Measurand Definition and Equations

The definition of the measurand is vital for telling a meaningful story about the quantity describing the object being measured. This work defines the measurand as the areal surface roughness values, Sa and Sq. These parameters are described by Eq 3.2 and 3.3, respectively. The target uncertainty for this study was ± 0.5 nm. The coverage factor considered for the expanded uncertainty was k $= 3$ (99.73 %).

$$Sa = \frac{1}{n} \int \int |Z(x,y)| dxdy \pm U(Sa) \tag{3.2}$$

$$Sq = \sqrt{\frac{1}{n} \int \int |Z^2(x,y)| dxdy} \pm U(Sq) \tag{3.3}$$

CSI measurements can be sensitive, but not limited to: (1) environmental conditions; (2) calibration of the instrument; (3) drift motions of the stage; and (4) the quality and optical properties that are inherently apart of the workpiece under test. The influencing contributors in the measurement are summarized by Figure 3.1.
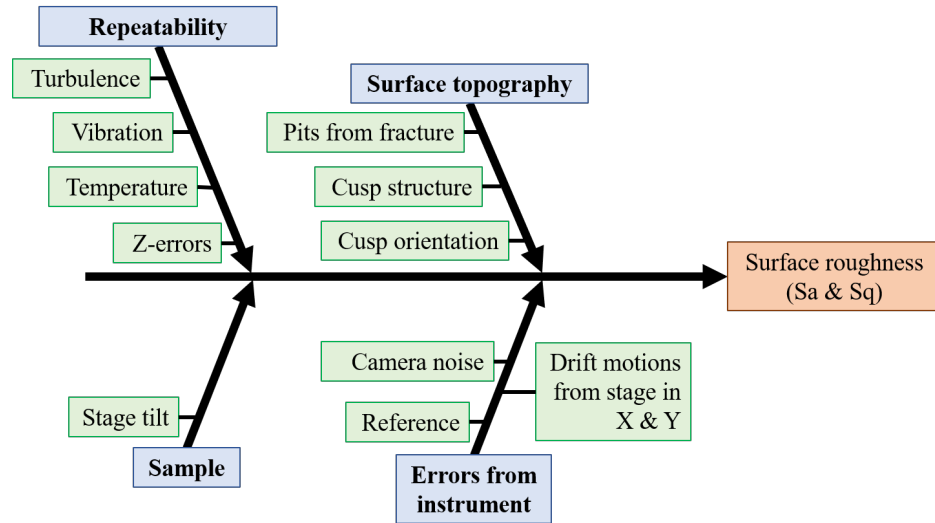
Figure 3.1: Ishikawa diagram - influencing contributors of the measurement.

Sample tilt was assumed to be negligible as the setup minimized the tilt as much as possible. The turbulence was also neglected since the air gap between the workpieces and objective was very small ($\sim$3-4 mm). The instrument setting denoise was turned on for all measurements to minimize camera noise in the measurements. The system's calibrated reference file was subtracted from all measurements in order to minimize artefacts from the instrument. The remaining influencing contributors are assumed to be captured in the performed surface topography repeatability (STR) measurements.

3.1.1.2   Evaluation Methods

Two evaluation methods were considered for analysing the STR of each surface measured. A total of 50 measurements per surface was collected using the CSI. Both methods for analysis used MATLAB® 2018b. All values reported in this analysis are rounded up to 1 decimal place considering the units of nm.

Method 1 provided an analytical model based on the same principles as the STR synthetic reference method used by Venditti et al. [53]. After post-processing of the height maps, the average height map was calculated. This average was then subtracted from the individual height maps, which resulted in 50 individual deviation maps. The *STR Sa* and *STR Sq* were calculated from the deviation maps and averaged. Eq 3.4 and 3.5 were used to calculate *STR Sa* and *STR Sq*. These values represent the estimated uncertainty from modelling Method 1.

$$STRSa = \frac{1}{n} \int \int |Z(x,y)| dxdy \tag{3.4}$$

$$STRSq = \sqrt{\frac{1}{n} \int \int |Z^2(x,y)| dxdy} \tag{3.5}$$

Method 2 was more unconventional from the ISO 27158-604 using a Monte Carlo simulation that evaluated the uncertainty by using the average height map and the 50 deviation maps. A randomly selected deviation map was designated to add a specific

pixel to the same pixel location in the average height map. Each pixel location was randomly chosen from one of the 50 deviation maps. The Sa and Sq values were computed for each iteration using the same formulas, shown in Eq 3.4 and 3.5, produced a probability density function (PDF) for each term. The Monte Carlo simulation ran 10,000 iterations prior to computing the PDF. The corresponding uncertainties were then determined by calculating the standard deviation of the PDF using the built in MATLAB® function 'std'. Figure 3.2 provides an example of a PDF produced from the Monte Carlo code.
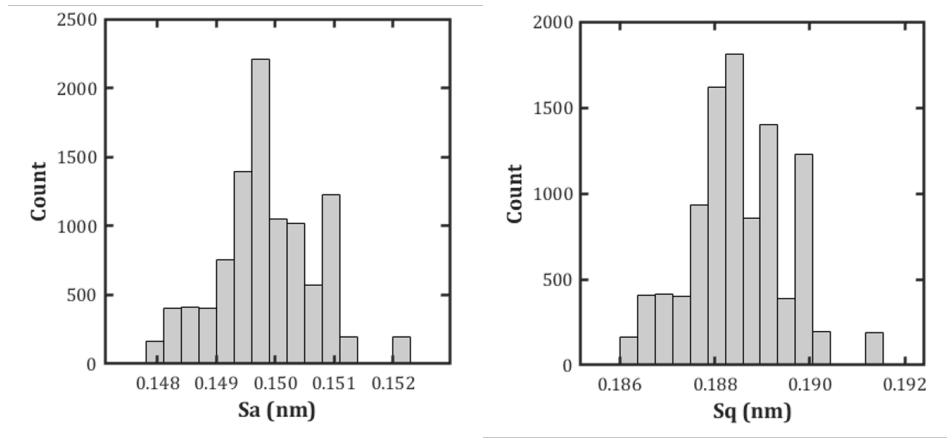
Figure 3.2: SiC-CVD - Monte Carlo resulting PDF after 10,000 iterations.

3.2   Basic Mechanics of Machining

As previously mentioned in the in Chapter 1, Ge is a brittle material and requires a fundamental knowledge in order to effectively machine the material for optical applications. Geometric parameters and machine input parameters all have an important interplay that dictates whether or not the material response is ductile-dominated or brittle-dominated. Simply put, kinematic and dynamic input parameters will decide the cutting mechanics. The R, in combination with a_{doc} and f_r, are the main contributors to defining the chip geometry. Figure 3.3 illustrates the effect of small and large R, where the undeformed chip geometry can be observed. As f_r gets larger the y_c approaches zero and thus the probability of fracture remaining in the generated surface increases.
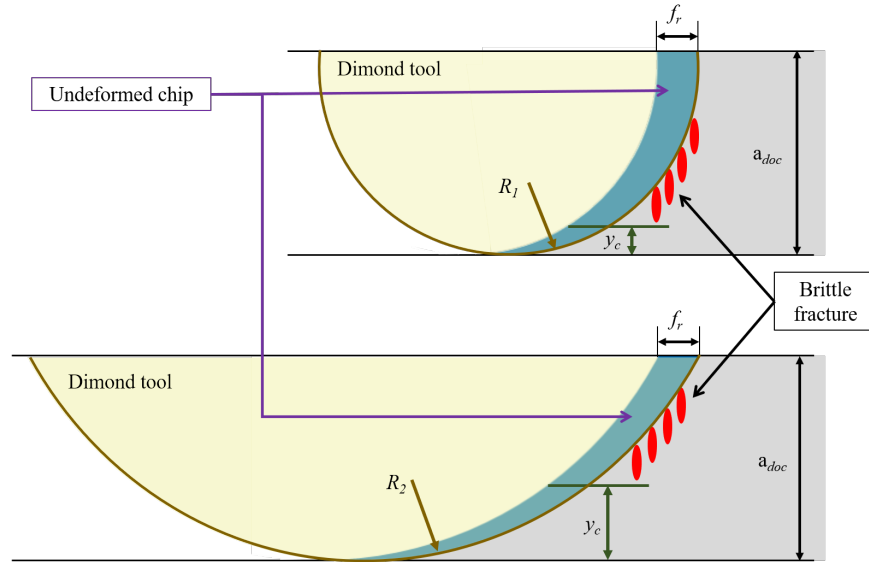
Figure 3.3: Effect of tool nose radius in SPDT of Ge as described by Blake et al. [24].

The undeformed chip thickness has served as a base-line in predicting surface fracture generation. The maximum undeformed chip thickness is described in Eq 3.6.

$$t_c = R - \sqrt{[R - a_{doc}]^2 + \left[R\sin\left(\arccos\left(\frac{R - a_{doc}}{R}\right)\right) - f_r\right]^2} \qquad (3.6)$$

The rake angle of the diamond tool determines the magnitude of tensile and compressive stress resolved into the workpiece during the cutting operation. Figure 3.4 depicts how a negatively raked diamond tool imposes a larger hydrostatic pressure into the workpiece material and suppresses brittle fracture. The suppression of brittle fracture can be examined by an increase in compressive stress and a decrease in the tensile stress. Brittle materials naturally perform better under compressive loading scenarios. Additionally, existing cracks propagation and crack nucleation is ceased or significantly sustained from growth due to the hydrostatic pressure.
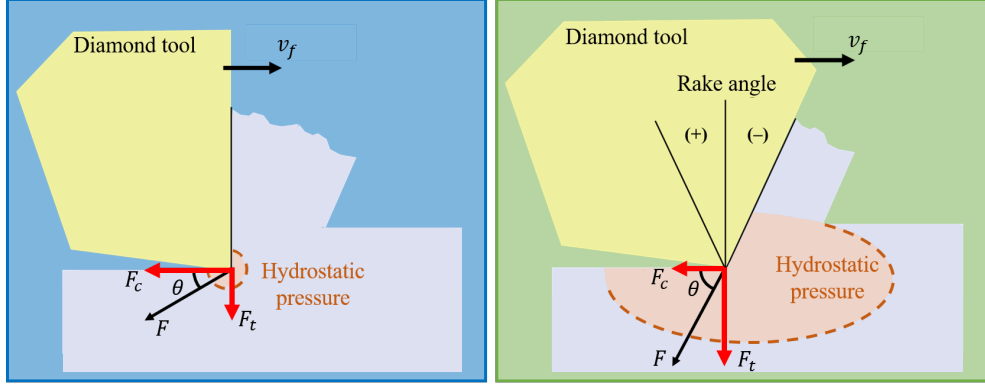
Figure 3.4: (left) zero raked tool, (right) negatively raked tool.

Cutting forces (F_c) and thrust forces (F_t) can be measured using a force measuring dynamometer. Figure 3.4 also depicts how a negatively raked tool increases the thrust force and decreases the cutting force. These forces in any case provides important insight into the mechanics of the cutting operations. For instance, when surface fracture occurs in a cut, the thrust force drops reducing the angle (θ) and the resultant force (F). Owen et al. discussed this results for orthogonal turning and flycutting of Ge [37].

Specific cutting energy (K_s) also provides insight into cutting mechanics for all materials. K_s is calculated from F, a_{doc}, and f_r, as shown in Eq 3.7. When surface fracture is present in a cut, the required energy to remove material is subsequently decreased. This is observed as a decrease in K_s. This research found that increasing V_c will reduce the K_s. The reduction will be reported later in Chapter 4.

$$K_s = \frac{F}{f_r a_{doc}} \qquad (3.7)$$
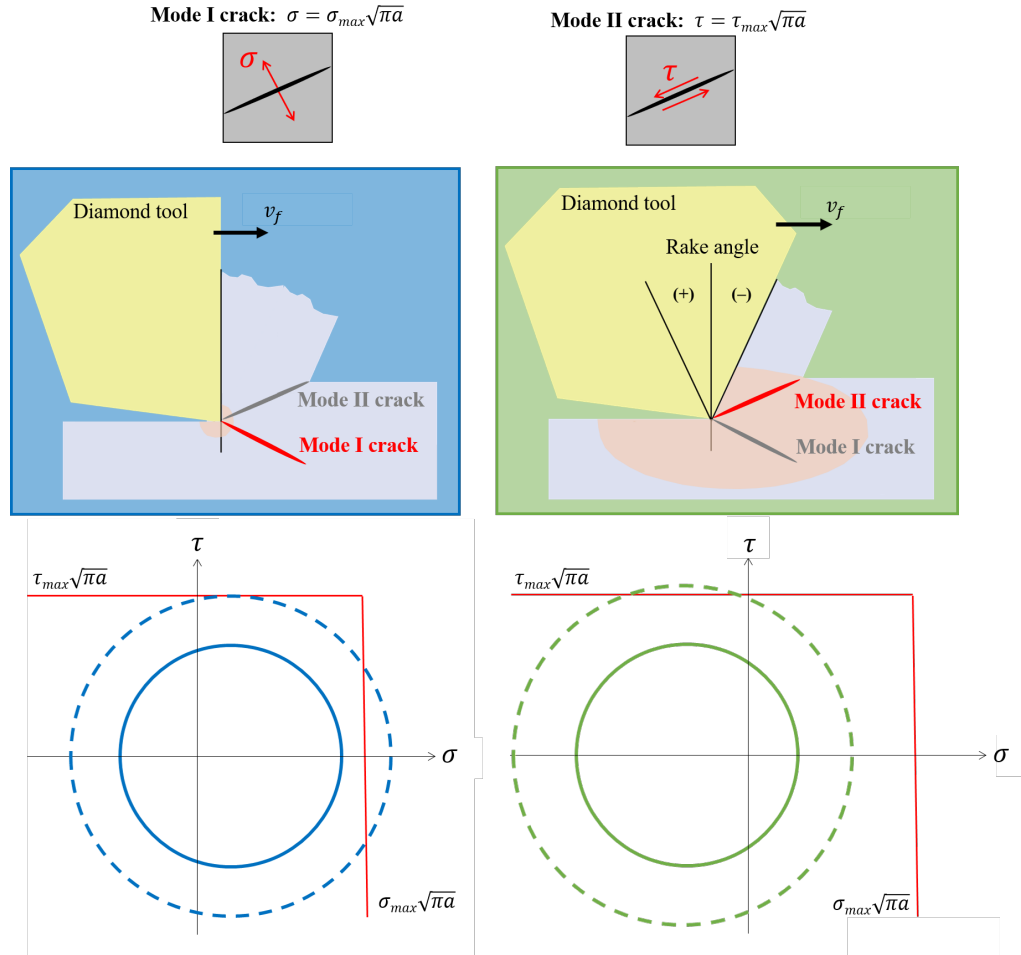
Figure 3.5: Cracking modes were described by Yoshino et al. in [25].

Yoshino et al. described the importance of a negatively raked tool in cutting brittle materials by visualizing the effect through Mohr's circle [25]. Figure 3.5 shows two

modes of crack nucleation from increased stress during a cutting operation. Mode I crack is activated when the tensile stress is excessively large reaching the threshold of $\sigma_{max}\sqrt{\pi a}$. Mode II crack nucleation is activated when shear stress is excessively large reaching the threshold of $\tau_{max}\sqrt{\pi a}$. Increased compressive stress induced by the negatively raked tool shifts Mohr's circle to the left. Thus, decreasing the possibility of Mode I cracks. It is also possible that Mode I crack can occur behind the tool.

3.2.1   Chip Morphology

Chip morphology can also provide insight on the mechanics of ductile-dominate and brittle dominated machining. A face plunge-to-face operation in Ge using a 5 mm R with a -25 degree α revealed ductile-dominated and brittle-dominated chips. The tool was plunged at a 50 nm/rev to a depth of 25 μm. A facing operation continued at 25 μm depth of cut and 15 $\mu m/rev$. Figure 3.6 shows an image of the chips produced. Ductile-dominated chips can be observed from the formation of lamellar chips, as shown in sub-image A in Figure 3.6. Brittle-dominated chips occurred during the facing operation and the subsequent chip can be seen in sub-image C of Figure 3.6. The remaining structure of the chip is held near the apex of the tool tip, where the chip is thinnest. Sub-image B in Figure 3.6 shows the effect of crystal orientation as described by Nakasuji et al. [23]; or, rather, SPDT along damage lobes where brittle behavior is more likely to occur.
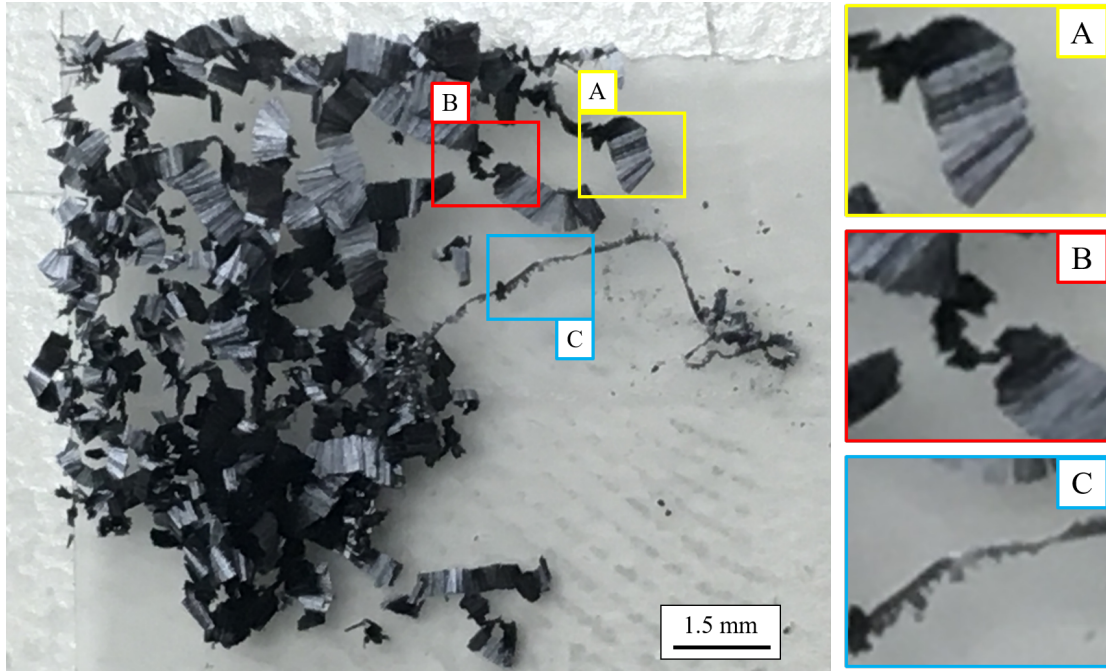
Figure 3.6: A face plunging operation reveals ductile-dominated and brittle-dominated chips.

In another scenario, a 3 mm R with a -25 degree α was used to face Ge. The cut was made at 1 μm depth of cut and 5 $\mu m/rev$. Figure 3.7 shows the chips produced from the operation. Again, a continuous section of the chip is observed where the chip is thinnest (apex of the tool). Increasing damage can also be observed further up the chip.
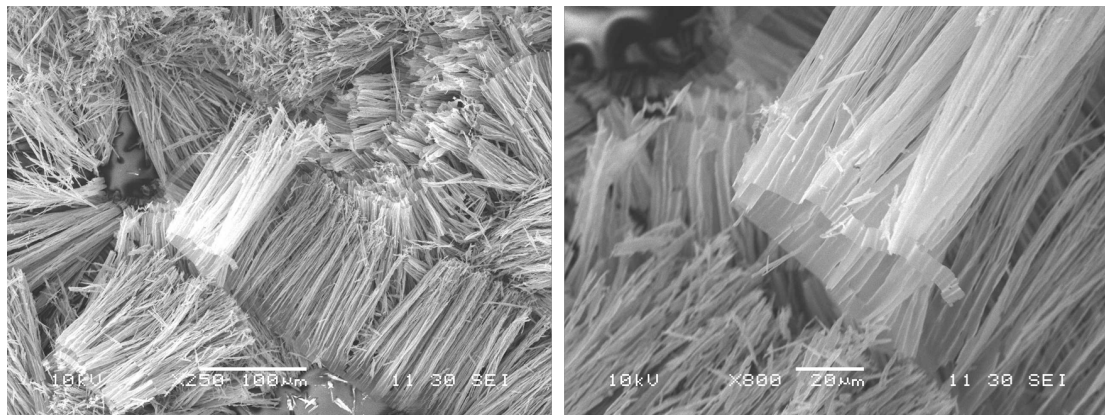
Figure 3.7: SEM image of germanium chips from SPDT.

3.3   Machining Learning

The information reported in this section was used from [42] and copyright permission was provided by the publisher. See Appendix A for the supporting documents.

Chapter 1 introduced the basic desire for utilizing machine learning models in engineering applications. This section on machine learning will specifically cover the background of data-driven machine learning models used in this research. This research focuses on the application and evaluation of machine learning methods to better assist the prediction of surface roughness parameters in Ge and provides a comparison with a well-understood ductile material, Cu.

3.3.1   Basic Background for Machine Learning

Data-driven models prioritize automatic discovery of patterns in the observed data using expert knowledge. Physics-based approaches are motivated by understanding hypotheses about specific physical relationships and correlations among specific parameters. As such, they are not easily able to accommodate complexity and generally rely on simplifying assumptions. In contrast, data-driven approaches, like in machine learning, typically use measurement data to build a model by training without any informing knowledge of the underlying physics. The types of machine learning algorithms differ in their approach and function, i.e. regression, classification, supervised, unsupervised, etc. They also differ by the type of input and output data, and the type of task or problem that they are intended to solve. Supervised machine learning infers a functional relationship from labeled training data consisting of a set of training examples. These training examples, known as output labels, are used to guide the learning process. Unsupervised learning builds a model from a set of data which contains only inputs and no desired output labels. Unsupervised learning algorithms are often used to find structure in the data, such as clusters, by grouping inputs by similarity, or aim at reducing data dimensionality to make a problem more tractable

[54][55]. Among the most popular data-driven approaches, especially for machining applications, are artificial neural networks (ANNs), support vector machines, decision trees, and random forest regression [56][57].

ANNs are a family of machine learning models based on biological neural networks which are used to estimate complex relationships between inputs and outputs [58][59]. Machine learning models, like ANNs, make predictions or decisions without being explicitly programmed to perform the tasks. Like the human brain, ANNs are modeled as a stylized web of interconnected nodes or neurons. The networks are composed of an input layer referred to as input features, one or more hidden layers that process the data with an assigned function, and an output layer that provides one or more targeted outputs. Figure 3.8 illustrates a base-line and deep(er) artificial neural network. A deep or deeper artificial neural network has a larger number of hidden layers (>2).
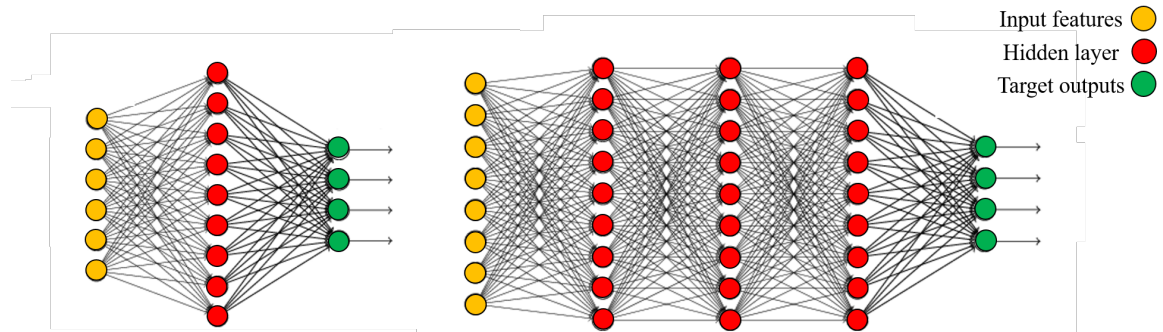
Figure 3.8: (left) base-line artificial neural network, (right) deep(er) artificial neural network.

In feedforward networks, the flow of information takes place in the forward direction. The input features are used to calculate intermediate functions in the hidden layers. The subsequent values from the hidden layers are used to calculate the target outputs. The neurons are the computational building blocks of the artificial neural network. An artificial neural network transforms input features by applying a nonlinear function to a weighted sum of the inputs within the hidden layers. Each neuron

receives inputs from several other neurons, multiplies them by assigned weights, adds them and passes the sum to one or more neurons in feedforward fashion. A hidden layer can apply an activation function to the intermediate-output before passing it to the next variable. Learning is accomplished through iterative optimization of the loss function to adjust the weights such that convergence toward the target output(s) is achieved. A popular optimizer that uses gradient descent optimization, Adam (adaptive moment estimator), aims to calculate the individual adaptive learning rate for each parameter from estimates of first and second moments of the gradients. Adam is typically used in the case of noisy gradients or gradients with high curvatures. The datasets in this research are noisy by nature.

Support vector machines are supervised machine learning models that are used largely for classification, but also prediction [60]. Like artificial neural network, support vector machines infer a function from labeled training data consisting of a set of training examples of paired inputs and outputs. The objective of the support vector machine algorithm is to find a hyper-plane in an N-dimensional space, where N is the number of input features that distinctly classifies the data points. For example, binary classification is performed by finding the hyper-plane that best differentiates between two classes, i.e. maximizes the margin between the hyper-plane and the support vectors, or closest values to the classification margins, illustrated in Figure 3.9. The use of kernels can transform linearly inseparable problems into linearly separate ones.
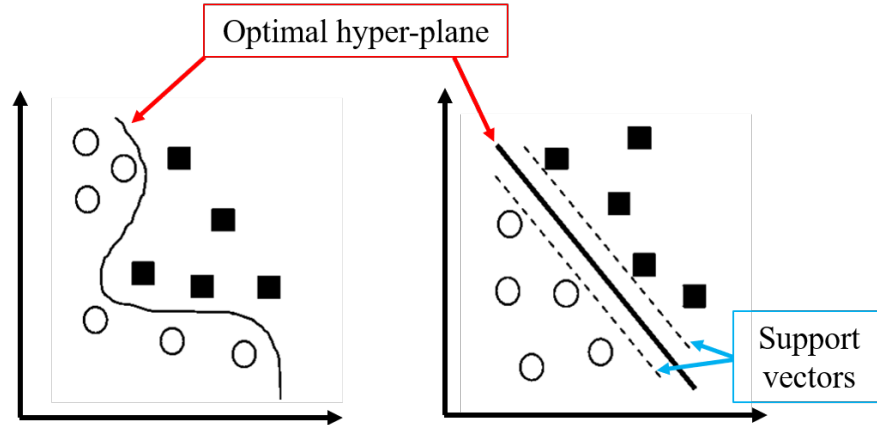
Figure 3.9: Support vector machine example: (left) non-linear and (right) linear by Kernel function.

Decision trees are a non-parametric supervised learning method used for both classification and prediction [61]. The output of a decision tree analysis is represented by a tree-like structure shown Figure 3.10. The algorithm breaks a given dataset into smaller and smaller subsets which form the branches and leaves of the tree. Learning in decision trees is implemented by inferring decision rules from input features at the decision points in the tree structure (non-iterative). Individual decision trees that grow very deep tend to over-fit, exhibiting low bias but very high variance.
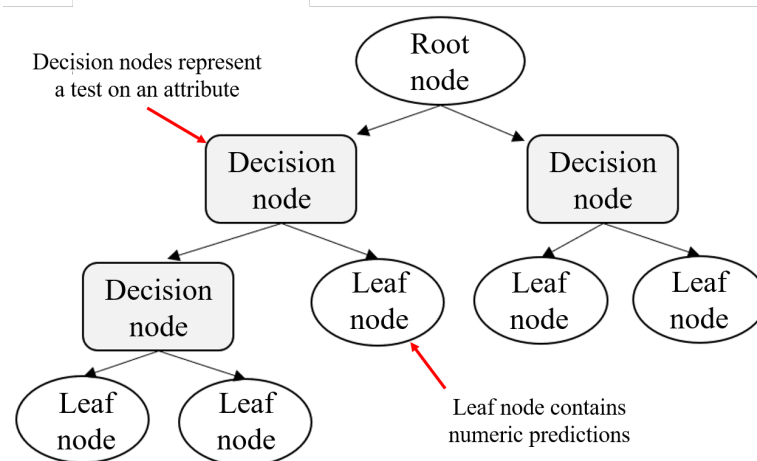
Figure 3.10: Decision tree example.

A meta-algorithm called boosting is often used in conjunction with machine learn-

ing methods to improve performance. Boosting is a method of converting a set of weak learners into stronger learners. A weak learner has a low likelihood of producing the correct target values (<50%). The AdaBoost meta-algorithm, chosen for this research, functions by putting more weight on difficult to classify instances and less on those already handled well [62][63].

Random forest consists of a large number of individual decision trees that operate as an ensemble [57][64]. The underlying idea is to combine many different decision trees, built with different bootstrapped samples of the original dataset, and a pre-specified, but random, number of input features as shown in Figure 3.11. Random forest methods are a way of combining multiple deep decision trees that are trained on different parts of the same training dataset, with the goal of reducing the variance. Random forest methods typically avoid over-fitting. Random forest methods can also handle unbalanced data and are robust to outliers and non-linear data. Generally, an ensemble of a large number of uncorrelated decision tree models will outperform any of the individual models in the ensemble. As with decision trees, random forest methods provide some insight into the relative importance of each feature on the predicted output.
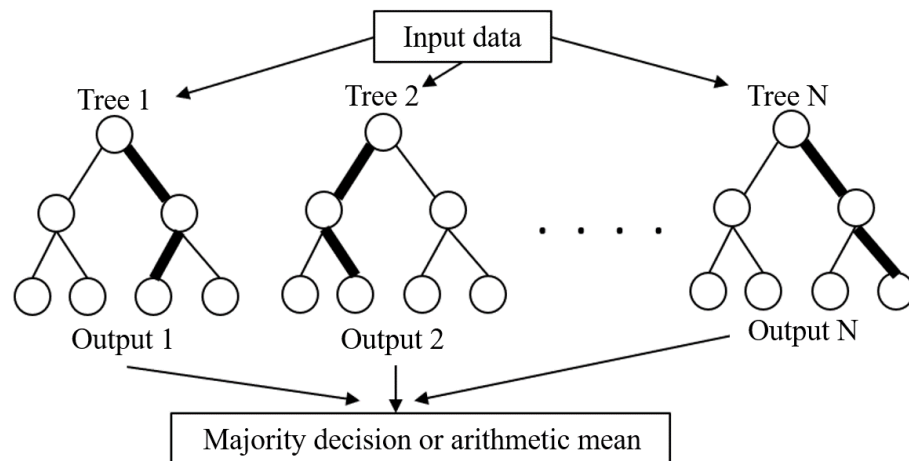
Figure 3.11: Random forest example.

3.3.2   Data Processing
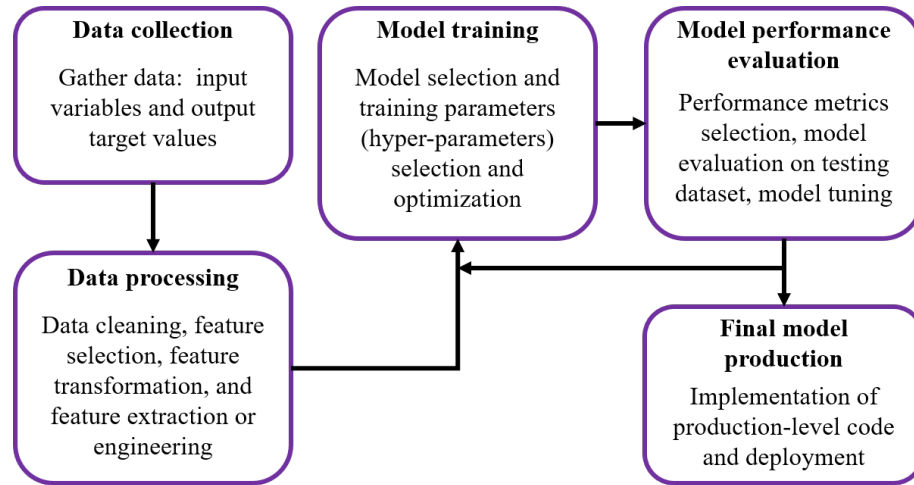
Figure 3.12: Machine learning workflow for creating and employing data-driven models.

Implementation of various machine learning approaches follows a typical workflow, as shown in Figure 3.12. A typical workflow consists of five steps that are applied to model a problem. Data collection (step 1) gathers a set of samples. Each set containing values for input variables describing the problem being modeled. This research specifically uses supervised learning algorithms that have corresponding numeric target output values associated with the inputs. Data processing (step 2) focuses on cleansing and formatting the dataset to be acceptable for the machine learning algorithms through feature selection, feature transformation, and feature extraction. Data cleansing consists in removing or repairing incorrect or missing data, reducing noise, and/or applying data augmentation techniques. Data augmentation techniques synthetically create variation of the existing data to avoid the need for additional data collection and to create a more balanced dataset. Data augmentation is particularly important in classification tasks. Analysis of individual features can lead to removal of unnecessary features. Invariant features are not ideal and are a case for removal. Transforming the remaining features by normalization or scaling can help improve

the machine learning algorithm's accuracy. Extraction of new features from the input data is another technique to engineering a dataset that may be better suited to the machine learning method. The ultimate goal of a machine learning method is to create a model capable of performing well on new data it has not 'seen' during the learning phase. For this reason, in step 2, the resulting, clean dataset is split into non-overlapping training and testing sets. Model training (step 3) includes selecting adequate parameters for the learning algorithm, which is then executed to find patterns in the training data that map the input features to the output target. The product of this step is a machine learning model that captures these patterns and can produce the correct target output when injected with a new input sample. Model performance evaluation (step 4) involves an evaluation of the model generated by measuring its responses to the testing dataset. This uses performance metrics selected for the specific problem. Model hyper-parameters may need to be modified or tuned if results are not yet as accurate as expected. In this case, the process goes back to step 3, as the model must be re-trained using the modified parameters. Lastly, final model production (step 5) involves implementing and deploying the tuned model to operate with live data.

In this research, the Cu and Ge datasets contain features with varying magnitudes, units and range, as listed in Table 2.1 from Chapter 2. Machine learning algorithms are sometimes based on distance measures, e.g. SVM. Large scale differences between features may become dominating and skew the model results. Feature scaling, or standardization, is a type of feature transformation applied to individual features during the data processing step. This normalizes the data to a particular range. It also helps to improve algorithmic accuracy and speeds up computation time. However, normalization should not be applied if the scale difference in features is meaningful. Standardization replaces feature values by their Z-scores by linearly transforming the data to have zero mean and standard deviation of 1. Z-scores are calculated for each

individual feature by Eq 3.8, where μ is the feature mean and σ is the feature standard deviation.

$$Z = \frac{x - \mu}{\sigma} \tag{3.8}$$

The input features of the Cu and Ge datasets have been standardized to ensure good results for the SVM models. The same standardized data was utilized in all the experiments for comparison purposes. The target outputs were not standardized as the magnitude and range of Sa, Sq, and Sz from surface roughness measurements are important to our analysis. Machine learning experiments were implemented in the programming language Python v.3.7.3, utilizing Keras v.2.2.5 neural network API to access the TensorFlow library in the back-end, and various regression algorithms of the Scikit-learn v.0.20.3 machine learning library.

3.3.2.1 Machine Learning Experiments

The task of predicting surface roughness in the Cu and Ge was tackled by performing experiments with four classic machine learning algorithms: decision tree, random forest, adaboost, and support vector regressors, and a set of ANN machine learning architectures differing in the number of hidden layers and neurons per layer. Figure 3.13 provides a summary of the models tested.
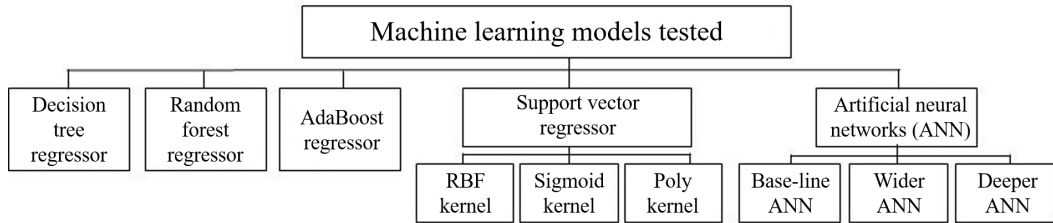
Figure 3.13: Machine learning models tested with Cu and Ge datasets.

Machine learning algorithms have a number of hyper-parameters that require fine-tuning to reduce the generalization error and achieve the best possible model. For example, 'max depth' is the hyper-parameter that controls the maximum number of

children nodes that can grow out from a decision tree before it is cutoff. Experiments were conducted with four decision trees by setting their max depth to 2, 5, 8, and 11. This hyper-parameter should also be tuned when applying the random forest and adaboost algorithms, as they are ensembles of decision trees. Other trial runs were performed using two separate experiments with each of these algorithms by setting max depth to 8 and 11, since these methods are not susceptible to over-fitting. Another hyper-parameter that required tuning was the maximum number of estimators. This had to be tuned before boosting was terminated in adaboost. Random forest also required setting the maximum number of trees (estimators) in the forest. Both algorithms used 100 estimators.

A support vector regressor uses a set of mathematical functions, known as kernels, to take lower dimensional data as input and transform it into a higher dimensional form. This was used to determine the hyper-plane that enables prediction of continuous values, i.e. the target output. Three general-purpose support vector regressor kernels were examined: Gaussian radial basis function (RBF), sigmoid (Sig), and polynomial (Poly). A strong advantage of RBF is that it requires no prior knowledge of the data. The Sig kernel is customarily used as a proxy for neural networks, while the Poly kernel is popular in image processing and was added as a baseline for comparison with the other kernels. The RBF kernel has two free parameters: the regularization parameter C set to 100, and the epsilon value set to 0.1. The epsilon value assigns a safeguard distance from the actual value suffering any penalty during the model training phase. For the Poly kernel, C was set to 1000 and epsilon was kept as 0.1. Additional free parameters for the Poly kernel are coef0, the independent term in the kernel function, which was set to 1. The degree of the polynomial kernel function was set to 3. For the Sig kernel, coef0 was set to -3, while epsilon was kept as 0.1.

Selecting the ANN algorithm and configuration that best fits a dataset is an open

research question that is continuously being investigated by many researchers. Among a growing number of ANN algorithms and optimizers, the Adam optimizer has been selected for the experiments given that is it straightforward to implement, computationally efficient, appropriate for problems with noisy data, and requires little tuning of hyper-parameters. A number of feedforward ANN configurations were tested, i.e. ANNs with different numbers of hidden layers and different numbers of neurons per layer. Six ANN configurations were kept in the final experiment. A basic ANN consisting of a single hidden layer with a small number of neurons is used as a 'Base-line'. ANN configurations named 'Wider' have a single hidden layer but contain a larger number of neurons in this layer. The 'Deeper' ANN configurations have three hidden layers and different number of neurons in these layers. The activation function applied to the hidden layers of the ANNs was the rectified linear unit (ReLU), while a linear activation function was applied to the output layers. The loss function utilized for minimizing the loss of the ANNs by optimizing its weight parameters was the mean squared error (MSE), as shown in Eq 3.9.

$$MSE = \frac{1}{n} \sum_{i=1}^{n} (\hat{y}_i - y_i)^2 \qquad (3.9)$$

The Cu dataset contains only 78 samples, a small dataset by machine learning standards. Thus, the data was randomly split by separating 80% of the samples (62 samples) for training the model and the remaining 20% (26 samples) for testing. The larger Ge dataset has 810 samples and was also randomly split in 80% (648 samples) for training and 20% (162 samples) for testing to allow for better comparison of the accuracy in results against those from Cu data.

3.3.2.2   Evaluation Metrics

There are multiple ways to define the performance criteria for a machine learning model and a number of metrics are typically used. For regression tasks, predictive

capability is typically evaluated using metrics that measure how close predicted values are to the actual measured value. Variance score, root mean squared error, mean absolute error, and R-squared score were computed and used to evaluate the predictive capability of machine learning for surface roughness in diamond turned Ge and Cu. The following explains each of these metrics.

In Eq 3.10, 3.11, 3.12, 3.13, and 3.14, $\hat{y}_i$ corresponds to the value predicted and y_i is the actual measured value expected for the ith example. $\bar{y}$ is the feature mean and Var is the variance, i.e. the square of the standard deviation.

The explained variance regression score (EVS) is a statistical measure, defined in Eq 3.10, of the proportion of variance in a given dataset which is accounted by a regression model. The mean absolute error (MAE) measures the average of the absolute difference between each true value and the prediction. MAE corresponds to an absolute measure of fit and is computed by Eq 3.11.

$$EVS = 1 - \frac{Var(y_i - \hat{y}_i)}{Var(y_i)} \tag{3.10}$$

$$MAE = \frac{1}{n}\sum_{i=1}^{n}|y_i - \hat{y}_i| \tag{3.11}$$

Root mean squared error ($RMSE$) is computed as the square root of the average of the squared difference between each prediction and its actual measured value, as shown in Eq 3.12. Squaring the differences between predictions and true values makes $RMSE$ give higher weight to larger outliers, which is a useful property for data analysis. Similarly to MAE, $RMSE$ is in the same units as the target. The maximum residual error ($MaxError$) measures the worst-case error between the predicted (target) value and the actual measured value. This is a useful property when very high errors can result in catastrophic or expensive events. $MaxError$ is shown in Eq 3.13.

$$RMSE = \sqrt{\frac{\sum_{i=1}^{n}(\hat{y}_i - y_i)^2}{n}} \tag{3.12}$$

$$MaxError = max(|y_i - \hat{y}_i|) \tag{3.13}$$

R-squared (R^2), or coefficient of determination, is the statistical measure of the proportion of the variance in the dependent (target output) variable that is predictable from the independent (input features) variables. Typically R^2 values vary between 0 and 1. An R^2 value equal to 0 indicates that the model is not capable of predicting the target from the given input features. On the other hand, an R^2 value equal to 1 means that the target output can be predicted without error from the input features. In rare cases, when the selected model fit is worse than a horizontal line R^2 values can be negative. Thus, a negative value indicates that the mean of the data is a better predictor than the selected model.

$$R^2 = 1 - \frac{\frac{1}{n}\sum_{i=1}^{n}(y_i - \hat{y}_i)^2}{\frac{1}{n}\sum_{i=1}^{n}(y_i - \bar{y})^2} \tag{3.14}$$

Performance metrics were computed for both the training and test phases of model building. A machine learning model 'learns' a system's behavior from input-output pairs of samples it 'sees' processes during the training phase. The model's accuracy is evaluated during the testing phase by measuring the error of its predictions when presented with input samples it has not seen before. The corresponding target output value is also unknown to the model. Model evaluation results utilizing these metrics are presented in the Chapter 5.

CHAPTER 4: EXPERIMENTAL RESULTS

4.1   Surface Measurement Uncertainty

This section focuses reporting the results from the uncertainty analysis in measuring surface roughness on Ge that is machined using a single-point diamond tool. In particular, the areal surface roughness (Sa) and the root mean squared areal surface roughness (Sq) are considered as the measurands for the analysis. Since single-point diamond turned surfaces are not considered as homogeneous, it is anticipated that the texturing on the surfaces will drive up the uncertainty in surface topography repeatability (STR) analysis. Additionally, since Ge is a brittle material, it is expected to have surface fracture due to aggressive turning parameters, which is hypothesized to further increase the uncertainty in the STR analysis. It was assumed for the purpose of this research, that the STR analysis will capture the dominating uncertainty for the measurements as previously discussed. A SiC CVD reference standard was used as a comparator to the effects from the machined surfaces.

4.1.1   Uncertainty Analysis Results

The uncertainties determined from Method 1 are summarized in Table 4.1. The three surfaces SiC-CVD, Ge-1, and Ge-2.1 all seem to have minimal uncertainty from the STR analysis. The surface Ge-2.2 had a minor amount of surface damage due to brittle fracture. The surface Ge-3 had severe surface fracture damage. These two surfaces had larger associated uncertainties, where Sq more vividly captured the surface defects present in the two surfaces.

Table 4.1: Method 1 - STR analysis results for 50 measurements.

	SiC-CVD	Ge-1	Ge-2.1	Ge-2.2	Ge-3
$STR\ Sa$ (nm)	0.1	0.1	0.1	0.2	1.0
$STR\ Sq$ (nm)	0.2	0.1	0.2	1.6	4.7

Figure 4.1 shows the effect of surface fracture as the number of measurements increases. This ever growing increase in the $STR\ Sa$ could be attributed to the drift motions of the stages over time. The $STR\ Sq$ results depicted the same relationship with presence of brittle fracture in the samples surface. It should also be pointed out that the values reported in this graph were rounded up to 1 decimal place considering the units of nm.
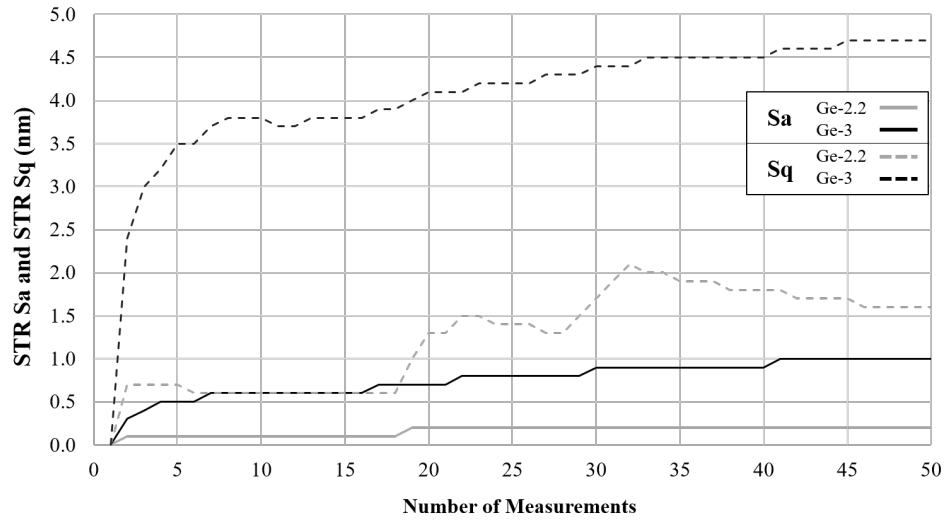
Figure 4.1: Method 1 - STR analysis.

Table 4.2: Method 2 - STR analysis results for 50 measurements.

	SiC-CVD	Ge-1	Ge-2.1	Ge-2.2	Ge-3
Mean Sa (nm)	0.2	0.4	2.7	2.9	21.9
Mean Sq (nm)	0.2	0.5	3.2	5.4	48.1
STR Sa (nm)	0.1	0.1	0.1	0.1	0.3
STR Sq (nm)	0.1	0.1	0.1	0.8	0.7

The mean values for Sa and Sq are summarized in Table 4.2 for Method 2. The standard deviations were computed from the PDFs of each surface. Major outliers in the PDFs were observed for Ge-2. These are likely attributed to the surface fracture in the surfaces.

Figures 4.2, 4.3, and 4.4 show the PDFs for Sa and Sq estimates based on Method 2. The plots are scaled with the same vertical axis bounds to better compare the results. The skewness and kurtosis values are reported in Table 4.3. Based on the results in Table 4.3, the PDFs are not normally distributed. The surface Ge-2.2 was largely effected by the surface defects present on the surface as the skewness and kurtosis indicate. The surface Ge-3 interestingly shows a similar distribution as the other surfaces. The surface defects for Ge-3 were better distributed as compared to Ge-2.2.

Table 4.3: Reported skewness and kurtosis for Method 2 PDFs.

	SiC-CVD	Ge-1	Ge-2.1	Ge-2.2	Ge-3
Skewness Sa (nm)	0.14	-0.73	0.09	2.04	-0.98
Skewness Sq (nm)	0.18	-0.87	0.06	1.87	-1.03
Kurtosis Sa (nm)	3.24	3.92	3.04	5.82	3.46
Kurtosis Sq (nm)	3.16	4.30	3.05	5.04	3.64
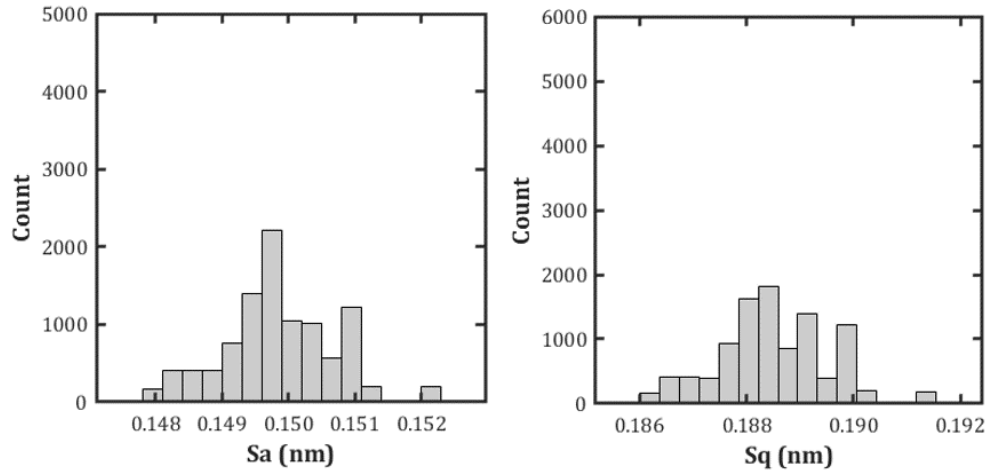
Figure 4.2: *Sa* and *Sq* PDFs for SiC-CVD.
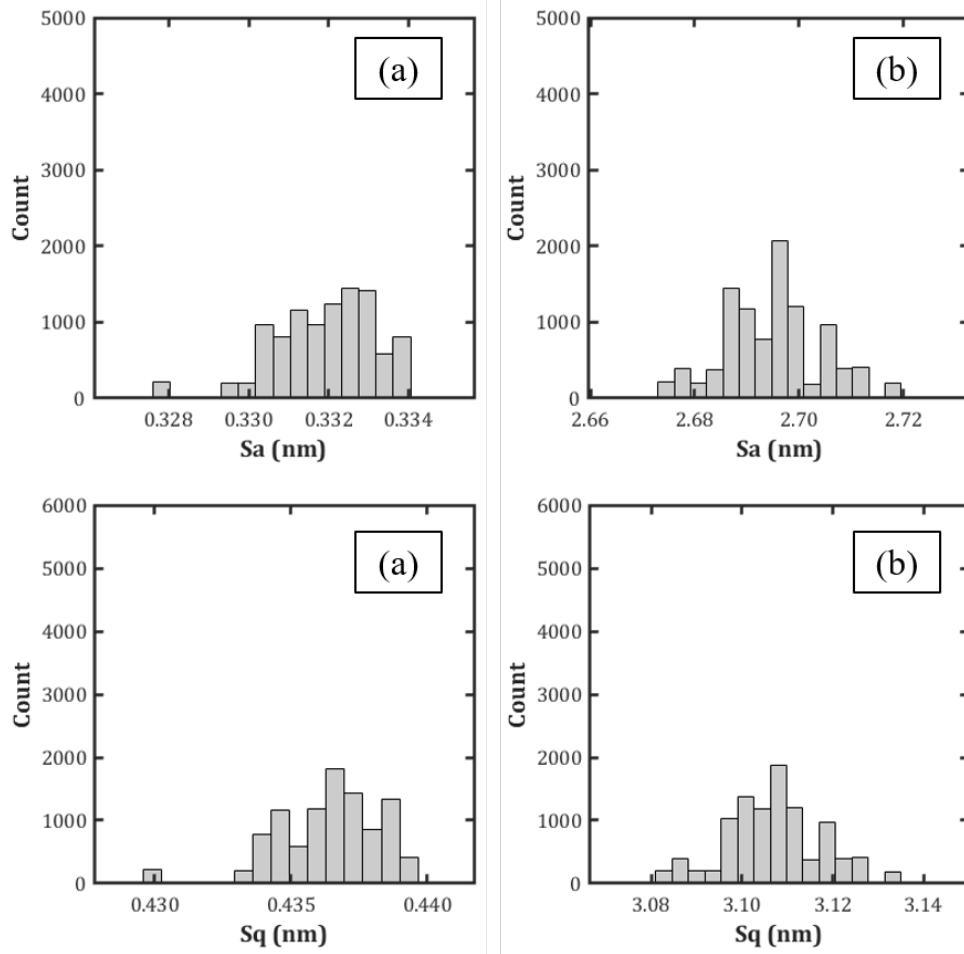
Figure 4.3: *Sa* and *Sq* PDFs for (a) Ge-1 and (b) Ge-2.1.
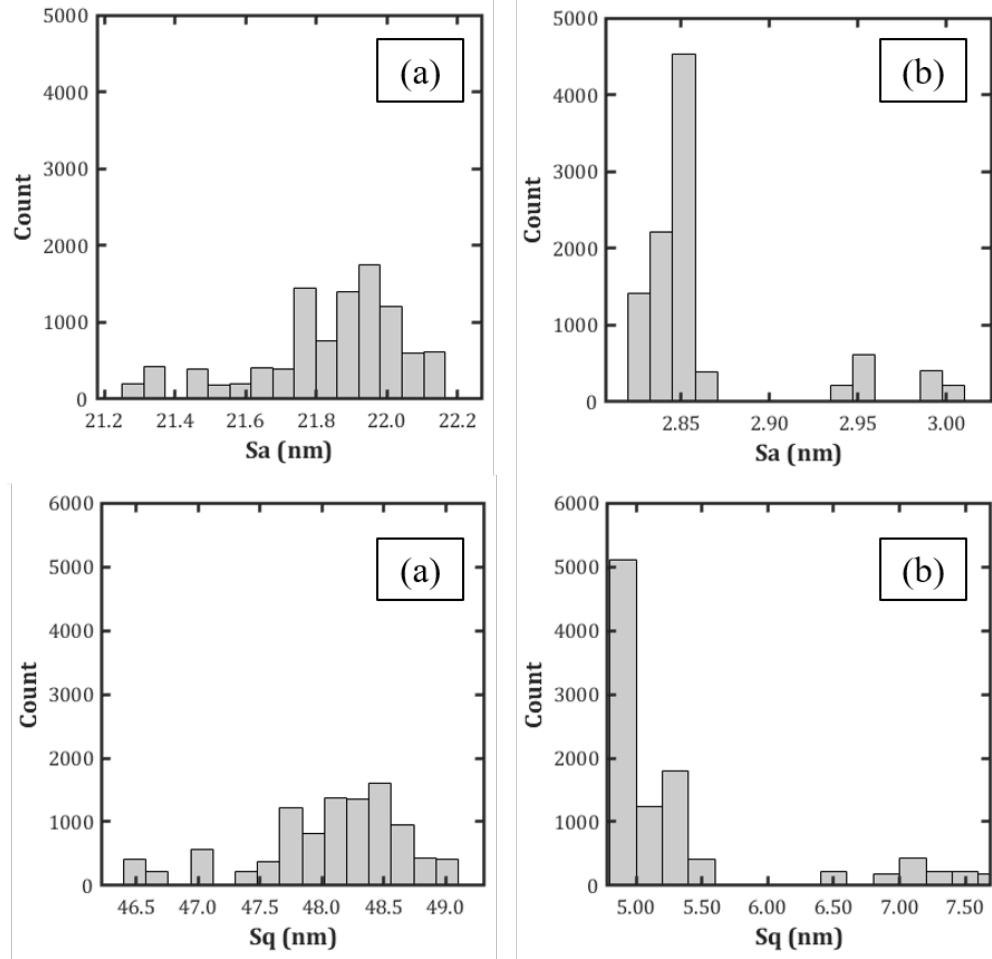
Figure 4.4: Sa and Sq PDFs for (a) Ge-2.2 and (b) Ge-3.

4.2 Single-Point Diamond Turning

4.2.1 General Force Results in Germanium

This section will report on the cutting forces F_c and thrust forces F_t measured while single-point diamond turning Ge. The major crystal orientation of the Ge is (100) for these results. The following machine parameters were held constant for this set of experiments: V_c at 2 m/sec and a_{doc} at 25 μm. Tools with R of 0.5, 1.0, and 5 mm with an α of -25 degrees were used.

Figure 4.5, 4.6, and 4.7 shows F_c and F_t plotted against f_r for each of the tools. The standard deviation of the forces are plotted as a dashed line. For Figure 4.5 (R of 0.5 mm), surface fracture began to appear for f_r values greater than 1.1 μm/rev and became more prevalent after f_r exceeded 1.75 μm/rev. As the surface fracture increased, so did the standard deviation in the force plots. For Figure 4.6 (R of 1 mm), surface fracture began to appear for f_r values greater than 2.6 μm/rev.
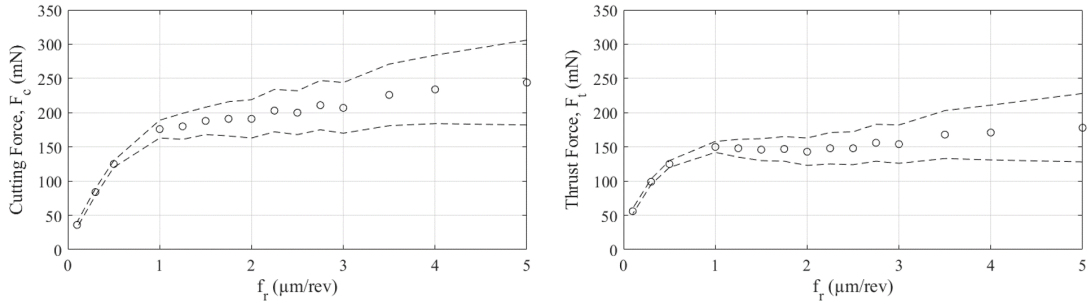
Figure 4.5: R of 0.5 mm for (left) F_c versus f_r and (right) F_t versus f_r.
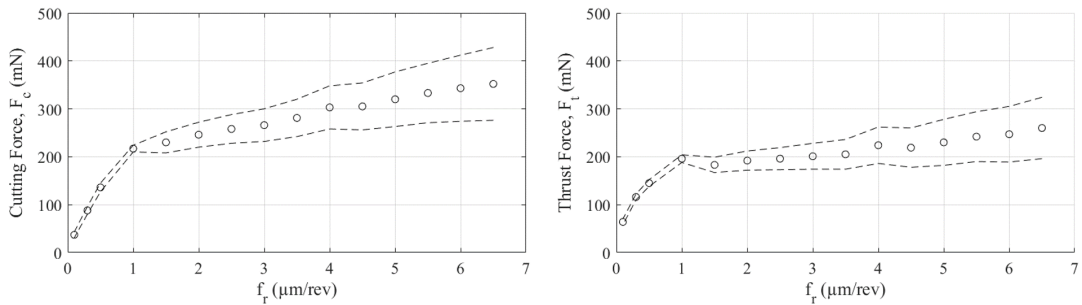
Figure 4.6: R of 1.0 mm for (left) F_c versus f_r and (right) F_t versus f_r.

The force results from 5 mm R, as shown in Figure 4.7, never experienced surface fracture; however, the standard deviation increased following 2 μm/rev.
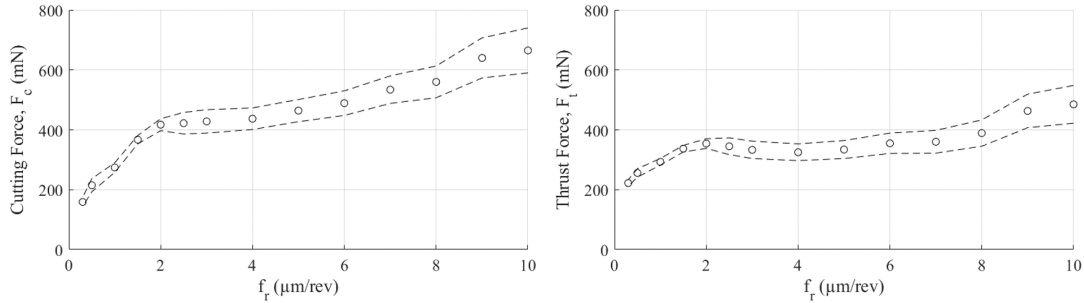
Figure 4.7: R of 5.0 mm for (left) F_c versus f_r and (right) F_t versus f_r.

The resultant forces F and angle resultant Θ for all three tools is shown in Figure 4.8. As previously mentioned, the 5 mm R did not exhibit surface fracture for f_r values between 0.3 to 10 μm/rev. Though there is still a decrease in Θ to a similar degree as the other two tools that did exhibit visible surface degradation. With this in mind, the decrease in angle could be considered in two parts: (1) larger chip loads increase the F_c more quickly than F_t, and (2) the larger chips are experiencing more brittle fracture within the chip.
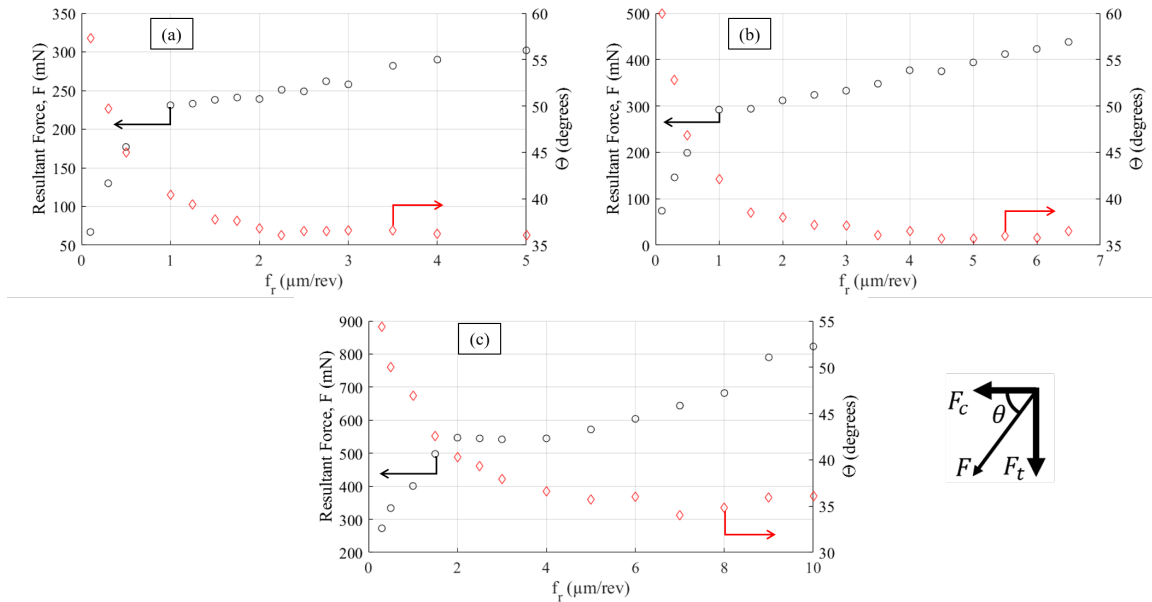
Figure 4.8: F and Θ for (a) R of 0.5 mm, (b) R of 1.0 mm, R of 5.0 mm.
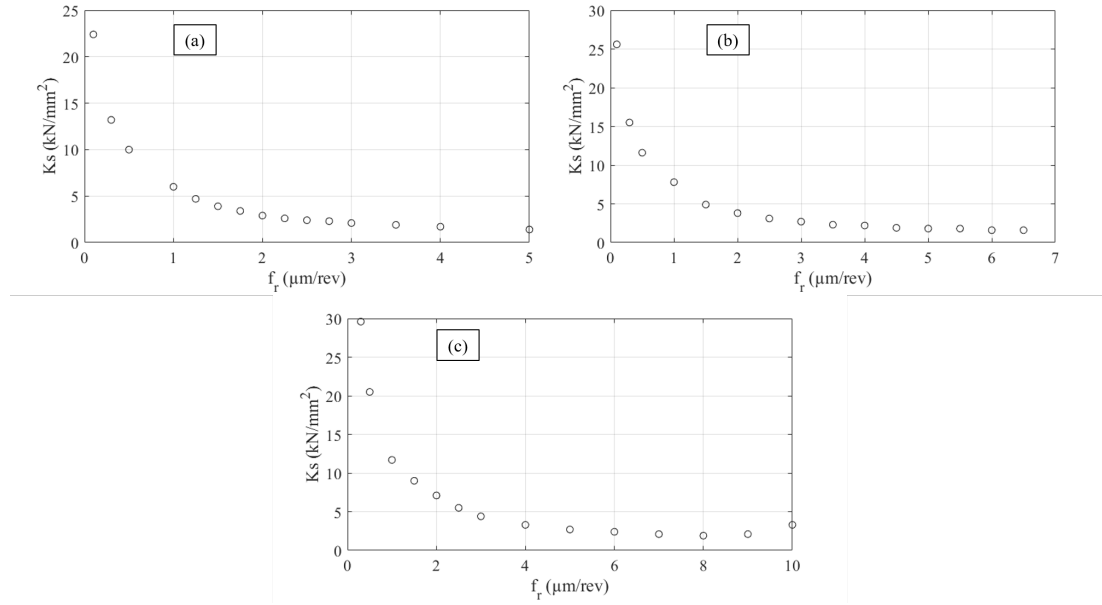
Figure 4.9: Ks versus f_r for (a) R of 0.5 mm, (b) R of 1.0 mm, R of 5.0 mm.

Even though the overall chip thickness decrease with a larger tool nose radius, the energy required to remove the material is higher. The undeformed chip thickness for the 5 mm tool is about 3 times smaller than that of the 0.5 mm tool. Another consideration is that because the chip is thinner for the 5 mm tool, there is less fracture generated within the chip.
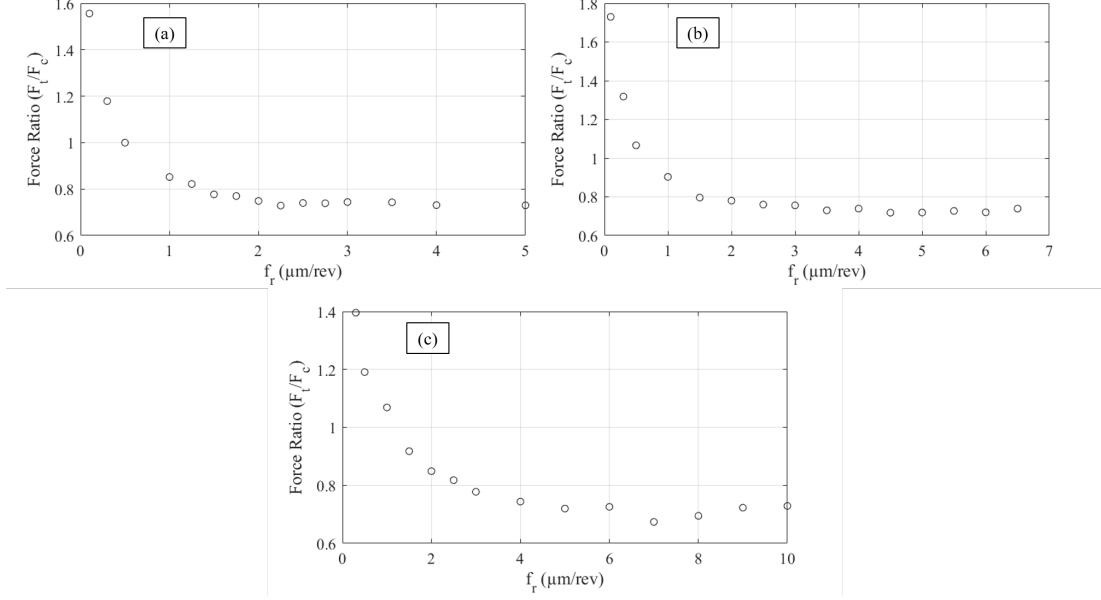
Figure 4.10: Force ratio for (a) R of 0.5 mm, (b) R of 1.0 mm, R of 5.0 mm.

Figure 4.10 shows the force ratio plots for the three tool nose radii. All three plots follow a similar trend, but one noticeable difference is observed in Figure 4.10 plot (c). Here there seems to be a stronger intrinsic effect as the chip thickness is much thinner than for the other two radii.

4.2.2   Major Crystal Orientation Effect

Ultra-precision machining of brittle materials is a timely process, as most machine input parameters are conservative. This is mostly due to the introduction of brittle fracture that has been discussed throughout this research. A reduction in surface integrity ultimately will degrade the quality of the part produced and could also impede optical performance and fatigue-life depending on the application of the final product.

There are two major crystal orientations for single-crystal Ge: (100) and (111). Since Ge has (ideally) isotropic optical properties, it would be important to know what major crystal orientation of Ge is the most cost-effective choice for manufacturing. The anisotropic mechanical properties are equally important to identify. In general,

optical-grade Ge with a major crystal orientation of (111) is procured more often and kept readily in-stock at vendors across the nation. However, as this research will show in this section, Ge with a major crystal orientation of (100) exhibits higher material removal rates than the (111) orientation. Thus, significantly reducing machine time for roughing parameters in single-point diamond turning scenario.

Figure 4.11 shows a comparison of maximum f_r allowed prior to brittle fracture based on R and the major crystal orientation. The a_{doc} and V_c were held constant at 25 μm and 2 m/sec, respectively. Three R were used (0.5 mm, 1.0 mm, and 5.0 mm) with an included α of -25 degrees. The major orientation (100) can achieve approximately twice the material removal rate compared with (111).
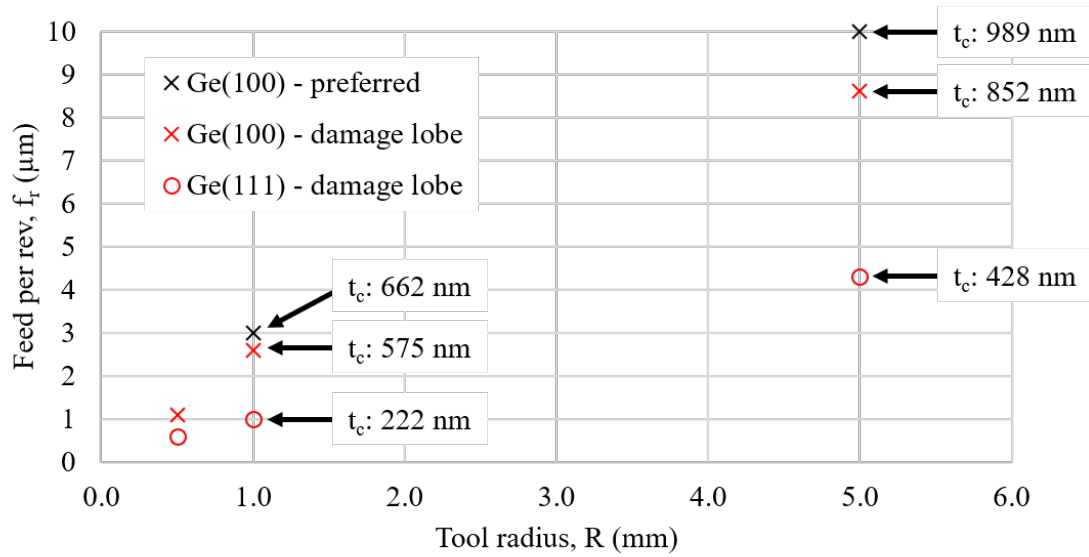
Figure 4.11: Maximum f_r prior to brittle fracture based on R and major crystal orientation.

4.2.3   Cutting Speed in Turning Germanium

Cutting speed V_c in diamond machining of Ge has not been a major focusing point in ductile-dominated machining of Ge. In fact, Blake and Scattergood published a paper in 1989 concluding that there was insufficient evidence V_c had an impact on surface integrity. This was the only account of the to date based on a current literature search. This section will provide the results that showcase the beneficial effects of V_c in diamond turning of Ge.

V_c was varied from 0.25 to 24 m/sec in SPDT of Ge. The a_{doc} and f_r were held constant at 20 μm and 4 μm/rev, respectively. 4 μm/rev was chosen as surface fracture was present at 2 m/sec. The goal of this experiment was to determine whether or not surface fracture was suppressed by an increased V_c. Five repetitions were completed for thoroughness to ensure that the results were repeatable.

Force data was also collected during the cutting operations using the Kistler 9256C1. The cutting (tangential) force F_c and thrust (normal) force F_t were analyzed to get a better understanding the mechanics of the operation. Figure 4.12 shows F_c and Figure 4.13 shows F_t. As V_c increases from 2 m/sec and onward, the forces begin to drop and so does the standard deviation. The standard deviation of the force data is plotted along with the F_c and F_t data. The narrowing of the standard deviation tends to be a good sign, as it indicates a reduction or absence of surface fracture. The drop in forces that is observed at lower values of V_c (i.e. 0.25 m/sec) is from the increase in surface fracture. Less energy is required to remove material with the assistance of fracturing.
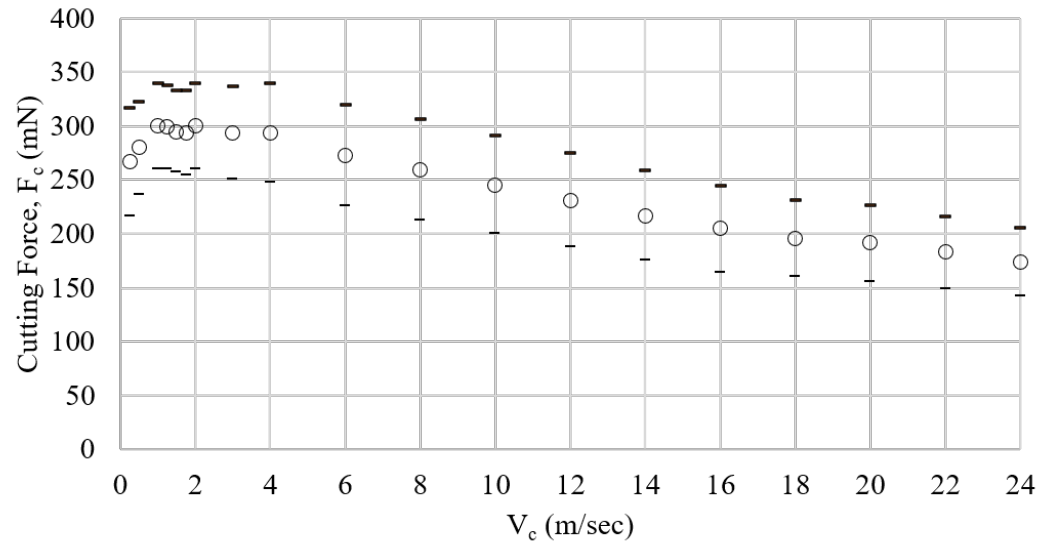
Figure 4.12: Cutting force F_c versus cutting speed V_c.
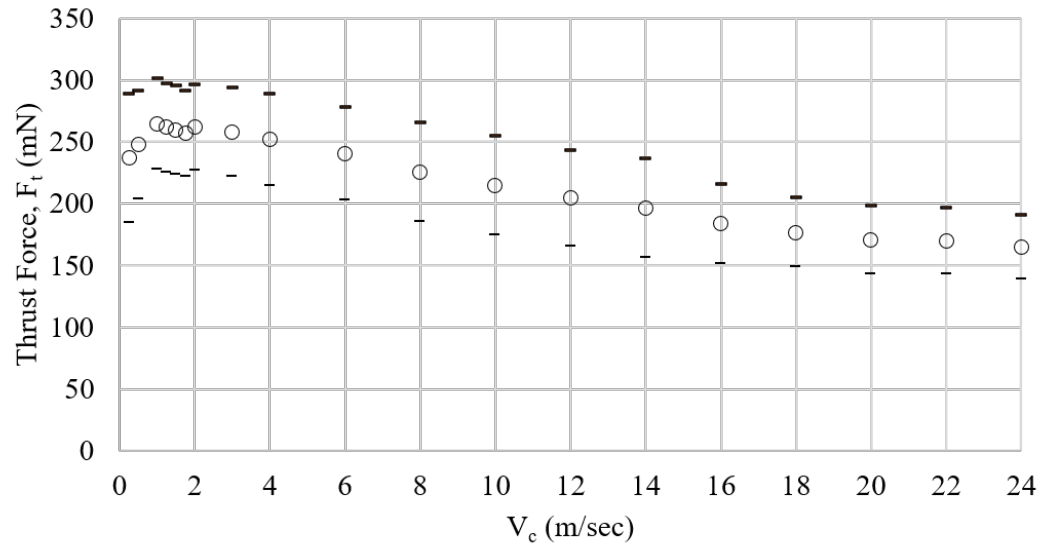
Figure 4.13: Thrust force F_t versus cutting speed V_c.

The resultant force F and resultant angle Θ were plotted against V_c, as shown in Figure 4.14. Here Θ is the angle between F and F_c. The increased V_c begins to increase Θ, which indicates that less tensile force is resolved into the surface.
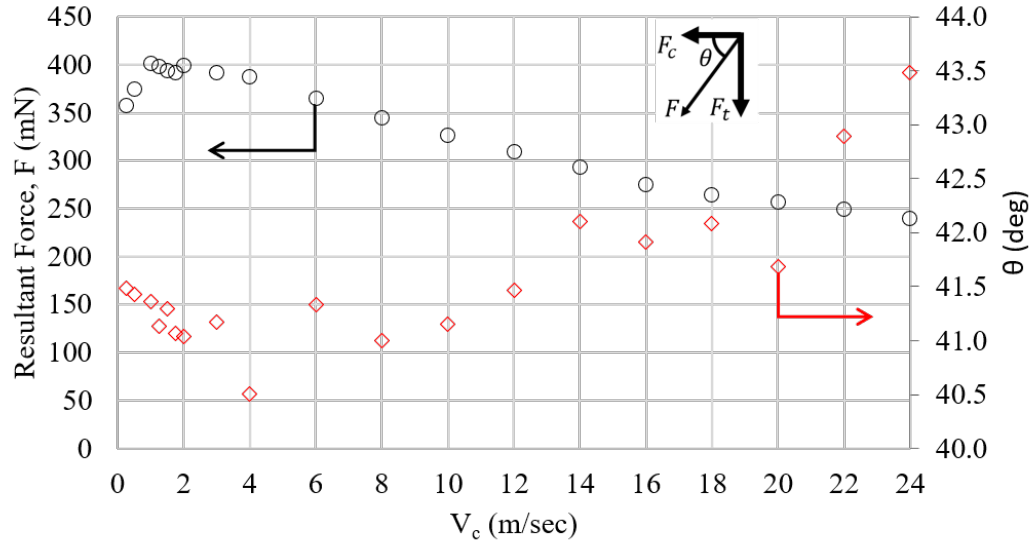
Figure 4.14: Resultant force F and angle Θ versus cutting speed V_c.

The specific cutting energy K_s is shown in Figure 4.15. Again, the same relationship is observed here, where the K_s decreases with increased V_c. The drop in forces and specific cutting energy is consistent with ductile metal cutting at high V_c values.
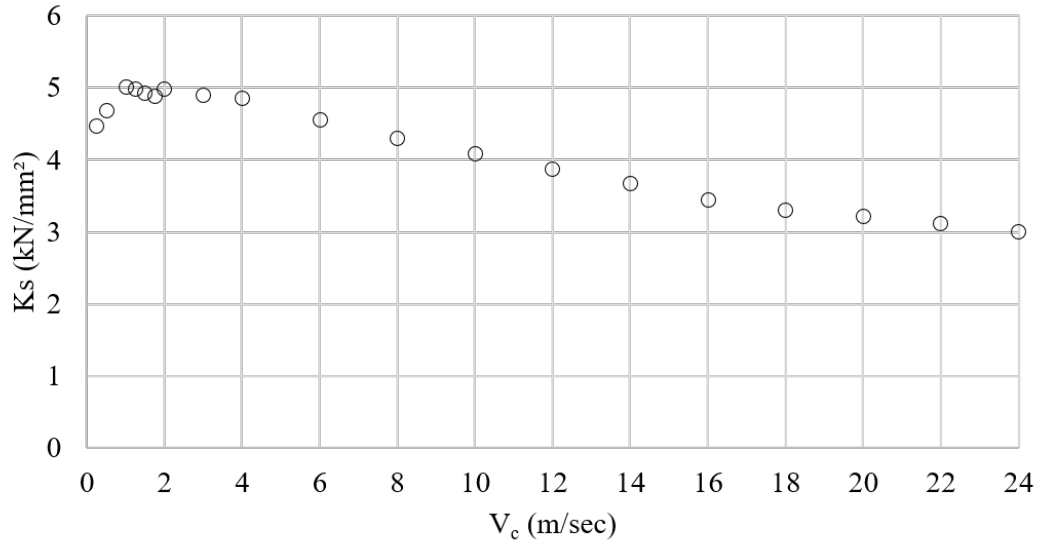
Figure 4.15: Specific cutting energy K_s versus cutting speed V_c.

Finally, the force ratio versus V_c is shown in Figure 4.16. One hypothesis to explain the observed increase in the force ratio is by relating it to an intrinsic effect. This means that the material being removed is likely experiencing ploughing rather than shearing. An alternative hypothesis is that the more rapid loading/unloading rate is assisting a phase transformation from diamond-cubic Ge to a metallic (β-tin) phase of Ge, which is more ductile by nature. In either case, the mechanism of material needs to be examined further by analyzing the subsurface and chips from machining.
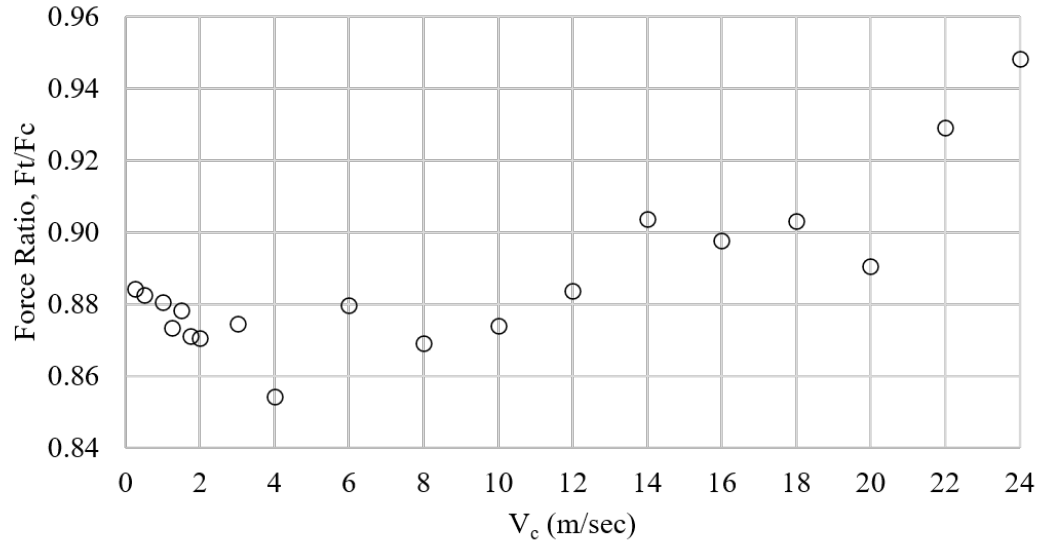
Figure 4.16: Force ratio $\frac{F_t}{F_c}$ versus cutting speed V_c.
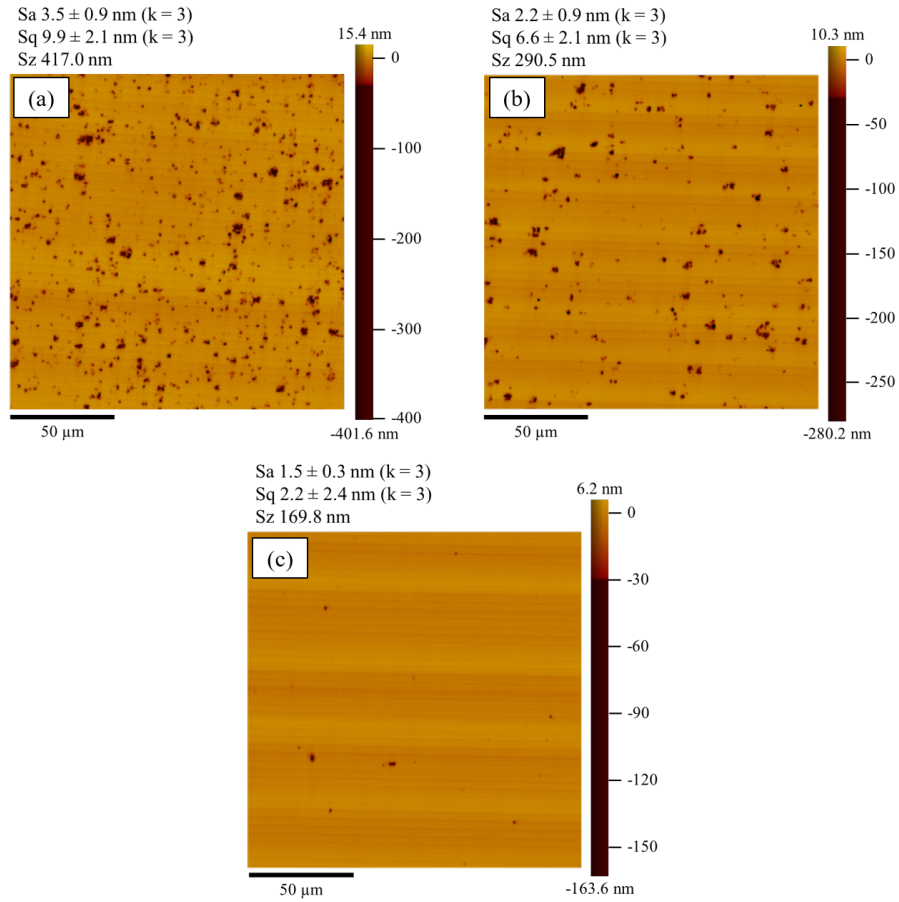
Figure 4.17: Single-point diamond turned germanium at V_c values of (a) 0.25 m/sec, (b) 10 m/sec, and (c) 24 m/sec.

Figure 4.17 shows three example surfaces from the V_c experiment. A larger network of cracks produces more pitting that also goes deeper into the surface when V_c is 0.25 m/sec. As V_c increases to 10 and 24 m/sec, there is likely a decrease in the density of crack nucleation, thus generating fewer surface defects. Surface fracture generation is fairly agnostic to the depth of cut in turning and flycutting of Ge. That being said, it is safe to say that a small variation in the depth of cut ($\pm$ 6 nm) observed in the feed direction did not alter the mechanics of the cut. In the case of turning, the feed per revolution f_r is a much more sensitive parameter.

It is clear that a higher cutting speed provides a means for improved material removal rates. A 1 mm R will begin to produce surface fracture around 2 μm/rev at low values of V_c ($<$10 m/sec). Higher V_c values increase the maximum allowable f_r before fracture occurs.

4.3   Single-Point Diamond Flycutting

As previously mentioned diamond flycutting operation used a 1 inch arbor mounted to a 60,000 rpm air-bearing spindle. The experiments conducted using this setup had the goal of vary the cutting speed V_c to determine if a speed effect reduces brittle fracture on the surface.

4.3.1   Cutting Speed in Flycutting Germanium

As previously discussed in the single-point diamond turning results, a speed effects was observed in a continuous cutting operation. Those results concluded that cutting speeds higher than 10 m/sec assisted in suppressing brittle fracture in the surface. A similar hypothesis in interrupted cutting (flycutting) was therefore expected to be true. However, unlike the turning operation, the flycut surfaces were all free of fracture. In order to observed the effect from varying the V_c, the exits of the patches were examined using a CSI.

Recall the patches flycut in Ge were 0.5 mm by 2 mm, such that force data and surface data could be collected from the resulting surfaces. Also recall that the V_c was varied from 10 to 40 m/sec, while a_{doc}, f_r, and R were constant. The rotation of the flycutter in combination with the feed direction makes this operation similar to a climb milling operation, such that the tool enters the cut where the chip is largest.
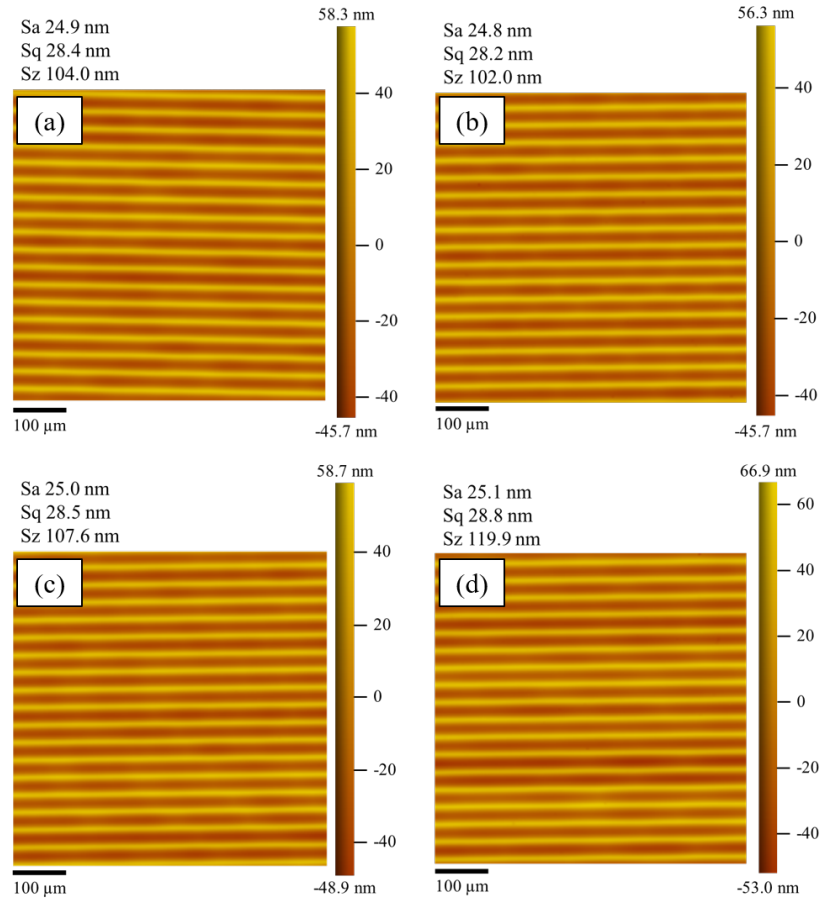
Figure 4.18: Flycut germanium at V_c values of (a) 10 m/sec, (b) 20 m/sec, (c) 30 m/sec, and (d) 40 m/sec.

Figure 4.18 shows the four surfaces from varying the V_c from 10 to 40 m/sec. Notice that all three surfaces have very similar Sa and Sq values, which also overlap if the uncertainty in the measurements is included $\pm$ 0.3 nm. This does not necessarily mean that there is no residual damage underneath the surfaces.
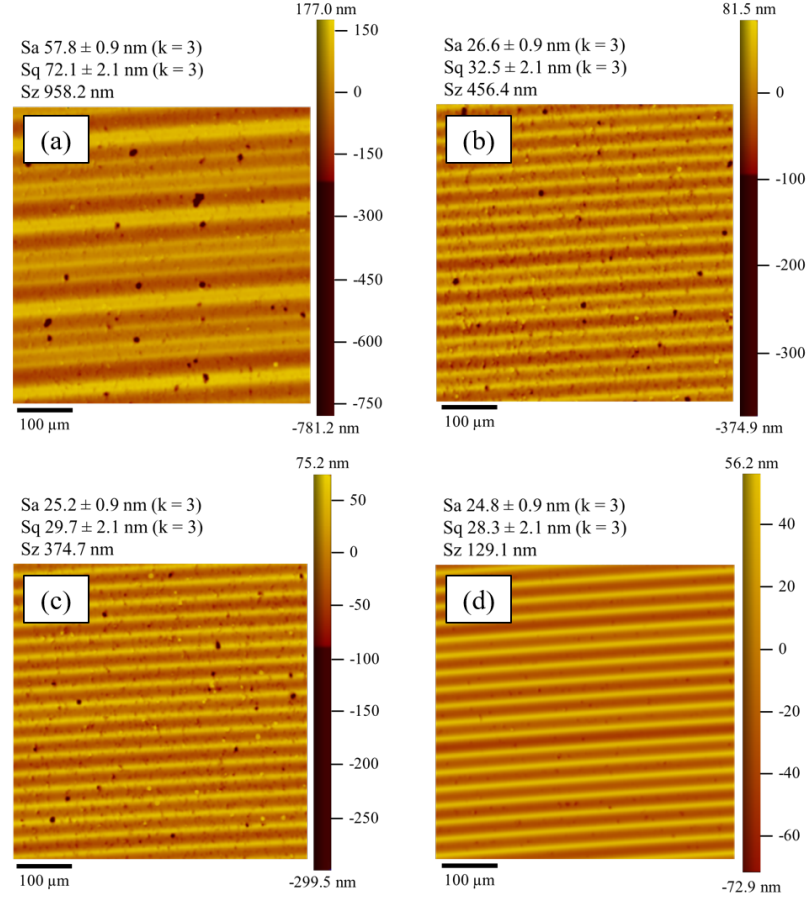
Figure 4.19: Flycut exit in germanium at V_c values of (a) 10 m/sec, (b) 20 m/sec, (c) 30 m/sec, and (d) 40 m/sec.

Figure 4.19 shows the exit of the cuts for the four surfaces that were shown in Figure 4.18. The exit of the cuts provide the final visual evidence that V_c does indeed influence the cutting mechanics and does impact the damage residing in the surface. As V_c is increased from 10 to 40 m/sec, the depth of damage perceived as surface fracture, and represented here through Sz, decreases from $\sim$1.0 μm to $\sim$0.1 μm.

4.4   Polishing

4.4.1   Magneto-Rheological Finishing Results

Single point diamond turning has been a method of manufacturing precision parts for optical molds or directly manufacturing of symmetric lenses. The manufacturing of IR optics using brittle materials like germanium and chalcogenide glass can be tricky due to their brittle nature. Obtaining reasonable methods for evaluating surface and subsurface damage is important to ensure the quality of the manufactured optics. Some methods like confocal Raman spectroscopy is extremely limited on the depth of penetration it can observe into the surface provided the right laser source is used. For example, a 532 nm laser can observe damage and disorder only down to 30 nm or less in Ge. Two alternative methods using an MRF machine were used to evaluate damage depth in single-point diamond turning of Ge. These two methods are the MRF spotting technique and a full aperture polish using the MRF machine. The major difference between these two methods are: (1) the spotting technique polishes a single location on the workpiece for a prescribed amount of time; (2) full aperture polishing includes a rotating and rastering workpiece over the flowing ribbon of the MRF machine. The basic hypothesis behind the first method is that the MRF fluid is removing material from the surface exposing the subsurface damage and eventually the polishing will reach a non-damaged surface. The second method addresses the process of removing subsurface damage from a diamond turned surface; however, the findings focus more on the mitigation of mid-spatial frequencies. For the purpose of this research, it was assumed that the MRF fluid is not causing additional damage or fracture propagation into the surface.

4.4.1.1   Sample 1 - Surface Damage Evaluation

Sample 1 was initially diamond turned as specified earlier. The damage introduced into the surface and subsurface from the SPDT operation was evaluated through the

MRF spotting technique. Figure 4.20 shows sample 1 on the NexView stage. The workpiece was aligned using the fiducial marks presented on the surface of the part. The fringes were 'fluffed' such that a single fringe engulfed the field of view.
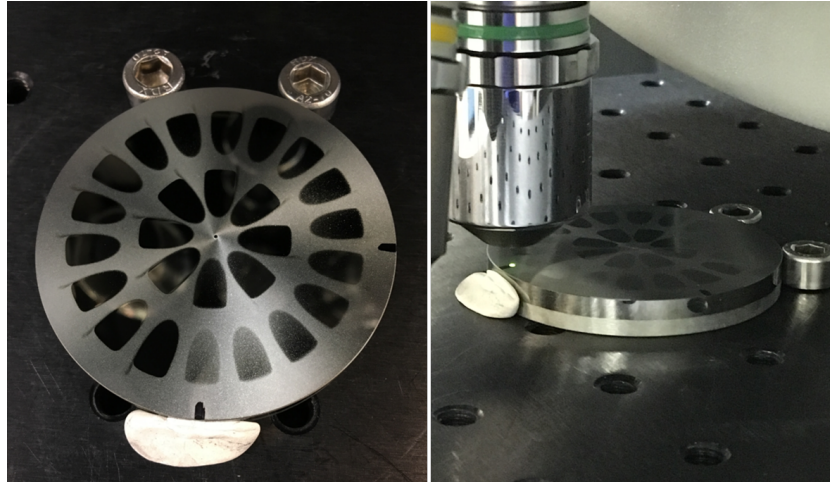
Figure 4.20: Sample 1 - MRF spotting technique.

The MRF spotting technique completed on sample 1 shows some promise in estimating the subsurface damage in SPDT germanium. However, in order to have complete confidence in the process, the spots were etched using 3% hydrogen peroxide. The etch rate was determined to be approximately 1 nm/min while using an ultrasonic bath. The ultrasonic bath assisted the etch rate. The sample was etched for 25 minutes. Thus, approximately 25 nm were removed. Figure 4.21 shows the original diamond turned surface and etched surface. The etching process revealed more damage from the network of fractured surface surface.
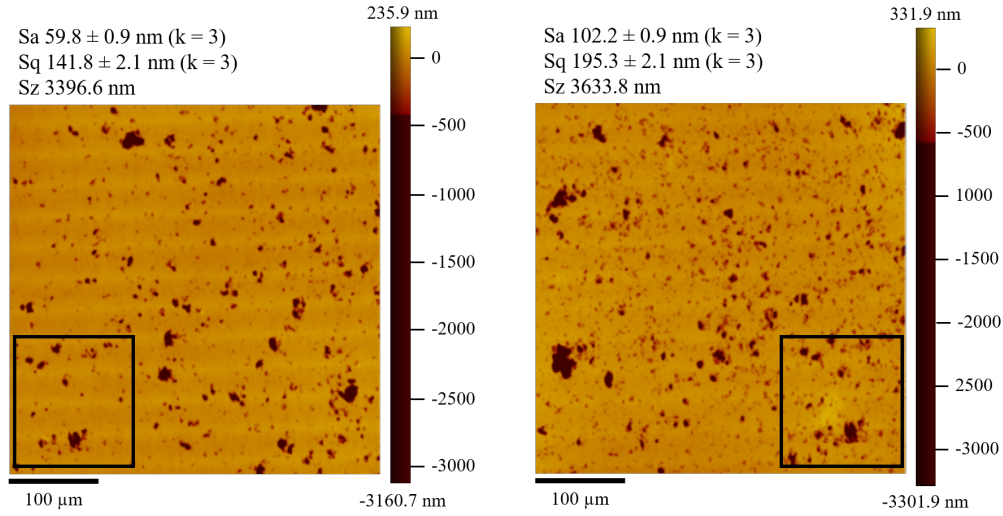
Figure 4.21: (left) SPDT surface; (right) SPDT turned - etched.

Figure 4.22 shows the progression of damage removal in MRF spotting after 21 seconds of spotting time. The diagonal marks in the surfaces are made by the MRF fluid (D10). Larger pits were revealed following the etching process.
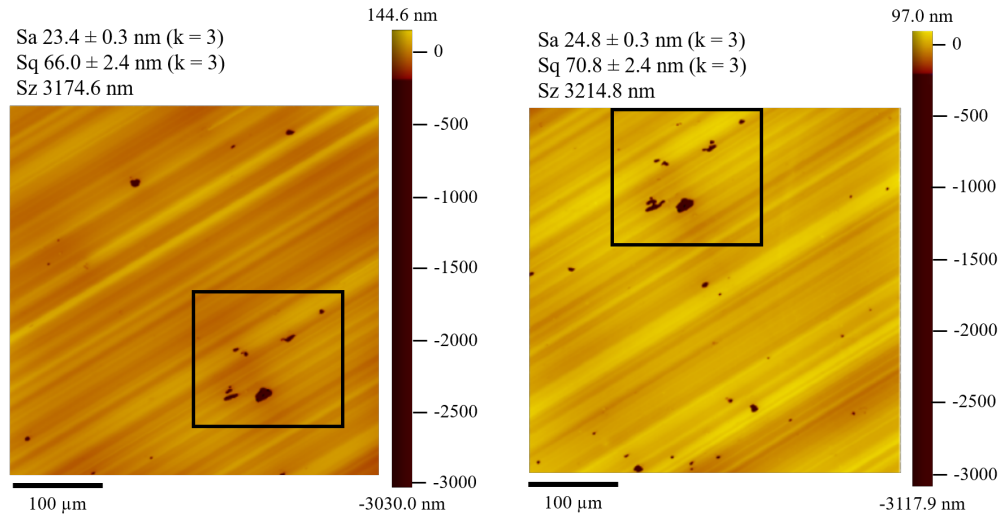
Figure 4.22: (left) MRF spot - 21 seconds; (right) MRF spot - 21 seconds - etched.

Figure 4.23 shows a 60 second spot. No additional damage (in the form of pits) was observed in the pre-etched or etched surface that indicated damage from the diamond turning operation. There was no sign of material shearing from the MRF process; however, more experiments are required.
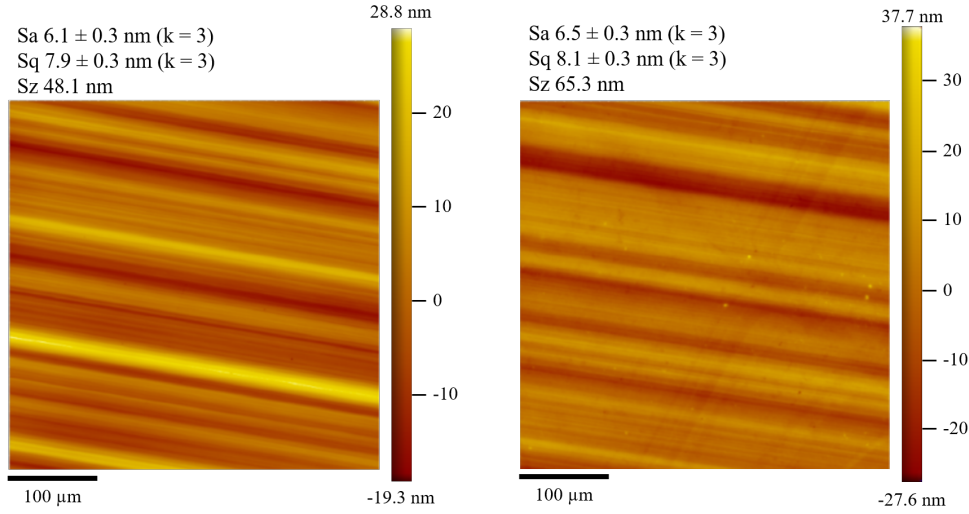
Figure 4.23: (left) MRF spot - 60 seconds; (right) MRF spot - 60 seconds - etched.
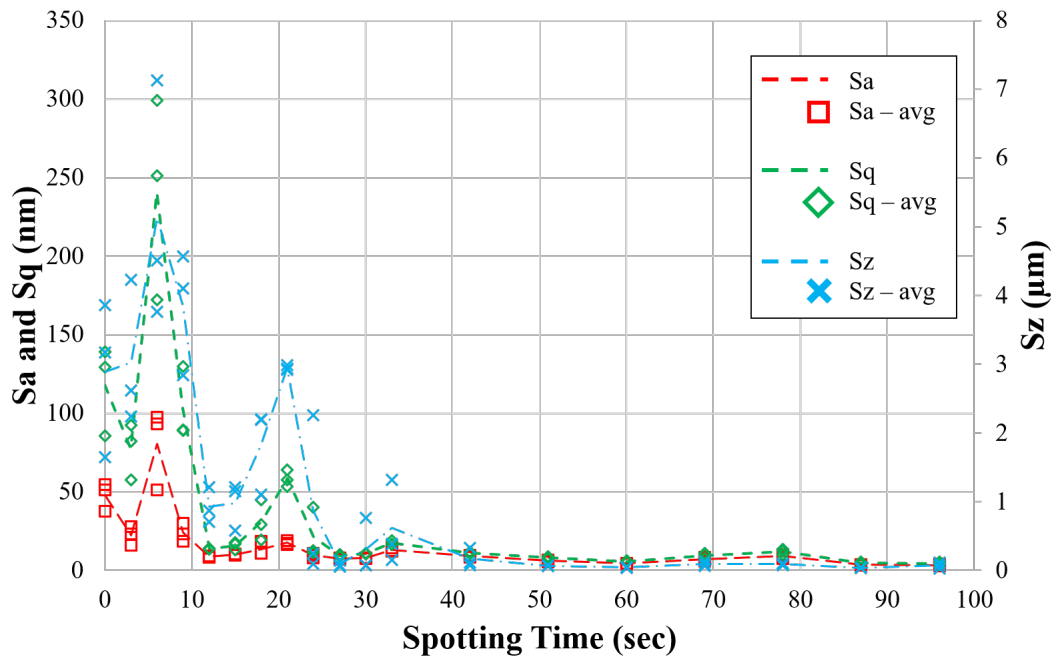
Figure 4.24: Evaluation of surface parameters from spotting data.

An estimation of the subsurface damage was determined from the CSI results. Figure 4.24 shows the plot of Sa, Sq, and Sz. The plot summarizes an average of measurements for each of the spotting times. The spotting surfaces begin to be free of pits between 40-50 seconds spotting time. This concludes that the estimated

subsurface damage was between 5.2 to 6.3 μm deep.

The theoretical spot depth compared relatively close to the measured spot depth. The original material removal rate for D10 fluid was at 8 μm/min; however, the trend depicted in Figure 4.25 matches better with a material removal rate of 7.5 μm/min. This could be from the change in viscosity during the polishing operation.
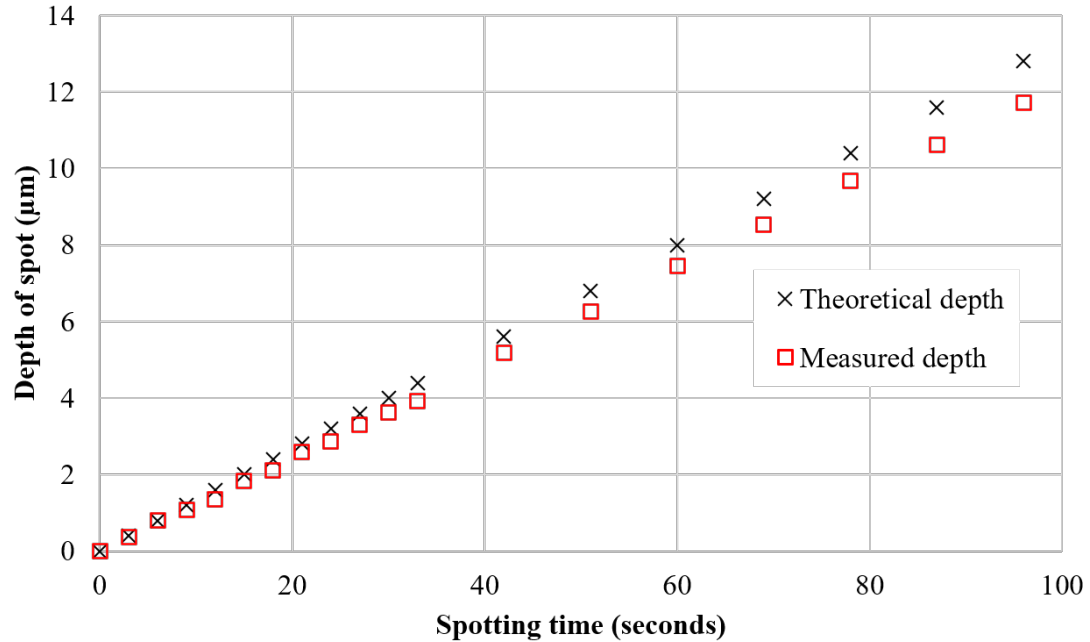
Figure 4.25: Theoretical and measured spot depth from CSI stitch.

4.4.1.2   Sample 2 - Mid-spatial Evaluation

The study involving sample 2 - MRF full aperture polishing - showed great promise in removing damage and mitigating mid-spatial frequencies from a SPDT Ge puck. Figure 4.26 illustrates the transition in MRF polishing for select steps of the process. At 5 μm of material removed, it can be seen that most of the damage from diamond turning has been removed. It was observed in an additional sub-study that D10 fluid can polish Ge to a sub-nanometer surface finish after filtering is applied. However, D10 is not a sufficient finishing slurry. D20 or possibly C30 would be a suitable fluid as the particle sizes for these slurries are much finer. A finer abrasive would be

necessary for improving the surface texture.
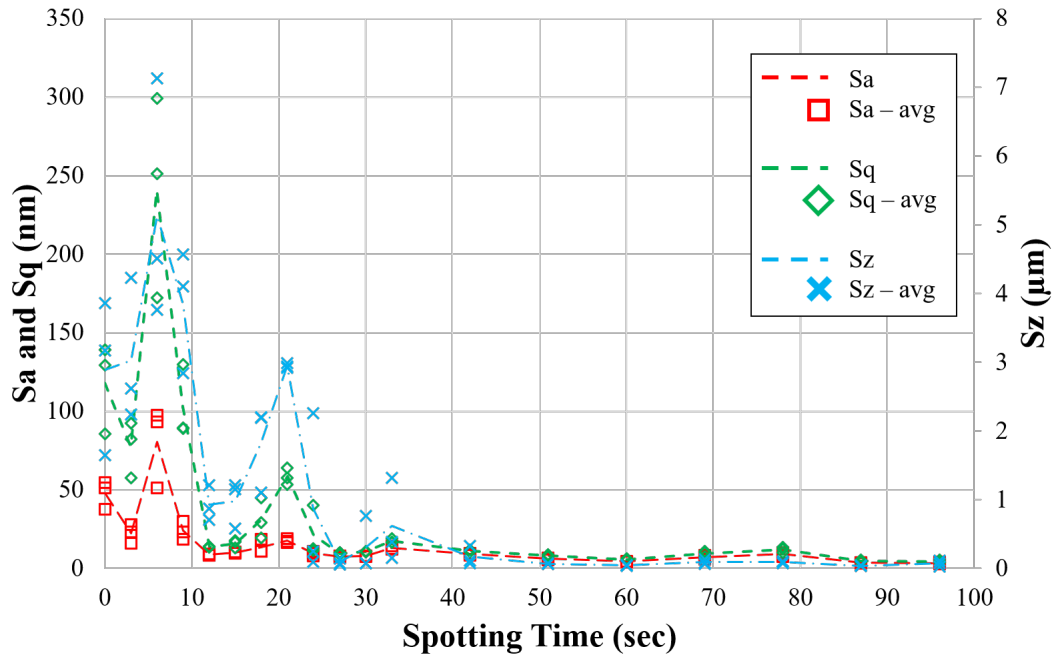
Figure 4.26: (a) SPDT surface; (b) iteration 2 - 1 μm removed; (c) iteration 4 - 2 μm removed; (d) iteration 8 - 5 μm removed.

The information in Figure 4.27 shows that the MRF full aperture polish continuously removed damage from the surface. The drop in Sz indicated that there are fewer pits from fracture present in the surface topography. In comparison to the spotting data, the subsurface damage might be removed within the next micrometer or so, since both sample were generated using the same tool, setup, and cutting parameters.
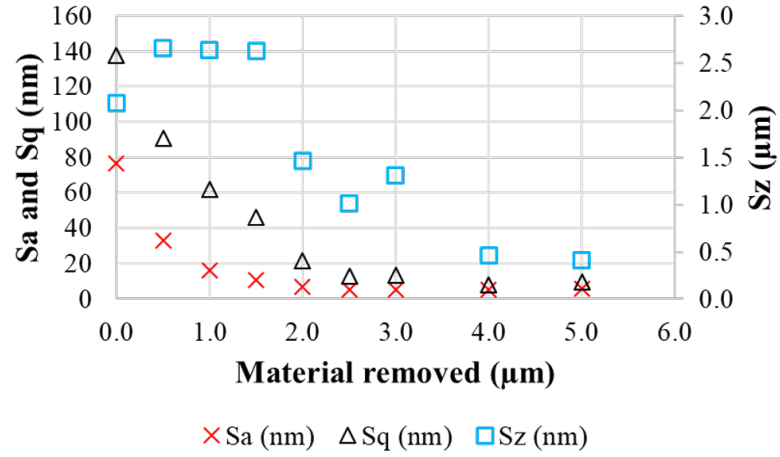
Figure 4.27: Surface history from full aperture polish in steps.

In order to get a better picture of the capabilities of the MRF machine using D10, an evaluation of the surface using a power-spectral density (PSD) plot was necessary. A 2.75x objective with a 1x tube lens was used to measure the surface to obtain a PSD plot. A PSD shows dominating surface characteristics, such as f_r. The f_r and a harmonic of the f_r can be seen in Figure 4.28 as two peaks in iteration 0 (it.0). There was also a mid-spatial indicated by the arrow in Figure 4.28 that shifted and propagated further into the polished surface.
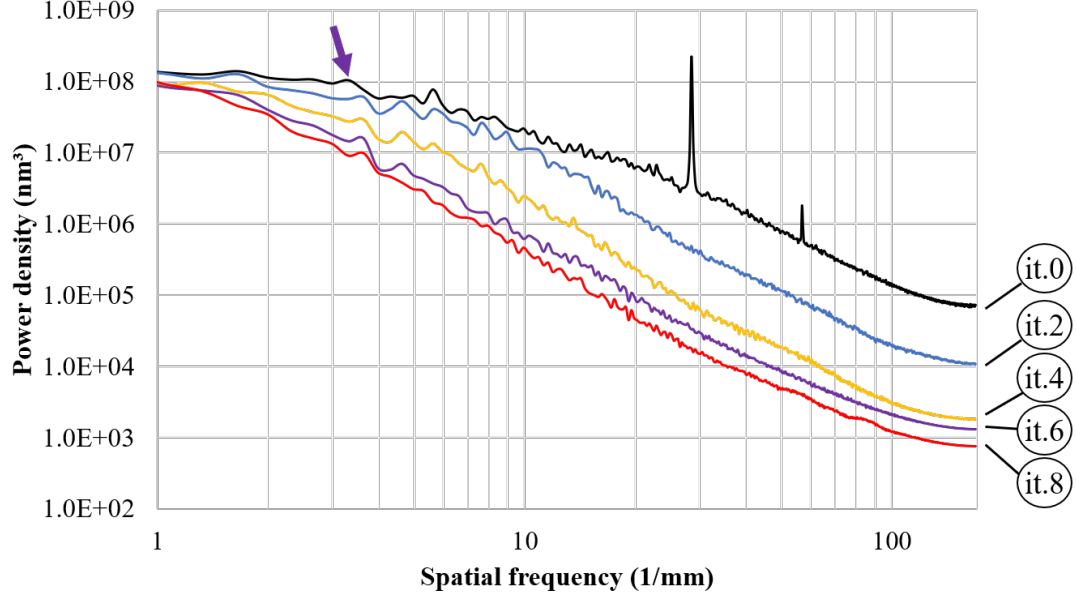
Figure 4.28: PSD plots from the SPDT surface and the MRF polished surfaces.

4.4.2   Surface Integrity Results

The following study focused on creating and characterizing a set of Ge specimens, which had a major crystal orientation of (100), that were created with single point diamond turning using 3 mm R and -25 degree α with a range of f_r values. The a_{doc} and Ω were held constant at 10 μm and 1000 rpm, respectively. These were previously described in Section 2.2.1.4 of Chapter 2. In addition to the as-cut surfaces, surfaces finished with MRF, CMP, and a combination of CMP+etching were investigated. The polish arrangements for CMP and MRF were explained in Section 2.3 of Chapter 2. Note that the polished and etched surfaces were all diamond turned using the same machine input parameters, where f_r was 9 μm/rev. The mini-dynamometer was used to measure the cutting forces F_c and thrust forces F_t during off-axis turning. The resulting surfaces and subsurfaces were characterized with CSI, confocal Raman, and RBS.

Figure 4.29 and 4.30 show the seven surfaces that were examined in this study. The three diamond turned surface shown in Figure 4.29 used considerably higher values f_r

that could be useful during a roughing stage of machining. Severe surface damage can be observed in height map (a) of Figure 4.29. The four surfaces shown in Figure 4.30 had the lowest surface finish values and, as will be discussed later, the best surface integrity.
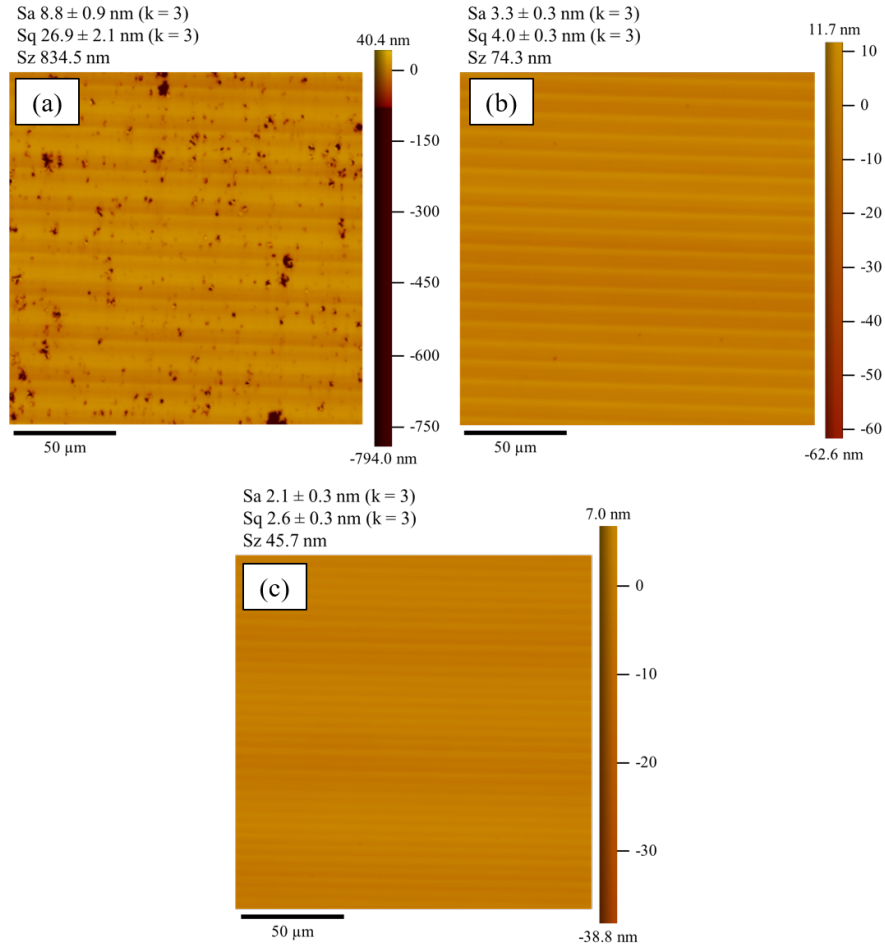
Figure 4.29: Single-point diamond turned with f_r values of (a) 20 μm/rev, (b) 9 μm/rev, and (c) 5 μm/rev.
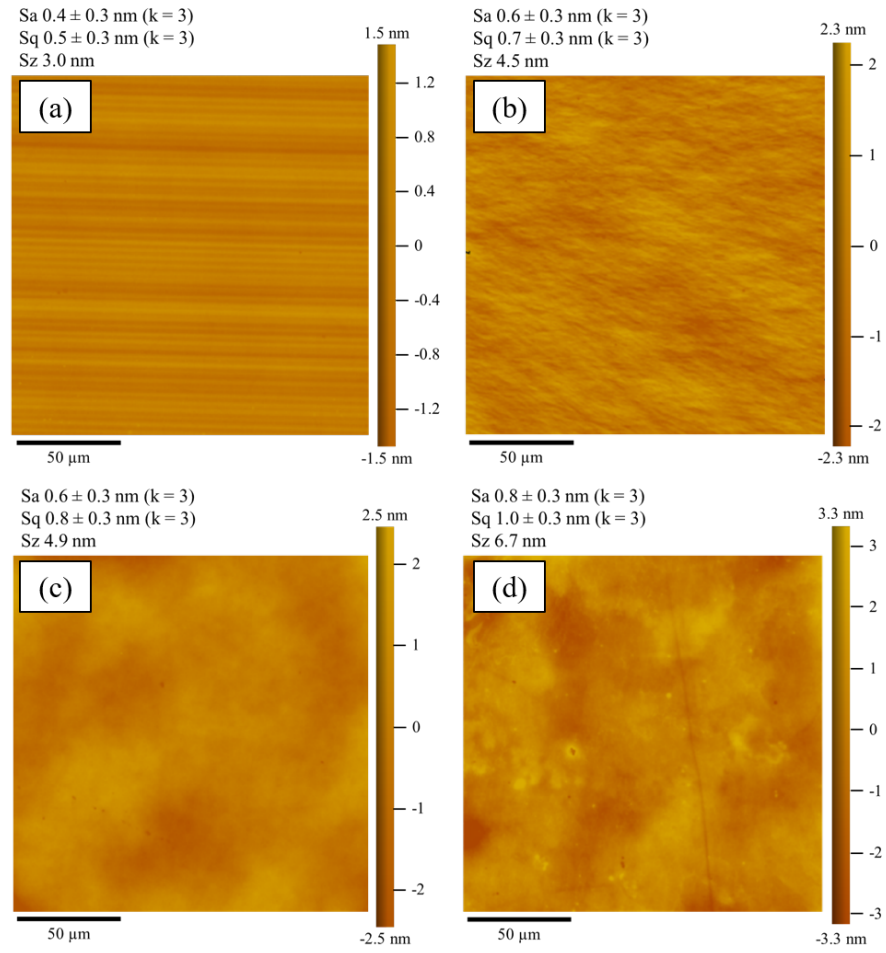
Figure 4.30: Best surfaces by the following processes: (a) SPDT, f_r of 0.3 μm/rev, (b) MRF, (c) CMP, and (d) CMP + Etched with hydrogen peroxide.

An initial study using confocal Raman was completed on the for each of the diamond turned surfaces and polished surfaces prior to examining with RBS. Figure 4.31 shows two plots. The top plot is the peak centering and the bottom plot is the peak width. Peak centering provides information regarding the residual stress within the lattice. An approximation of the residual stress is calculated from the peak centering data. Peak width or broadening of the peak indicates lattice disorder, such as cracks or dislocations. The CMP surface has the least lattice disorder, while the two diamond turned surface with f_r values of 0.5 μm/rev and 1.0 μm/rev have less than the MRF surface.
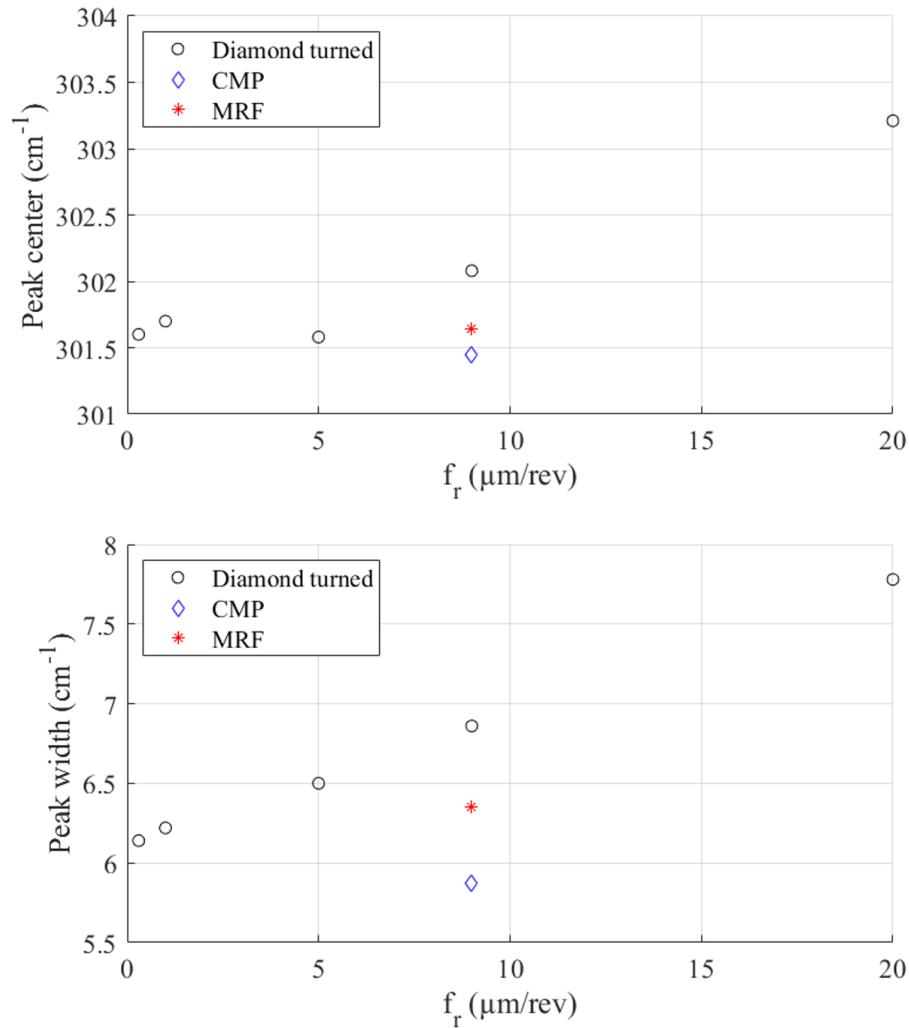
Figure 4.31: Confocal Raman results (top) peak center, (bottom) peak width.

Figure 4.32 shows the residual stress from the surfaces. Again, the CMP surface and the 0.3 μm/rev surfaces exhibited the lowest residual stress.
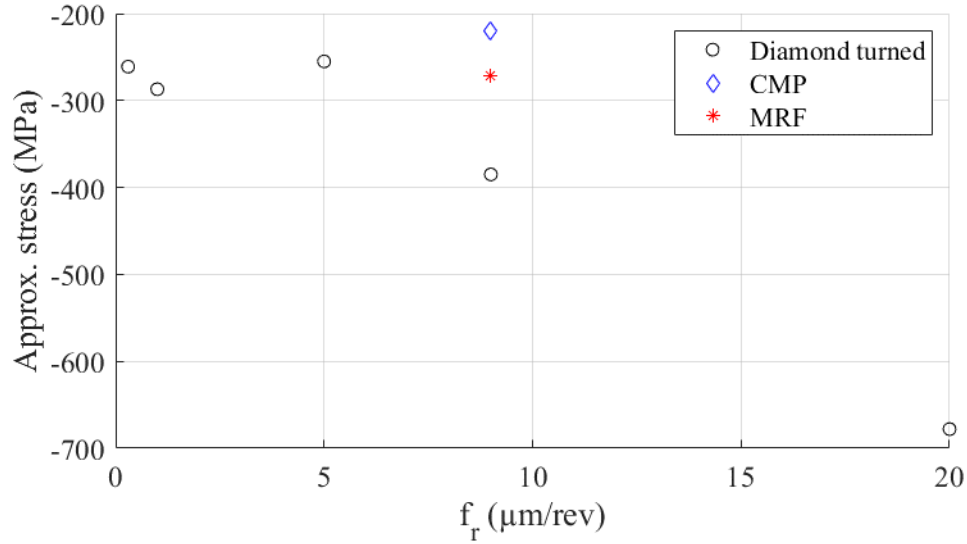
Figure 4.32: Confocal Raman results - residual stress.

Channeling RBS was performed on all of the surfaces to quantitatively measure the near surface crystal quality. MeV ions directed at an aligned crystal backscatter due to direct encounters with atoms on the surface, and also as a result of near surface lattice disorder. In a channeling experiment, the number of backscattered ions as a function of their backscattered energy is collected. If the disordered layer is thin (<1 μm) a surface peak in the backscattered spectrum occurs. It can be shown from first principles that the integrated intensity of the surface peak (the number of backscattered ions normalized by the charge collected and the solid angle of the detector) is directly proportional to the number of displaced atoms at the surface/cm^2 [36]. The values of the channeling minimum yield χ_{min}, which is the ratio of the backscattered yield under channeling conditions to that of a randomly oriented crystal, also provides a measure of the near surface crystal quality.

The resulting RBS spectra are shown in Figure 4.33 and the values of the channeling minimum yield, χ_{min}, are shown in Table 4.4. The as-cut surfaces were generally found to have an increasing amount of near surface damage with increasing feed f_r. The width of the peaks are marginally larger with increased f_r,

The one surface that did not fit this trend was the diamond turned surface with a f_r value of 1 μm/rev. It is unclear why the sample did not fit the trend and was therefore removed from the RBS results. A repeat of the channeling RBS experiments on the specimens created from diamond turning only is underway.
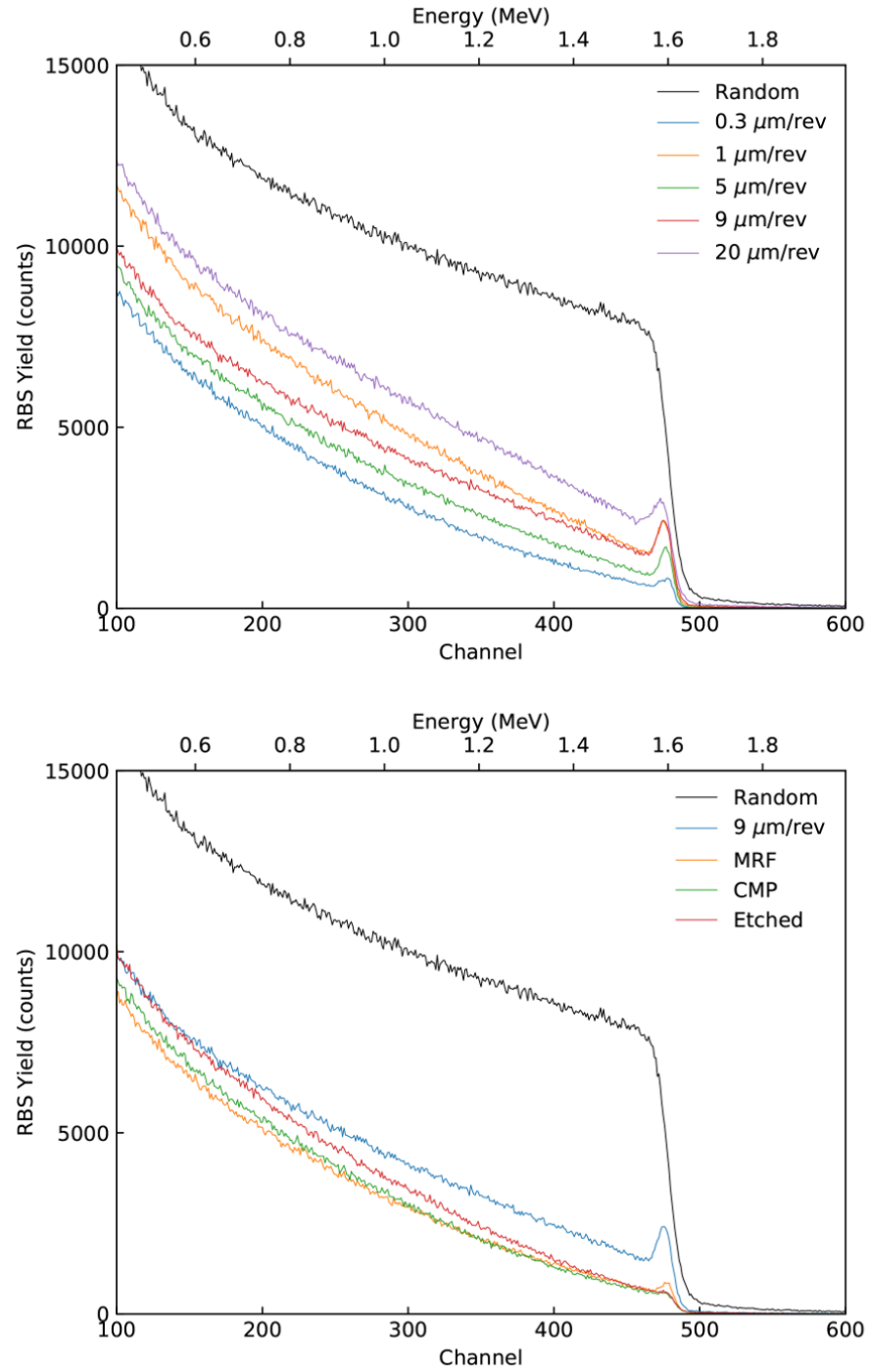
Figure 4.33: Channeling RBS spectra of the Ge surfaces.

Table 4.4: Channeling minimum yield χ_{min} values.

Processing	χ_{min}	d (μm)
DT: 0.3 μm/rev	8.4	0.06
DT: 1 μm/rev	20.2	1.02
DT: 5 μm/rev	12.2	0.47
DT: 9 μm/rev	19.3	.96
DT: 20 μm/rev	30.5	1.44
MRF	8.9	0.12
CMP	8.0	0
CMP+Etch	8.7	0.1

Taking the information from Table 4.4, an estimate of the disorder depth from the surface can be calculated using Eq 4.1. χ_{CMP} here is the CMP surface as it is nearly disorder-free (no peak). These value are also reported in Table 4.4.

$$d = \ln \frac{(1 - \chi_{min})}{(1 - \chi_{CMP})} \qquad (4.1)$$

CHAPTER 5: MODELING RESULTS

The information reported in this section was used from [42] and copyright permission was provided by the publisher. See Appendix A for the supporting documents.

5.1   Predicting Surface Roughness Parameters

For each prediction target outcome, i.e. Sa, Sq, and Sz, the classic machine learning algorithms were tested by building 1000 models per algorithm and per target, i.e. executing 1000 runs of each algorithm for each target. The results were averaged to obtain each evaluation metric. Each model was trained on data obtained by randomly splitting the (cleansed and standardized) dataset in 80% for training and 20% for testing sets. At each run, the same training input data and target output were used to train each of classic machine learning algorithms.

Experiments were also performed for the six different ANN configurations, as described previously described in Chapter 3. In the ANN experiments, the number of epochs was set to 300 with batch size of 1. In neural network terminology, an epoch corresponds to one forward and one backward pass of all the training examples. Batch size is the number of examples in one forward/backward pass. This means that the 648 examples in the Ge training dataset (and similarly, the 62 examples of the Cu training data) are presented as input to the model 300 times during the model training phase. Thus, the ANN will be trained in $(300 * 648 =)$ 194,400 iterations to pass the Ge training set through the algorithm, and $(300 * 62 =)$ 18,600 iterations for the Cu training data. The number of iterations indicates how much more computationally intensive it is to train an ANN with larger datasets. However, larger datasets are far preferred over small datasets.

5.1.1   Copper

Tables 5.1, 5.2, and 5.3 present the average results of 1000 runs for the classic machine learning algorithms for Sa, Sq, and Sz, respectively. Numeric results for both training and testing are provided for each of four metrics. A score of 1 for EVS indicates the model is capable of fully capturing the variance in the data. Thus, the best models based on these criteria are those closer to 1. For metrics measuring the error between prediction and measured values the best-case scenario is a score as close to 0 as possible.

The random forest (RF) with a maximum depth of 8 nodes performed the best when predicting the average surface roughness, Sa. This results and all other traditional machine learning models can be seen in Table 5.1.

Table 5.1: Sa average prediction results of 1000 runs for copper dataset.

ML Algorithms	EVS (test | train)	$RMSE$ (test | train)	MAE (test | train)	$MaxError$ (test | train)
DT(2)	0.987 | 0.977	6.625 | 10.057	2.39 | 8.889	21.248 | 16.379
DT(5)	1 | 0.988	0.585 | 7.382	0.294 | 1.654	1.881 | 10.44
DT(8)	1 | 0.987	0.122 | 7.493	0 | 1.392	0.366 | 10.936
DT(11)	1 | 0.988	0.109 | 7.425	0 | 1.376	0.366 | 10.664
RF(8)	0.998 | 0.996	2.846 | 3.912	0.217 | 1.057	12.946 | 6.282
RF(11)	0.998 | 0.996	2.85 | 3.934	0.235 | 1.084	12.972 | 6.377
AB(8)	1 | 0.989	0.355 | 7.102	0.102 | 1.297	0.648 | 9.399
AB(11)	1 | 0.989	0.338 | 7.104	0.112 | 1.297	0.553 | 9.399
SVR(RBF)	0.973 | 0.947	9.736 | 15.605	0.323 | 2.3	71.666 | 58.788
SVR(Poly)	0.999 | 0.954	1.737 | 14.181	0.222 | 1.196	7.842 | 11.488
SVR(Sig)	0.014 | 0.012	65.991 | 91.652	2.993 | 46.862	217.61 | 198.261
Eq 3.1	— | 0.977	— | 5.410	— | 2.138	— | 17.812

Table 5.2: *Sq* average prediction results of 1000 runs for copper dataset.

ML Algorithms	*EVS* (test | train)	*RMSE* (test | train)	*MAE* (test | train)	*MaxError* (test | train)
DT(2)	0.988 | 0.972	7.675 | 13.128	2.917 | 4.402	19.963 | 21.811
DT(5)	1 | 0.999	0.782 | 2.953	0.47 | 1.424	2.174 | 2.681
DT(8)	1 | 0.999	0.212 | 2.919	0.059 | 1.391	0.616 | 2.681
DT(11)	1 | 0.999	0.166 | 2.928	0 | 1.391	0.542 | 2.681
RF(8)	0.998 | 0.995	3.043 | 5.378	0.29 | 1.756	10.204 | 6.948
RF(11)	0.998 | 0.995	3.039 | 5.388	0.303 | 1.739	10.128 | 6.899
AB(8)	1 | 0.999	0.434 | 2.808	0.109 | 1.391	0.542 | 2.681
AB(11)	1 | 0.999	0.416 | 2.788	0.113 | 1.214	0.542 | 2.681
SVR(RBF)	0.953 | 0.969	15.675 | 14.774	0.411 | 2.339	84.603 | 42.296
SVR(Poly)	0.999 | 0.998	2.389 | 3.495	0.317 | 1.231	6.339 | 3.824
SVR(Sig)	0.012 | 0.011	79.56 | 97.649	4.333 | 31.976	247.982 | 236.66
Eq 3.1	— | 0.998	— | 5.498	— | 2.700	— | 16.446

The adaboost (AB) with a maximum depth of 11 nodes performed the best when predicting the root mean squared average surface roughness, *Sq*. This results and all other traditional machine learning models can be seen in Table 5.2.

Table 5.3: Sz average prediction results of 1000 runs for copper dataset.

ML Algorithms	EVS (test | train)	$RMSE$ (test | train)	MAE (test | train)	$MaxError$ (test | train)
DT(2)	0.982 | 0.991	9.25 | 8.1	3.359 | 2.363	23.944 | 25.792
DT(5)	1 | 0.998	0.785 | 3.975	0.576 | 0.954	2.061 | 5.439
DT(8)	1 | 0.998	0.255 | 3.991	0.012 | 1.499	0.86 | 5.439
DT(11)	1 | 0.998	0.242 | 3.989	0 | 1.411	0.86 | 5.439
RF(8)	0.999 | 0.999	2.463 | 2.937	0.373 | 0.683	9.705 | 8.493
RF(11)	0.999 | 0.999	2.482 | 2.986	0.377 | 0.684	9.766 | 8.621
AB(8)	1 | 0.998	0.42 | 3.986	0.174 | 1.285	0.687 | 5.439
AB(11)	1 | 0.998	0.473 | 4.023	0.109 | 1.615	0.86 | 5.439
SVR(RBF)	0.975 | 0.955	10.961 | 19.457	0.483 | 1.111	79.791 | 72.702
SVR(Poly)	0.999 | 0.99	2.361 | 8.309	0.347 | 0.831	3.422 | 6.58
SVR(Sig)	0.013 | 0.012	78.849 | 97.685	5.354 | 5.107	246.916 | 236.381
Eq 3.1	— | 0.799	— | 265.531	— | 55.438	— | 708.091

The random forest (RF) with a maximum depth of 8 nodes performed the best when predicting the peak-to-valley, Sz. This results and all other traditional machine learning models can be seen in Table 5.3.

Machine learning model performance was measured on how well the model predicted new data, i.e. the test set. The criterion for the best model for predicting each surface roughness target was the lowest RMSE score among test results. A closer inspection of the numeric results (in Tables 5.1, 5.2, and 5.3) shows that the model with the lowest RMSE test results also score as the best or close to the best model in the other three scoring criteria. Random forest, with maximum depth of 8, outperforms all other models when predicting Sa and Sz for the Cu dataset, while adaboost, maximum depth of 11, was the best model for predicting Sq.

Table 5.4 presents the results for the ANN configurations tested. As with the classic machine learning model results, the lowest RMSE score on the Cu test set was the criterion set for selecting the best model here. Even though all models are good predictors of the target Sa, as indicated by their R^2 scores, the 'Deeper' ANN models achieve better fit to the data. For Sa, the 'Deeper' ANN with the larger number of neurons in its three hidden layers, i.e. 50, 25, and 12 neurons, outperforms all the other ANN configurations, as well as the best model selected from the classic machine learning algorithms, i.e. Random forest with max depth of 8. Therefore, among the experiments with the Cu data, the best model for predicting Sa is the 'Deeper' ANN with configuration [50-25-12-1]. All machine learning and ANN models also outperform the analytical model (Eq 3.1) with respect to RMSE.

Table 5.4: Sa prediction results for the Cu dataset using artificial neural networks.

ANN type	ANN config (test | train)	R^2 (test | train)	$RMSE$ (test | train)
Base-line	[5-10-1]	0.992 | 0.991	5.432 | 5.57
Wider	[5-24-1]	0.993 | 0.993	5.329 | 4.661
Deeper	[5-24-16-8-1]	0.996 | 0.996	3.974 | 3.586
Deeper	[5-10-10-10-1]	0.995 | 0.994	4.401 | 4.349
Wider	[5-50-1]	0.995 | 0.994	4.331 | 4.641
Deeper	[5-50-25-12-1]	0.999 | 0.998	1.682 | 2.664
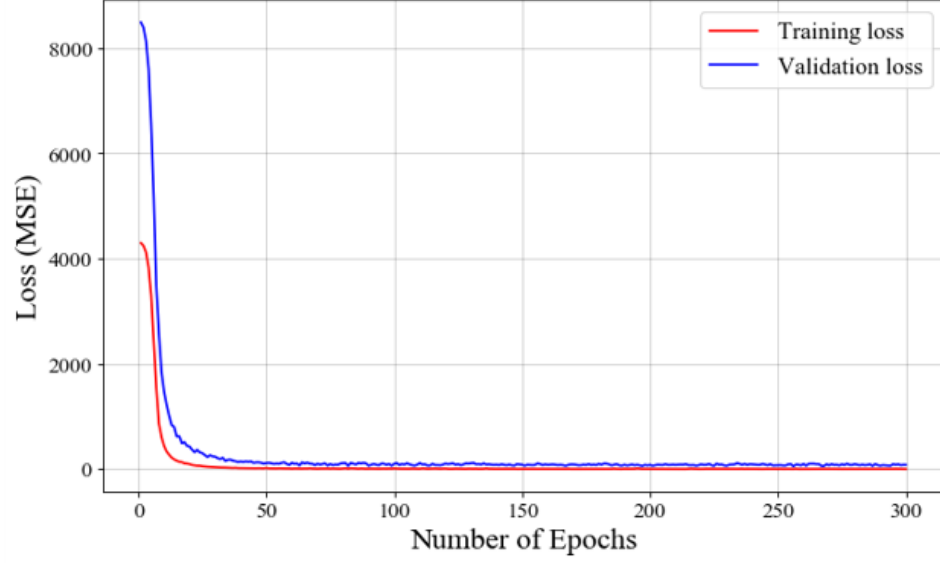
Figure 5.1: Loss (mean squared error) vs epochs for 'Deeper' ANN model ([5-50-25-12-1]) for the Cu dataset.

Figure 5.1 shows that the losses, based on MSE for the 'Deeper' ANN, gradually decrease to a steady state within 50 epochs. The two plots in Figure 5.2 allow for a direct comparison between the absolute error for Sa values predicted by the best 'Deeper' ANN versus the absolute error for analytical Sa values (Eq 3.1) as a function of f_r, and shows that the ANN model has a lower absolute error.
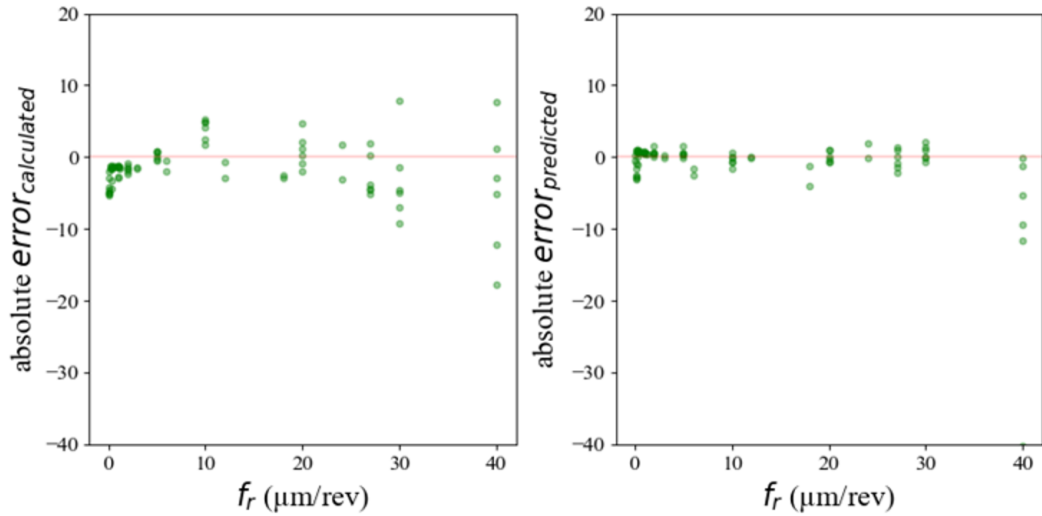
Figure 5.2: Plot of absolute error for analytical Sa and predicted Sa versus the observed Sa by the 'Deeper' ANN model ([5-50-25-12-1]) for the Cu dataset.

The Q-Q (quantile-quantile) plot in Figure 5.3 confirms the close similarity between the observed Sa and predicted Sa distributions. A graphic visualization of how closely the 'Deeper' ANN model predicts Sa when compared to the analytical model (Eq 3.1) is presented in Figure 5.4. The graph insert provides a close-up view of the Sa prediction error for very low values of f_r.
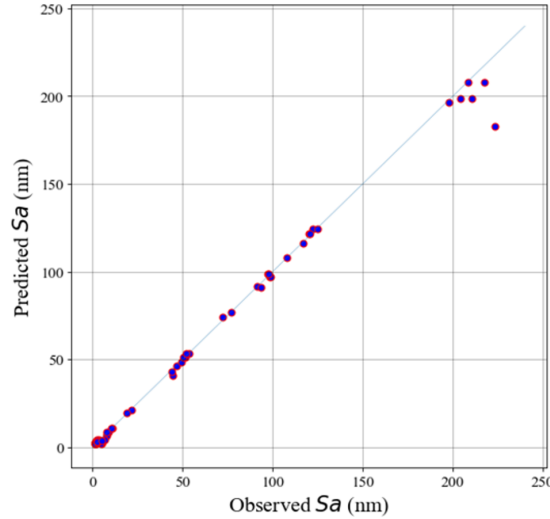
Figure 5.3: Q-Q plot between observed Sa and predicted Sa by the best 'Deeper' ANN model ([5-50-25-12-1]) for the Cu dataset.
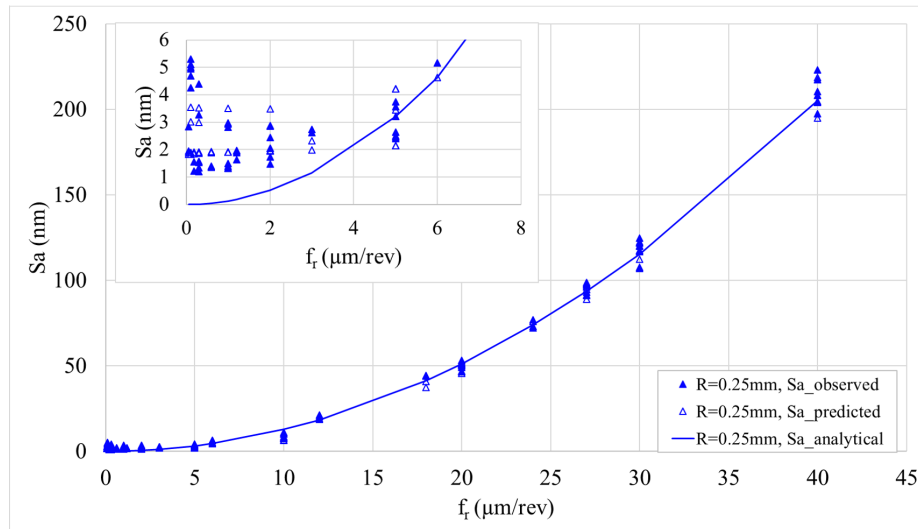
Figure 5.4: Plot of observed Sa and predicted Sa values obtained with best performing 'Deeper' ANN model ([5-50-25-12-1]) versus the analytical Sa for the Cu dataset.

5.1.2   Germanium

Tables 5.5, 5.6, and 5.7 contain the average results for 1000 runs of the classic machine learning algorithm experiments for predicting Sa, Sq, and Sz, respectively, for Ge. The evaluation metrics are the same as those for the Cu models, and the selection of best model for Ge is, again, based on the lowest RMSE score. A strong indication of the power of the machine learning technology is to verify that the same machine learning algorithms selected as the best model for the three surface roughness targets for Cu repeat their performance with the Ge dataset. Random forest with max depth of 8 has the lowest RMSE for Sa and Sz, and adaboost with max depth of 11 was the best model for Sq for Ge data. While the RMSE scores for Sa and Sq for both Cu and Ge are in acceptable ranges and similarly scaled, there was a large discrepancy between the RMSE scores for Sz of the two materials with the scores for Ge being much higher than those of Cu that were away from the acceptable range. The root cause for such large discrepancy is unknown. More research and measurement fieldwork are required to investigate whether the Sz values collected for the Ge dataset are skewed by measurement or other errors. Alternatively, the large deviation in the Sz performance in Ge could be attributed to the inhomogeneous surface fracture of Ge during SPDT. As such, surface fracture is characterized by spatial randomness that is not observed by the models since no image data is involved in the training currently.

Table 5.5: *Sa* average prediction results of 1000 runs for germanium dataset.

ML Algorithms	*EVS* (test | train)	*RMSE* (test | train)	*MAE* (test | train)	*MaxError* (test | train)
DT(2)	0.375 | 0.399	2.954 | 3.389	0.611 | 0.85	30.535 | 19.294
DT(5)	0.85 | 0.66	1.446 | 2.565	0.212 | 0.317	15.588 | 19.149
DT(8)	0.973 | 0.866	0.62 | 1.607	0.081 | 0.25	5.626 | 8.025
DT(11)	0.999 | 0.887	0.111 | 1.474	0 | 0.223	1.125 | 5.936
RF(8)	0.971 | 0.893	0.634 | 1.428	0.086 | 0.218	7.757 | 9.889
RF(11)	0.963 | 0.88	0.716 | 1.518	0.139 | 0.244	7.788 | 10.155
AB(8)	0.997 | 0.811	0.236 | 1.89	0.151 | 0.285	0.957 | 5.245
AB(11)	0.999 | 0.8	0.147 | 1.942	0.045 | 0.227	0.715 | 5.245
SVR(RBF)	0.883 | 0.869	1.286 | 1.612	0.1 | 0.203	22.736 | 13.669
SVR(Poly)	0.846 | 0.801	1.471 | 1.977	0.258 | 0.379	23.347 | 12.811
SVR(Sig)	0.209 | 0.167	3.509 | 4.328	0.2 | 0.279	31.49 | 20.308
Eq 3.1	— | 0.136	— | 4.118	— | 0.701	— | 20.409

Table 5.6: Sq average prediction results of 1000 runs for germanium dataset.

ML Algorithms	EVS (test | train)	$RMSE$ (test | train)	MAE (test | train)	$MaxError$ (test | train)
DT(2)	0.407 | 0.329	5.842 | 8.044	1.25 | 0.89	46.222 | 60.29
DT(5)	0.812 | 0.615	3.292 | 6.119	0.388 | 0.53	37.577 | 51.645
DT(8)	0.971 | 0.826	1.296 | 4.138	0.136 | 0.377	9.573 | 20.304
DT(11)	0.999 | 0.85	0.287 | 3.829	0 | 0.303	2.612 | 18.716
RF(8)	0.978 | 0.827	1.125 | 4.104	0.156 | 0.376	10.14 | 31.092
RF(11)	0.968 | 0.814	1.36 | 4.255	0.236 | 0.395	10.628 | 31.217
AB(8)	0.996 | 0.846	0.517 | 3.846	0.314 | 0.522	1.681 | 29.463
AB(11)	0.999 | 0.879	0.233 | 3.426	0.06 | 0.4	1.461 | 24.855
SVR(RBF)	0.891 | 0.784	2.513 | 4.623	0.148 | 0.277	31.494 | 42.196
SVR(Poly)	0.87 | 0.778	2.738 | 4.649	0.379 | 0.541	29.317 | 42.393
SVR(Sig)	0.162 | 0.097	7.634 | 10.06	0.358 | 0.409	50.166 | 64.134
Eq 3.1	— | 0.077	— | 9.562	— | 1.052	— | 50.319

The adaboost (AB) with a maximum depth of 11 nodes performed the best when predicting the root mean squared average surface roughness, Sq. This results and all other traditional machine learning models can be seen in Table 5.2.

Table 5.7: Sz average prediction results of 1000 runs for germanium dataset.

ML Algorithms	EVS (test | train)	$RMSE$ (test | train)	MAE (test | train)	$MaxError$ (test | train)
DT(2)	0.469 | 0.44	182.864 | 171.016	79.054 | 88.804	865.5 | 671.3
DT(5)	0.799 | 0.587	112.384 | 146.739	22.16 | 37.598	723.5 | 558.6
DT(8)	0.955 | 0.662	52.981 | 133.678	5.84 | 20.193	466.1 | 610.0
DT(11)	0.996 | 0.512	15.892 | 160.923	0 | 19.902	95.6 | 607.5
RF(8)	0.978 | 0.835	37.223 | 93.083	9.188 | 21.726	306.4 | 495.4
RF(11)	0.962 | 0.83	48.868 | 94.4	11.981 | 20.887	418.5 | 491.8
AB(8)	0.993 | 0.81	20.716 | 99.38	4.94 | 15.58	85.3 | 596.3
AB(11)	0.999 | 0.76	8.135 | 111.574	0.033 | 16.497	55.0 | 606.0
SVR(RBF)	0.807 | 0.776	111.039 | 107.5	28.298 | 40.603	772.9 | 552.5
SVR(Poly)	0.85 | 0.813	97.379 | 98.039	28.239 | 38.879	860.2 | 620.3
SVR(Sig)	0.009 | 0.01	297.648 | 267.548	17.678 | 17.843	1262.7 | 935.8
Eq 3.1	— | 0.009	— | 331.984	— | 28.916	— | 1284.2

Table 5.8: Sa prediction results for the Ge dataset using artificial neural networks.

ANN type	ANN config (test | train)	R^2 (test | train)	$RMSE$ (test | train)
Base-line	[5-10-1]	0.896 | 0.872	1.256 | 1.352
Wider	[5-24-1]	0.939 | 0.892	0.959 | 1.24
Deeper	[5-24-16-8-1]	0.995 | 0.973	0.265 | 0.625
Deeper	[5-10-10-10-1]	0.99 | 0.958	0.394 | 0.776
Wider	[5-50-1]	0.941 | 0.915	0.946 | 1.101
Deeper	[5-50-25-12-1]	0.996 | 0.981	0.254 | 0.525

Results for all ANN model configurations tested with the Ge data are shown in

Table 5.8. Similar to the results obtained for Cu, the best model among all ANNs tested was the 'Deeper' ANN with configuration [50-25-12-1]. Still more encouraging, was the fact that this ANN configuration has a much lower RMSE test score than that of the best traditional model found for the Ge data with the Random Forest with max depth 8. Thus, the 'Deeper' ANN with configuration [50-25-12-1] is the overall best model for predicting Sa for both Ge and Cu.

Figure 5.5 shows that the losses, based on MSE for the 'Deeper' ANN, gradually decreased to a steady state within 100 epochs. The Q-Q plot of Figure5.6 shows the correlation between the observed Sa and ANN predicted Sa values, while suggesting a few possible outliers, that require further investigation. Figure 5.7 presents strong evidence of the performance superiority of the 'Deeper' ANN model in predicting Sa for the Ge dataset over the geometric analytical model as the absolute errors of the predictions are significantly lower than the absolute errors of analytical Sa by Eq 3.1.
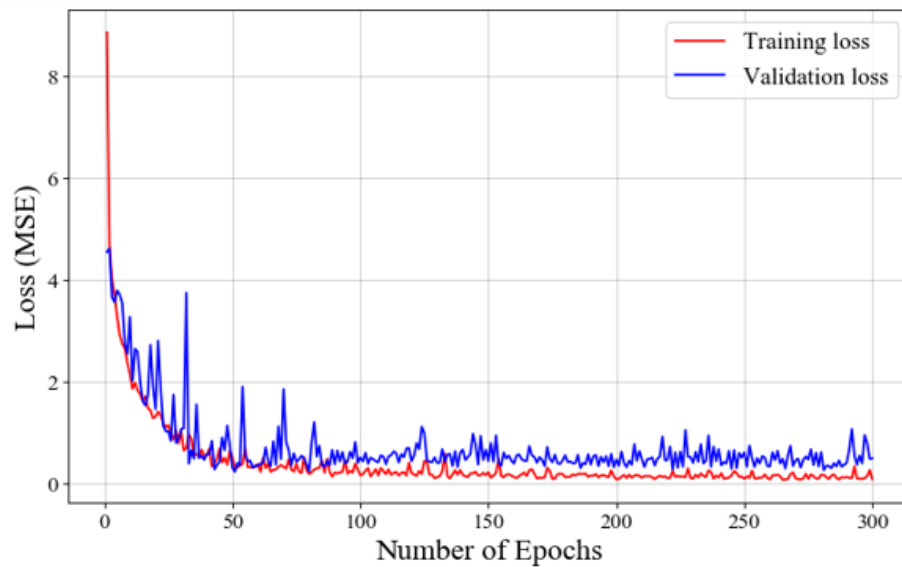
Figure 5.5: Loss (mean squared error) vs epochs for 'Deeper' ANN model ([5-50-25-12-1]) for the Ge dataset.
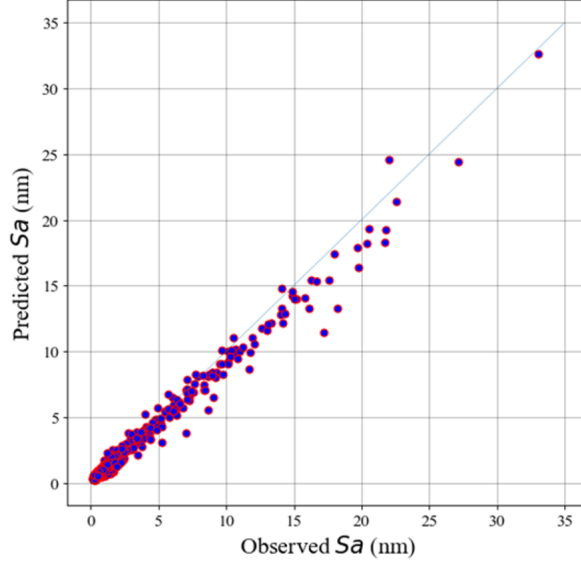
Figure 5.6: Q-Q plot between observed Sa and predicted Sa by the best 'Deeper' ANN model ([5-50-25-12-1]) for the Ge dataset.
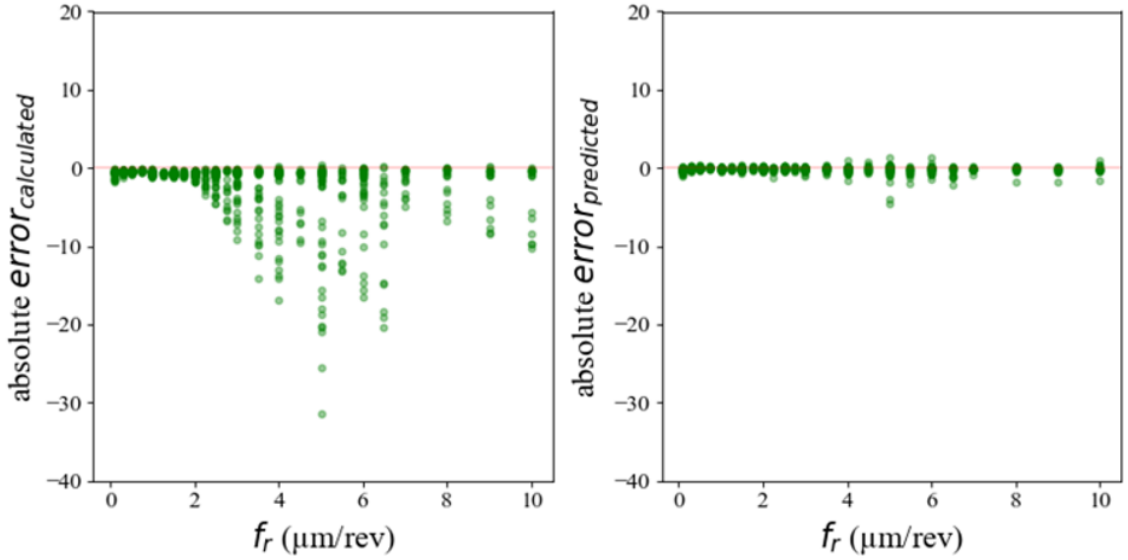
Figure 5.7: Plot of absolute error between analytical Sa and predicted Sa by the best 'Deeper' ANN model ([5-50-25-12-1]) for the Ge dataset.

The superior performance of the 'Deeper' ANN model in predicting target parameter Sa (non-solid markers) over the analytical model (continuous curve) when compared with observed values (solid markers) is shown in Figure 5.8. The ANN model significantly under performs at higher values of f_r. Results are shown for three

values of $R = 0.5$, 1.0 and 5.0. The analytical model also significantly under performs the 'Deeper' ANN model for smaller values of R confirming that surface roughness was dominated by geometric replication of the tool into the surface, especially at lower values of R, which the analytical model was not able to capture. Figure 5.9, 5.10, and 5.11 provide a comparison of the observed, predicted and analytical Sa values for the three cases of tool geometry (R equal to 0.1, 1.0 and 5.0 mm) over a range of f_r. While the 'Deeper' ANN model used to predict the Sa output included all eight of the aforementioned input parameters, Figure 5.9, 5.10, and 5.11 display predictive errors as a function of f_r only. These figures provide graphical insights into the quality of surface finish based on tool geometry and feed. Over the experimental range of f_r, Figure 5.9, 5.10, and 5.11 display which observed values are associated with surface fracture. As can be seen, surface fracture was observed much sooner in feed when the tool nose radius is small. Experiments with tool nose radius $R = 0.5$ mm experienced surface fracture during turning at feeds f_r as low as 1.5 μm/rev, while no fracture was observed at the larger tool nose radius $R = 5.0$ mm, $\alpha = $ -25 deg, $V_c = 2$ m/sec, and $a_{doc} = 25$ μm. In addition, the introduction of surface fracture is associated with increased error between the observed Sa and the analytical model, Eq 3.1.
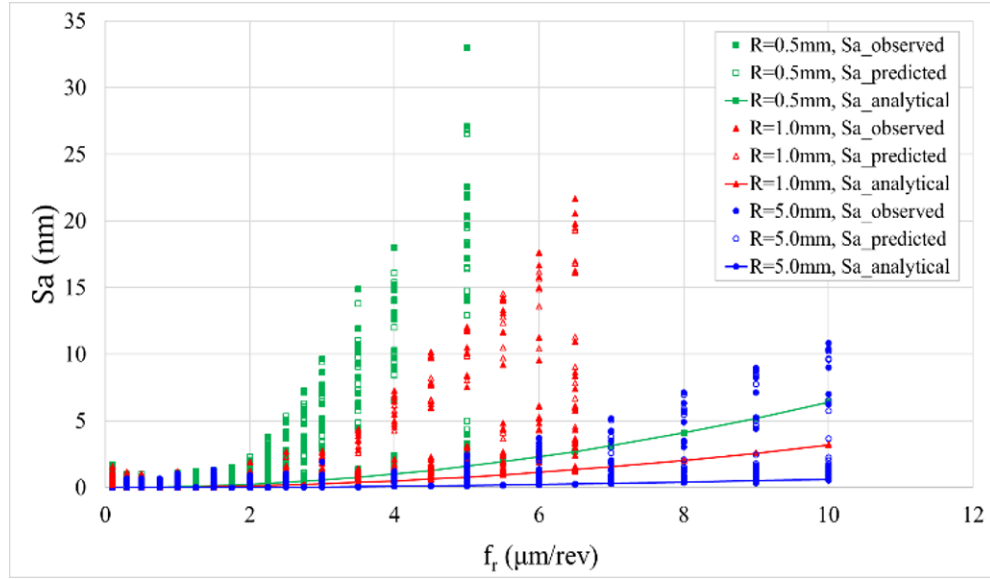
Figure 5.8: Plot of observed Sa and predicted Sa values obtained with best performing 'Deeper' ANN model ([5-50-25-12-1]) versus analytical Sa for the Ge dataset.
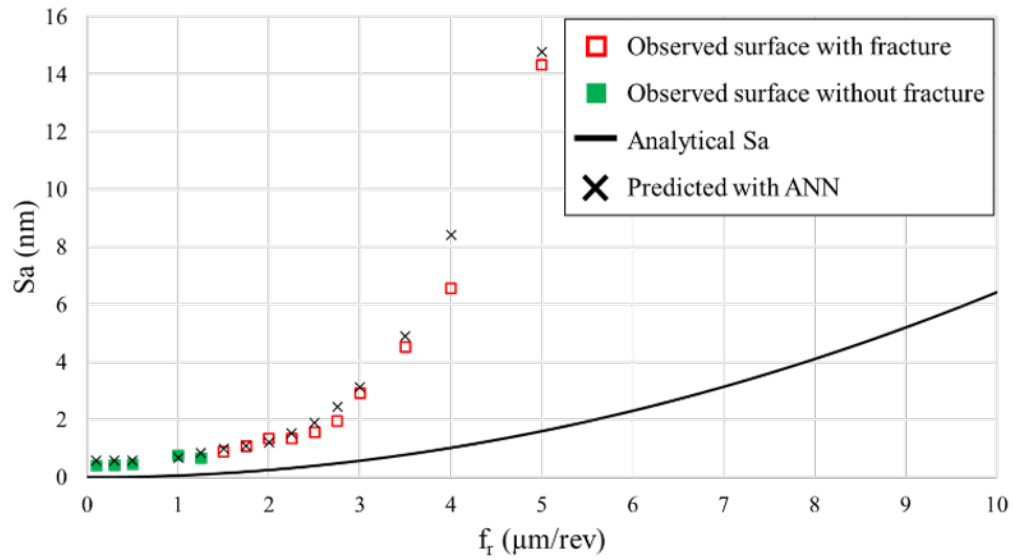
Figure 5.9: Sa roughness for: $R = 0.5$ mm; $\alpha = $ -25 deg; $V_c = 2$ m/sec; $a_{doc} = 25$ μm.
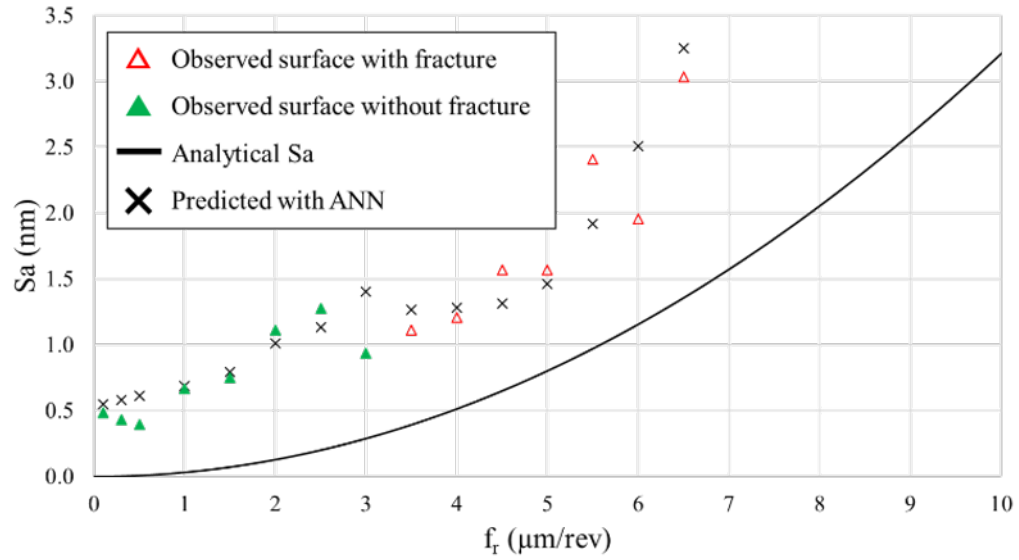
Figure 5.10: Sa roughness for: $R = 1.0$ mm; $\alpha = $ -25 deg; $V_c = 2$ m/sec; $a_{doc} = 25$ μm.
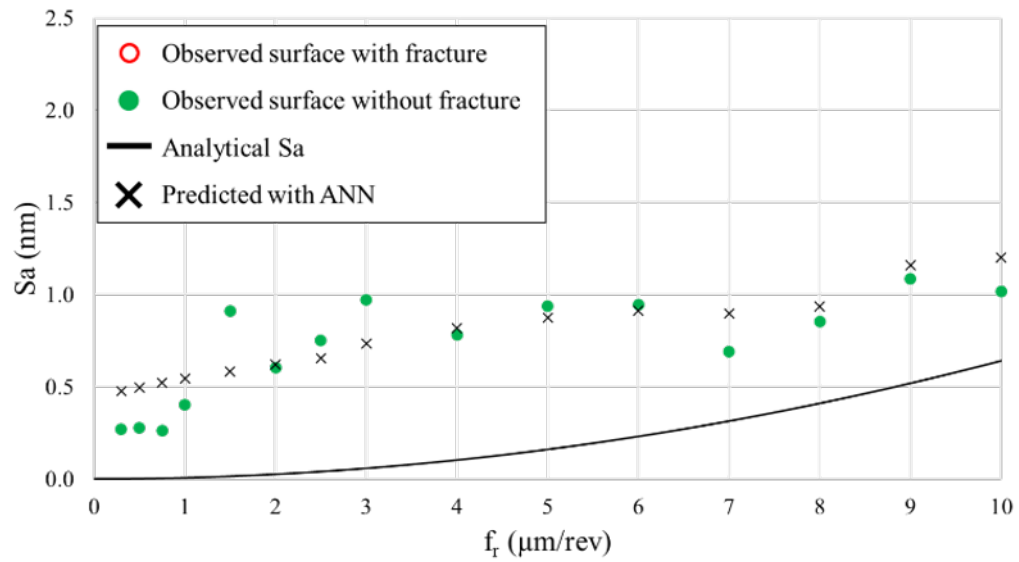
Figure 5.11: Sa roughness for: $R = 5.0$ mm; $\alpha = $ -25 deg; $V_c = 2$ m/sec; $a_{doc} = 25$ μm.

CHAPTER 6: APPLICATION FOR INFRARED OPTICS

The scope of this military application was to conduct research and development in flycutting Ge with the end goal of manufacturing enhanced FACs and SACs lens pairs for quantum cascade lasers. The optics will be manufactured in Ge using three-axis ultra-precision diamond flycutting. The main capabilities that pertain to this project are expertise in multi-axis machining of Ge in the so-called ductile-dominated mode for optical applications and metrology.

Because Ge is a brittle material, machining parameters must be chosen judiciously to obtain a final surface free of fracture. In particular, parameters such as α and R have a significant impact Ge due to its brittle nature. Publications and previous work have shown that a negative α produces a hydrostatic pressure locally in the material. This suppresses brittle fracture and increases plastic deformation in material removal. In addition, R influences the shape of the undeformed chip and how residual fracture is left in the generated surface. Increasing the tool nose radius effectively increases the distance of fracture from the generated surface. This also depends on other input machining parameters like feed f_r and depth of cut a_{doc}, where typically Ge behaves agnostically to a_{doc}.

Sa for flycutting can be predicted based on geometric replication of R onto the surface. This geometric relationship is defined by the equation $Sa = \frac{S_o}{9\sqrt{12R}}$, where S_o is the stepover in μm and R is the nose radius of the tool in μm. Figure 6.1 provides an example of this geometric relationship for flycutting.
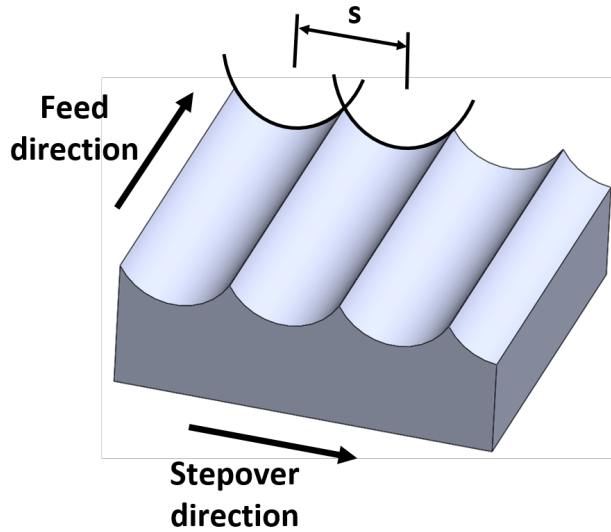
Figure 6.1: Cusp structure from flycutting - when f_r is much lower than S_o.

NanoCAM 4.0 was used to generate the tool paths for the test cylinders and for cutting the two optical elements.

6.1   Fast-axis Lens

The FACs included an acylinder as the major form of the prescription that had an axis of symmetry along the length of the optic making diamond flycutting a viable manufacturing option. Figure 6.2 shows the lens model. A 250 μm R with a -25 degree α diamond insert was used on the flycutter arbor. The following sections will discuss an assessment of the optical design, tool path generation, and a reporting of the metrology completed on the FACs.

Figure 6.2: Fast-axis lens model.

6.1.1   Analysis of Drawings for Manufacturing

Assessment of the initial optical design for the FACs indicated that the blend radius at the transition between the optical surface and the top (alignment) surface required a tool sweep angle of greater than 120 degrees. Diamond tool manufacturers are capable of creating sweep angles up to 180 degrees; however, controlling the waviness of the cutting cannot exceed 120 degrees, which limits the steepness of the blend radius. Refer to Figure C.1 in Appendix B for an example of a sweep angle on a diamond cutter. Since the blend radius was outside of the clear aperture (i.e. not part of the optical surface prescription), RPO modified the blend radius as shown in Figure 6.3(Rev 3). Figure 6.3(Rev 3) shows the profile of the blend radius before and after the change. The change admitted a tool with larger nose radius (250 μm). From a purely geometric standpoint, the larger radius also allows more aggressive (productive) cutting parameters while maintaining a target surface roughness.
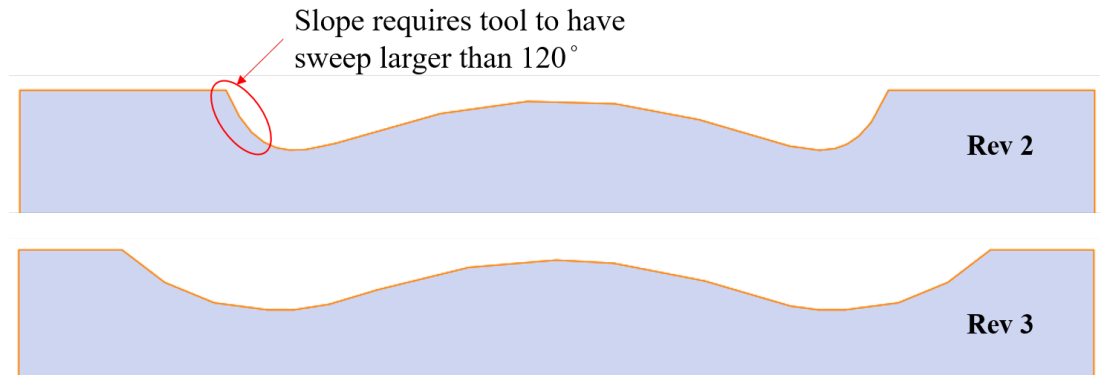
Figure 6.3: In Revision 2, the surface slope in the blend region between the optical surface and the flat reference surface radius that is too large for practical tooling; Revision 3 reduced the slope allowing a larger tool nose radius and a smaller included angle.

6.1.2   Tool Path Generation

NanoCAM 4.0 was used to model the FACs and generate the cutting path. The following subsection discusses the correction of R to ensure that the form of the prescription is manufactured within specification.

6.1.2.1   Tool Nose Radius Correction

A test cylinder was modeled and the subsequent tool path generated in NanoCAM 4.0. A radius r close the base radius of the FACs was defined as 1.5 mm. approximately 18 degrees of the diamond tool sweep is utilized in the manufacturing of the FACs, thus the test cylinder was modeled with a ϕ of 20 degrees. Figure 6.4 shows the model of the test cylinder.
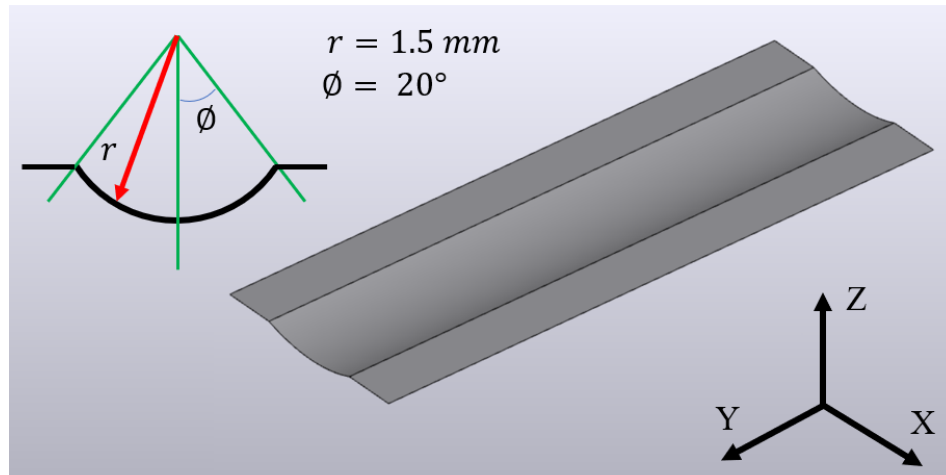
Figure 6.4: Fast-axis test cylinder.
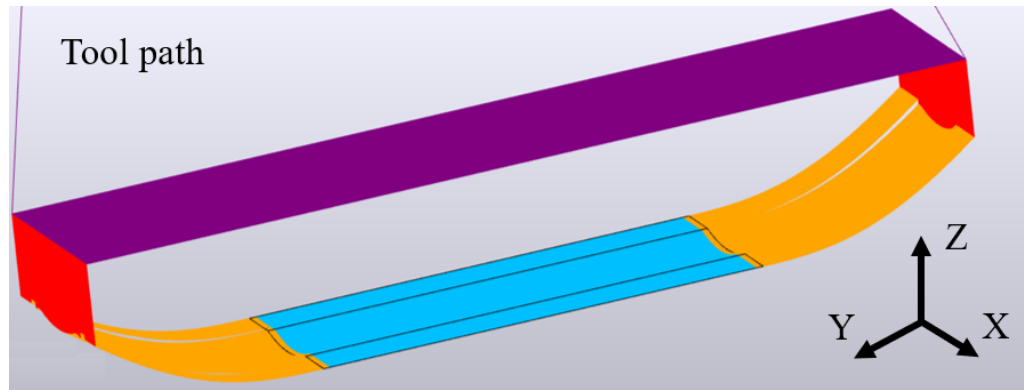
Figure 6.5: Fast-axis test cylinder - tool path.

The tool path for the test cylinder can be seen in Figure 6.5. The tool path included a uni-directional raster.

Nominally the diamond insert had a 250 μm R included a negative α. However, in reality the radius is smaller. This is in part due to the manufacturing method of the diamond insert and the tool height relative to the center of rotation of the flycutting arbor. The latter is perceived as a reduction in R as the tool and an example is shown in Figure 6.6.
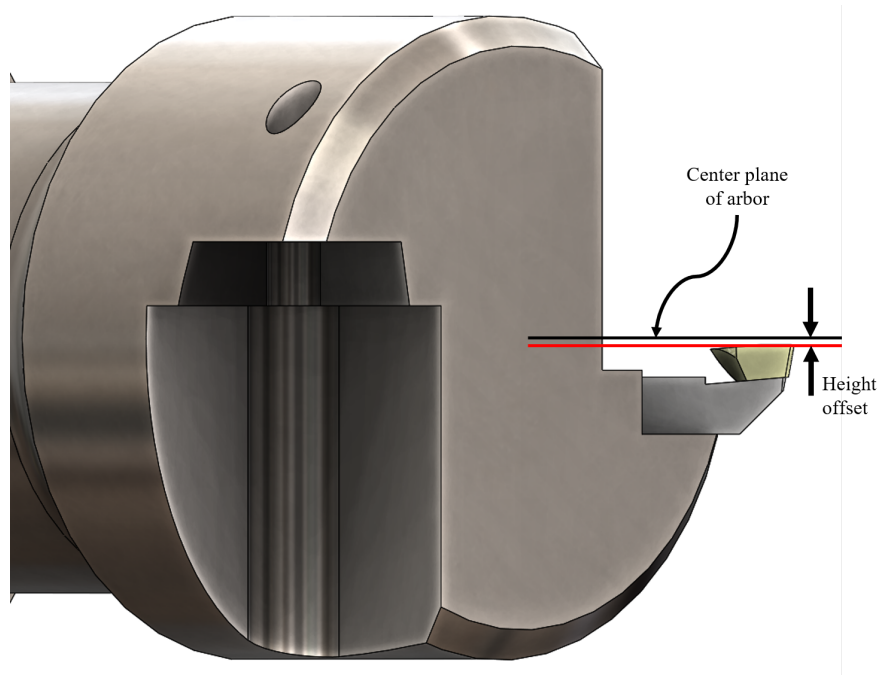
Figure 6.6: Tool height offset example.

Two iterations were completed to determine the actual radius of the tool. The first iteration provided the correction necessary to produce the prescribed radius of the test cylinder. The second confirmed the correction of the radius and provided feedback to any further deviation. Verification of the cylinder radius was confirmed using a Mahr Marsurf LD-260. Traces were taken perpendicular to the axis of symmetry and a best fit radius was calculated from the data using MATLAB®. The corrected R for this setup and tool was 229 μm.

6.1.2.2   Tool Path for FACs

6.1.3   Metrology Verification Results

A Mahr Marsurf LD-260 was used to confirm the form of the fast-axis lens. Figure 6.7 below shows the form error for two traces perpendicular to the acylinder axis. The mean Z error for Figure 6.7 (left) and (right) are 2.8 nm and 7.5 nm, respectively. The standard deviation errors for Figure 6.7 (left) and (right) are 110.1 nm and 108.9 nm, respectively. The peak-to-valley (PV) of the form error is 450 nm.
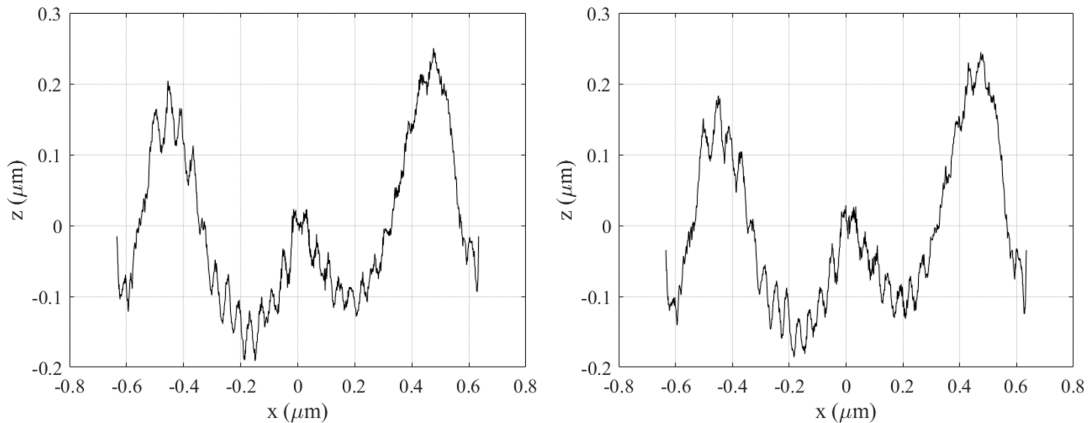
Figure 6.7: Form error from profilometer measurement.

Figure 6.8 shows the mean Sq of the fast-axis lens is 14.7 ±0.3 nm. There is a waviness feature on the surface that has a period of 41 μm and a PV of approximately 60 nm.

Sa 12.3 ± 0.3 nm (k = 3)   33.4 nm
Sq 14.3 ± 0.3 nm (k = 3)
Sz 64.8 nm
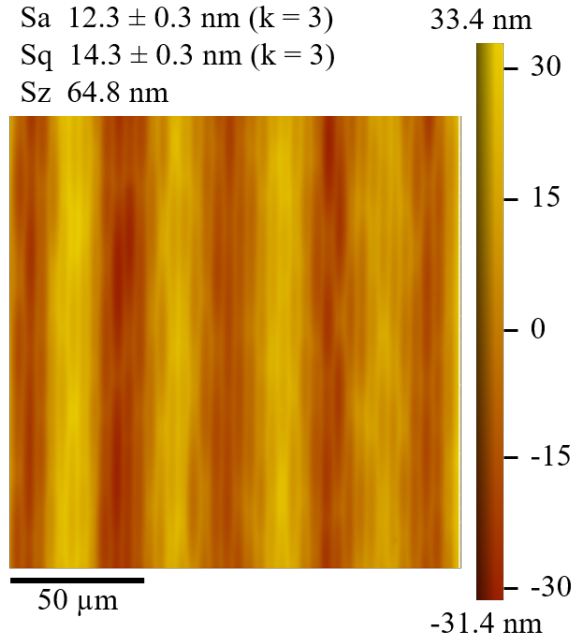
Figure 6.8: Form error from CSI measurement.

6.2   Slow-axis Lens

The SACs included an array of cylinders that spanned the length of the lens. Figure 6.9 shows the SACs lens model. A smaller tool was required for this part, as there little-to-no transition between each cylinder. The SACs lenslet array utilized a 10 μm R in order to minimize the separation of the lenses and maximize the clear aperture/useable optical surface. The axis of symmetry for the cylinder is perpendicular to the length of the lens. Thus, the flycutting direction was programmed to feed perpendicular to the length of the part. A 10μm R with a -25 degree α diamond insert was used on the flycutter arbor. The following sections will discuss the tool path generation and a reporting of the metrology completed on the SACs.
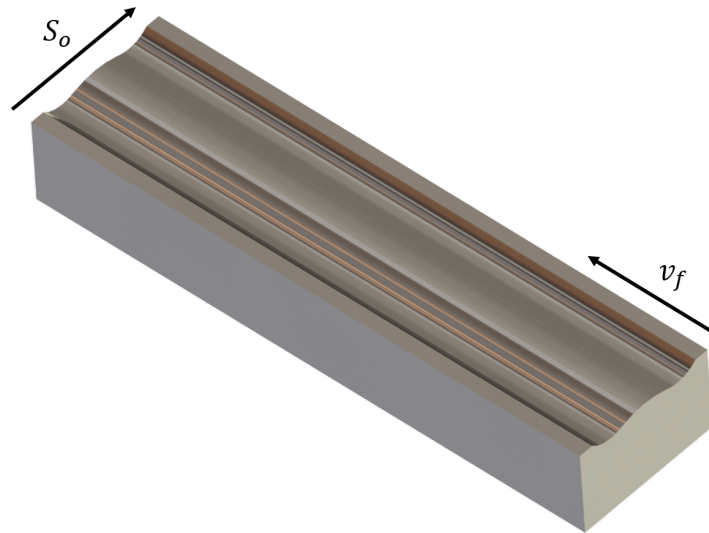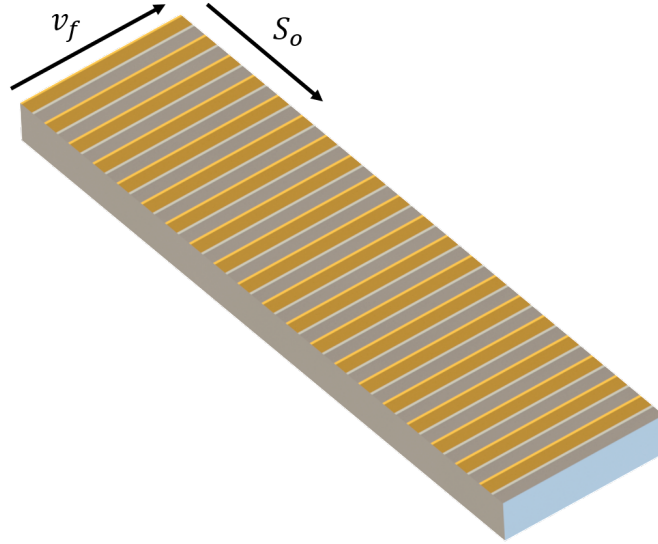
Figure 6.9: Slow-axis lens model.

6.2.1 Tool Path Generation

6.2.1.1 Tool Nose Radius Correction

A test cylinder was machining using the 10 μm R. A small section of the sweep was required on this tool and, therefore, the correction was minimal. The radius confirmation for the test cylinder was verified using the NexView CSI. This was because the arc length of the test cylinder was so small and could not be verified by fitting a circle to the Mahr data. The actual radius of the tool was programmed as 10.02 μm.

6.2.1.2 Tool Path for SACs

6.2.2 Metrology Verification Results

A previously mentioned, the radius of the cylinders that make up the slow-axis surface were verified through a non-contact profilometer. The mean radius of the cylinders was determined to be 1.8295 mm. Figure 6.10 below shows a plot of the distribution of cylinder radius measurements. The mean as compared to the prescribed focal length varies by 0.9 μm.
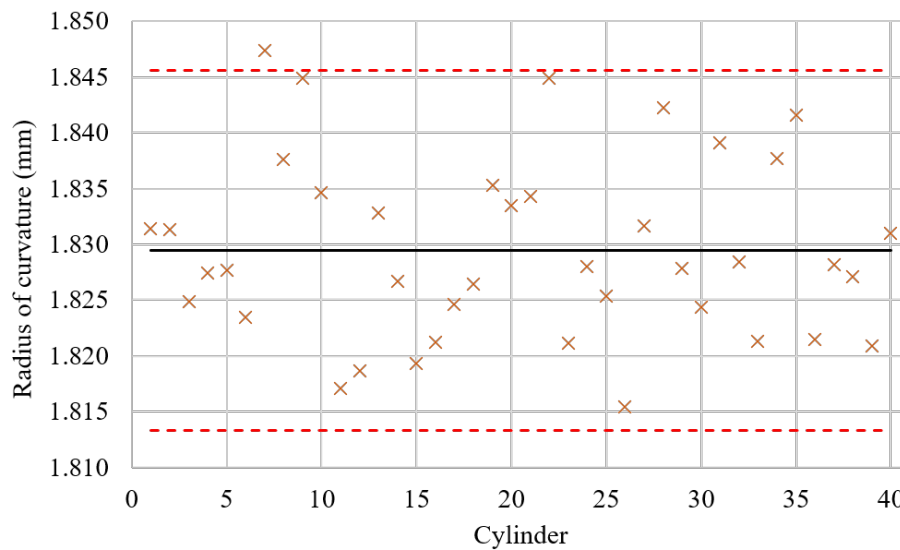
Figure 6.10: Form error from CSI measurement.

Figure 6.11 shows the mean Sq of the slow-axis lens is 16.0 ±0.3 nm (k = 3). There is a waviness feature on the surface that has a period of 16 μm and a PV of approximately 54 nm.
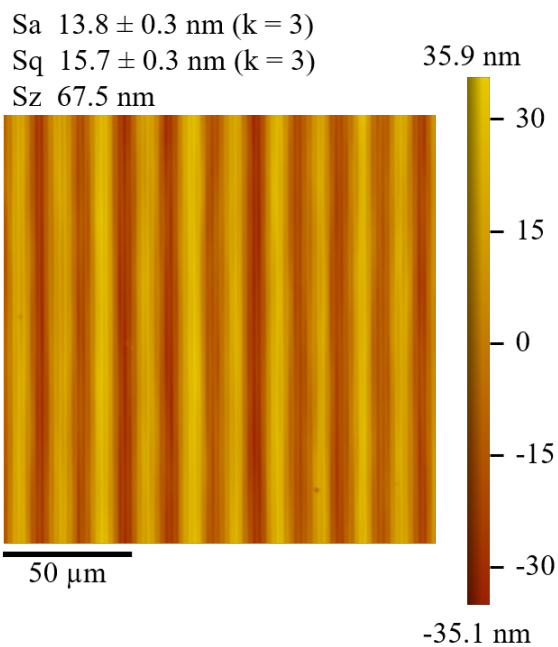
Figure 6.11: Form error from CSI measurement.

CHAPTER 7: CONCLUSIONS

7.1   Uncertainty Analysis Conclusion

The findings from this analysis reported the uncertainty in measuring single-point diamond turned Ge. Recall that the measurand was defined as Sa and Sq. Some of the surfaces had optical quality surface roughness, where others exhibited surface fracture from more aggressive turning parameters. These surfaces were analysed using two STR analysis methods: Method 1 and Method 2. The STR analysis from Method 2 was considered as the best estimate of the uncertainty, as it is the more robust procedure for evaluating the STR for both Sa and Sq. The mean values from Table 2.3 are used in Table 7.1. The reported uncertainty considers k = 3 (99.73 %).

Table 7.1: STR uncertainty analysis summary.

	Mean (nm)	Uncertainty (nm)
$Sa_{SiC-CVD}$	0.1	± 0.3
$Sq_{SiC-CVD}$	0.2	± 0.3
Sa_{Ge-1}	0.3	± 0.3
Sq_{Ge-1}	0.4	± 0.3
$Sa_{Ge-2.1}$	2.7	± 0.3
$Sq_{Ge-2.1}$	3.1	± 0.3
$Sa_{Ge-2.2}$	2.9	± 0.3
$Sq_{Ge-2.2}$	5.0	± 2.4
Sa_{Ge-3}	21.6	± 0.9
Sq_{Ge-3}	47.6	± 2.1

Recall that the target uncertainty was ± 0.5 nm. This was achieved by all surfaces measured using the STR analysis, except for Ge-2.2 and G-3. These two surfaces exhibited surface fracture which drove the uncertainty up in the analysis.

Following this work, Venditti et al. determined that the STR uncertainty analysis varies based on the Sq of the measured surface [53]. The uncertainties included in the height map measurements throughout this dissertation should be considered as an estimate of the total uncertainty in the measurements based on the surface type. They do not reflect what was determined by Venditti et al. [53].

7.2 Diamond Machining of Germanium

7.2.1 Major Crystal Orientation

The findings on the major crystal orientation showed that the Ge with a major crystal orientation of (100) could handle a higher material removal rate ($\sim$2x) than Ge with a (111) crystal orientation. Future work will include an analysis of the subsurface damage using confocal Raman and RBS.

An anonymous survey of several suppliers across the United States summarized that the most common orientation procured was (111). Given the new findings on Ge (100) versus (111), and Ge's (ideally) isotropic optical properties, it would make sense that manufacturers use Ge(100) to optimize machine usage.

7.2.2 Cutting Speed in Turning

The results from the cutting speed V_c study in diamond turning of Ge revealed promising findings. There was an improvement in the surface quality when V_c exceed 10 m/sec. Future work utilizing confocal Raman and RBS will be required to explore the residual damage in the surfaces. It is expected that the deformation zone is decreased at the time of contact over a region is decreased, but it is not clear how much damage remains and how phase transformation occur in each scenario.

7.2.3 Cutting Speed in Flycutting

Insufficient information was gained by the cutting speed study using a flycutting apparatus. It is likely that lower values of V_c should be tests. The exit of the cuts did provide some insight into the damage depth along the chip. Future work is required to understand more into the surface and subsurface.

7.3 Surface Integrity

The results from the surface integrity study concluded that the CMP process developed in this research was near-damage free and was ideal as a base-line for diamond machining experiments. MRF might have shown more promising results had a finer particle size been used in the polishing slurry. Additionally, when no polishing method is readily available, diamond turning with a f_r around 0.3 μm/rev produces a comparable surface quality to CMP.

7.4 Machine Learning Modeling Conclusion

Data-driven machine learning models have become more useful predictive tools as modern computing power has accelerated, and are increasingly part of the data science toolkit for understanding the theory and practice of machining. This research demonstrated the predictive capability of ANN methods and four classic machine learning methods (random forest, decision trees, adaboost, and support vector machines) to predict surface roughness during diamond turning of both Ge and Cu. Both analytical and theoretical models such as finite element analysis (FEA) provide an excellent tool when modeling the plastic flow of ductile materials like Cu, for example during chip production. However, these models have demonstrated shortcomings when modeling brittle materials like Ge that experience fracture or other random material defects during turning. The results presented in this research suggest that both machine learning and ANN methods are capable of addressing these shortcomings.

First, over the range of all eight input parameters studied, f_r, R, α, a_{doc}, V_c, v_f,

t_c and ω, both machine learning and ANN models offer significant improvements in the prediction of surface roughness for Ge when compared against analytical models. These machine learning and ANN models also offer slight improvement over analytical models in predicting surface roughness for Cu. However, the most significant improvements are attained for Ge which is well-known to experience brittle fracture during diamond turning.

Second, and surprisingly given the differences in material structure and dynamics between Ge and Cu, the best performing predictive models for the three ISO standard surface finish parameters Sa, Sq and Sz were identical for both Ge and Cu. Among the ANNs, the 'Deeper' [50-25-12-1] ANN model exhibited the best overall fit with respect to $RMSE$ and R^2 for both Ge and Cu when predicting surface roughness parameter Sa. Similarly, among the classic machine learning models, random forest with max depth 8, adaboost with max depth 11, and random forest with max depth 8 achieved the best accuracies when predicting surface roughness parameters Sa, Sq, and Sz, respectively, for both Ge and Cu.

Finally, this research has yielded several key insights that can inform both future analytical model development for diamond turning and suggest improvements in the selection of turning process parameters, especially for Ge.

Future work will incorporate dynamometer force measurements and surface classification data into machine learning prediction models for Sa, Sq, and Sz.

7.5 Application for Infrared Optics

This work was a collaborative project with Rochester Precision Optics (RPO) Corporation funded by the Air Force Research Laboratory (AFRL) under an STTR-Phase 2 grant extension for contract FA9451-17-C-0424.

Targets for surface roughness and form error (departure from prescription) were 10 nm Sa and ± 300 nm, respectively. Waviness or so-called mid-spatial frequency errors have not yet been specified. However, based on experience, we expect these

errors to be on the order of ±150 nm with a spatial wavelength that is dependent on the cutting parameters. The sources of these errors are thermal and are result from cycles in the machine temperature control systems which have a temporal period of less than 10 minutes.

The final surface roughness of both optics lies above the targeted 10 nm Sa. Though, both the Sa and Sq are below 30 nm, which is more than enough for IR applications. The form errors in the fast-axis lens had a PV of 450 nm, which was below the expect range.
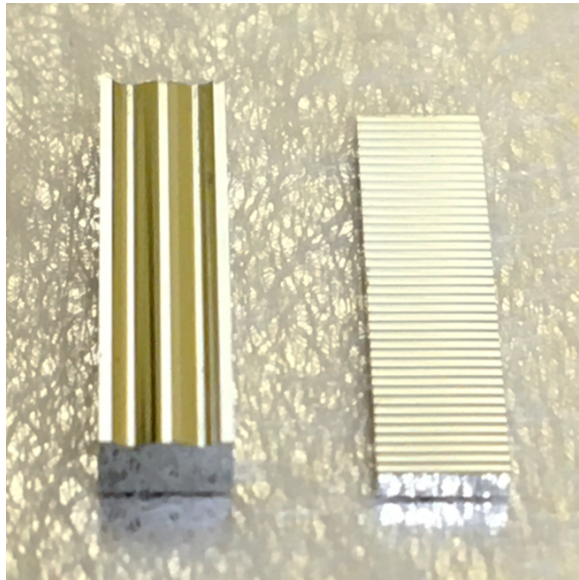
Figure 7.1: Final parts (left) FACs and (right) SACs.

The final parts are shown in Figure 7.1. These were packaged and ship to RPO to anti-reflective coating prior to optical testing at AFRL. The optical testing is on-going.

REFERENCES

[1] O. Riemer, "Advances in ultra precision manufacturing," *Proc. Jpn. Soc. Precis. Eng*, pp. 1–6, 2011.

[2] E. Brinksmeier, B. Karpuschewski, J. Yan, and L. Schönemann, "Manufacturing of multiscale structured surfaces," *CIRP Annals*, pp. 717–739, 2020.

[3] G. Chapman, "Ultra-precision machining systems; an enabling technology for perfect surfaces," *Moore Nanotechnology Systems*, pp. 1–9, 2004.

[4] C. Thomas, "Germanium," tech. rep., U.S. Department of the Interior, U.S. Geological Survey, 2017.

[5] W. P. Shanks III, B. E. Kimball, A. C. Tolcin, and D. E. Guberman, "Germanium and indium," tech. rep., US Geological Survey, 2017.

[6] M. Bosi and G. Attolini, "Germanium: Epitaxy and its applications," *Progress in Crystal Growth and Characterization of Materials*, vol. 56, no. 3-4, pp. 146–174, 2010.

[7] B. Wang, Z. Liu, G. Su, Q. Song, and X. Ai, "Investigations of critical cutting speed and ductile-to-brittle transition mechanism for workpiece material in ultra-high speed machining," *International Journal of Mechanical Sciences*, vol. 104, pp. 44–59, 2015.

[8] R. Neugebauer, K.-D. Bouzakis, B. Denkena, F. Klocke, A. Sterzing, A. Tekkaya, and R. Wertheim, "Velocity effects in metal forming and machining processes," *CIRP annals*, vol. 60, no. 2, pp. 627–650, 2011.

[9] H. Shahinian, J. A. Navare, C. Bodlapati, D. Zaytsev, D. Kang, and D. Ravindra, "High speed ultraprecision machining of germanium," no. November 2019, pp. 59–64, 2019.

[10] J. C. Morris, D. L. Callahan, J. Kulik, J. A. Patten, and R. O. Scattergood, "Origins of the ductile regime in single-point diamond turning of semiconductors," *Journal of the American Ceramic Society*, vol. 78, no. 8, pp. 2015–2020, 1995.

[11] P. N. Blake and R. O. Scattergood, "Ductile-regime turning of germanium and silicon," pp. 1–22, 1989.

[12] D. Lucca, P. Chou, and R. Hocken, "Effect of tool edge geometry on the nanometric cutting of ge," *CIRP Annals*, vol. 47, no. 1, pp. 475–478, 1998.

[13] T. Bifano, P. Blake, T. Dow, and R. Scattergood, "Precision finishing of ceramics," in *Micromachining of Elements with Optical and Other Submicrometer Dimensional and Surface Specifications*, vol. 803, pp. 12–22, International Society for Optics and Photonics, 1987.

[14] K. Liu, X. Li, and S. Liang, "The mechanism of ductile chip formation in cutting of brittle materials," *The International Journal of Advanced Manufacturing Technology*, vol. 33, no. 9-10, pp. 875–884, 2007.

[15] O. Horiuchi, R. Itabashi, Y. Mitoma, H. Shibutani, and H. Suzuki, "Diamond turning of single crystal germanium with an oscillating rotary tool," in *Key Engineering Materials*, vol. 238, pp. 395–398, Trans Tech Publ, 2003.

[16] R. R. Donaldson, C. K. Syn, J. S. Taylor, and R. A. Riddle, "Chip science: Basic study of the single-point cutting process," *Research in the Disciplines*, pp. 49–54, 1986.

[17] R. G. Sparks and M. A. Paesler, "Micro-Raman analysis of stress in machined silicon and germanium," *Precision Engineering*, vol. 10, no. 4, pp. 191–198, 1988.

[18] R. G. Sparks and M. A. Paesler, "Depth profiling of residual stress along interrupted test cuts in machined germanium crystals," *NIST Special Publication*, vol. 891, no. 847, pp. 303–315, 1993.

[19] W. S. Blackley and R. O. Scattergood, "Crystal orientation dependence of machning damage–a stress model," *Journal of the American Ceramic Society*, vol. 73, no. 10, pp. 3113–3115, 1990.

[20] M. F. Ashby, "A first report on deformation-mechanism maps," *Acta Metallurgica*, vol. 20, no. 7, pp. 887–897, 1972.

[21] Y. Furukawa and N. Moronuki, "Effect of material properties on ultra precise cutting processes," *CIRP Annals*, vol. 37, no. 1, pp. 113–116, 1988.

[22] W. Blackley and R. Scattergood, "Ductile-regime machining model for diamond turning of brittle materials," *Precision Engineering*, vol. 13, no. 2, pp. 95–103, 1991.

[23] T. Nakasuji, S. Kodera, S. Hara, H. Matsunaga, N. Ikawa, and S. Shimada, "Diamond Turning of Brittle Materials for Optical Components," *CIRP Annals - Manufacturing Technology*, vol. 39, no. 1, pp. 89–92, 1990.

[24] P. N. Blake and R. O. Scattergood, "Ductile-regime machining of germanium and silicon," *Journal of the American ceramic society*, vol. 73, no. 4, pp. 949–957, 1990.

[25] M. Yoshino, "Effects of External Hydrostatic Pressure on Orthogonal Cutting Characteristics," *Procedia Manufacturing*, vol. 5, pp. 1308–1319, 2016.

[26] W. Blackley and R. O. Scattergood, "Chip topography for ductile-regime machining of germanium," *Journal of Manufacturing Science and Engineering*, pp. 263–266, 1994.

[27] D. J. Oliver, J. E. Bradby, J. S. Williams, M. V. Swain, and P. Munroe, "Rate-dependent phase transformations in nanoindented germanium," *Journal of Applied Physics*, vol. 105, no. 12, pp. 1–3, 2009.

[28] S. Minomura, "Pressure-induced transitions in amorphous silicon and germanium," *Le Journal de Physique Colloques*, vol. 42, no. C4, pp. 181–188, 1981.

[29] G. Pharr, W. Oliver, R. Cook, P. Kirchner, M. Kroll, T. Dinger, and D. Clarke, "Electrical resistance of metallic contacts on silicon and germanium during indentation," *Journal of materials research*, vol. 7, no. 4, pp. 961–972, 1992.

[30] J. E. Bradby, J. S. Williams, J. Wong-Leung, M. V. Swain, and P. Munroe, "Nanoindentation-induced deformation of Ge," *Applied Physics Letters*, vol. 80, no. 15, pp. 2651–2653, 2002.

[31] G. Patriarche, E. Le Bourhis, M. M. Khayyat, and M. M. Chaudhri, "Indentation-induced crystallization and phase transformation of amorphous germanium," *Journal of Applied Physics*, vol. 96, no. 3, pp. 1464–1468, 2004.

[32] J. I. Jang, M. J. Lance, S. Wen, and G. M. Pharr, "Evidence for nanoindentation-induced phase transformations in germanium," *Applied Physics Letters*, vol. 86, no. 13, pp. 1–3, 2005.

[33] M. S. Kiran, T. T. Tran, L. A. Smillie, B. Haberl, D. Subianto, J. S. Williams, and J. E. Bradby, "Temperature-dependent mechanical deformation of silicon at the nanoscale: Phase transformation versus defect propagation," *Journal of Applied Physics*, vol. 117, no. 20, pp. 1–9, 2015.

[34] S. Deshmukh, B. Haberl, S. Ruffell, P. Munroe, J. S. Williams, and J. E. Bradby, "Phase transformation pathways in amorphous germanium under indentation pressure," *Journal of Applied Physics*, vol. 115, no. 15, pp. 1–10, 2014.

[35] F. Campos, N. Mestres, F. Alsina, J. Pascual, E. Morvan, P. Godignon, and J. Millán, "Confocal micro-raman scattering and rutherford backscattering characterization of lattice damage in aluminum implanted 6h–sic," *Diamond and related materials*, vol. 8, no. 2-5, pp. 357–360, 1999.

[36] D. Lucca, C. Wetteland, A. Misra, M. Klopfstein, M. Nastasi, C. Maggiore, and J. Tesmer, "Assessment of subsurface damage in polished ii–vi semiconductors by ion channeling," *Nuclear Instruments and Methods in Physics Research Section B: Beam Interactions with Materials and Atoms*, vol. 219, pp. 611–617, 2004.

[37] J. D. Owen, J. R. Troutman, T. A. Harriman, A. Zare, Y. Q. Wang, D. A. Lucca, and M. A. Davies, "The mechanics of milling of germanium for IR applications," *CIRP Annals - Manufacturing Technology*, vol. 65, no. 1, pp. 109–112, 2016.

[38] C. Claeys and E. Simoen, *Germanium-based technologies: from materials to devices.* Elsevier, 2011.

[39] T. Wuest, D. Weimer, C. Irgens, and K. D. Thoben, "Machine learning in manufacturing: Advantages, challenges, and applications," *Production and Manufacturing Research*, vol. 4, no. 1, pp. 23–45, 2016.

[40] D.-H. Kim, T. J. Kim, X. Wang, M. Kim, Y.-J. Quan, J. W. Oh, S.-H. Min, H. Kim, B. Bhandari, I. Yang, *et al.*, "Smart machining process using machine learning: A review and perspective on machining industry," *International Journal of Precision Engineering and Manufacturing-Green Technology*, vol. 5, no. 4, pp. 555–568, 2018.

[41] Z. Jurkovic, G. Cukor, M. Brezocnik, and T. Brajkovic, "A comparison of machine learning methods for cutting parameters prediction in high speed turning process," *Journal of Intelligent Manufacturing*, vol. 29, no. 8, pp. 1683–1693, 2018.

[42] N. E. Sizemore, M. L. Nogueira, N. P. Greis, and M. A. Davies, "Application of machine learning to the prediction of surface roughness in diamond machining," *Procedia Manufacturing*, vol. 48, pp. 1029–1040, 2020.

[43] N. Trela, H. J. Baker, J. J. Wendland, and D. R. Hall, "Dual-axis beam correction for an array of single-mode diode laser emitters using a laser-written custom phase-plate," *Optics express*, vol. 17, no. 26, pp. 23576–23581, 2009.

[44] T. Possner, B. Messerschmidt, A. Kraeplin, V. Bluemel, B. Hoefer, and P. Schreiber, "Assembly of fast-axis collimating lenses with high-power laser diode bars," in *Optoelectronic Interconnects VII; Photonics Packaging and Integration II*, vol. 3952, pp. 392–399, International Society for Optics and Photonics, 2000.

[45] E. Paul, C. J. Evans, A. Mangamelli, M. L. McGlauflin, and R. S. Polvani, "Chemical aspects of tool wear in single point diamond turning," *Precision Engineering*, vol. 18, no. 1, pp. 4–19, 1996.

[46] X. Zhang and Y. Zhang, "Study on the surface quality of a diamond-turned oxygen-free high-conductance copper reflector used in a high-power co2 laser," *Optical Engineering*, vol. 36, no. 3, pp. 825–830, 1997.

[47] JCGM, "Evaluation of measurement data - guide to the expression of uncertainty in measurement," 2008.

[48] N. E. Sizemore, M. L. Nogueira, N. P. Greis, T. L. Schmitz, and M. A. Davies, "Machine learning model for surface finish in ultra-precision diamond turning," *NIST Advanced Manufacturing Series - $10^{th} Model Based Enterprise Summit, vol. 24, pp. 131 - -139, 2019.$

[49] P. Harris, R. Leach, and C. Giusca, "Uncertainty evaluation for the calculation of a surface texture parameter in the profile case.," pp. 1–51, 2010.

[50] H. Haitjema, "Uncertainty in measurement of surface topography," *Surface Topography: Metrology and Properties*, vol. 3, no. 3, pp. 1–8, 2015.

[51] S. Zahwi, M. Koura, and A. Mekawi, "Factors influencing uncertainty evaluation for surface roughness measurements," in *Proceedings, XVII IMEKO world congress*, pp. 1870–1875, 2003.

[52] P. Montgomery, M. Guellil, P. Pfeiffer, B. Serio, F. Anstotz, L. Pramatarova, and S. Roques, "Challenges in the areal measurement of surface roughness and shape at the micro and nanoscale," in *Journal of Physics: Conference Series*, vol. 558, pp. 1–10, IOP Publishing, 2014.

[53] K. Venditti, "Design for metrology of freeform optics," *The University of North Carolina at Charlotte*, pp. 24–25, 2020.

[54] A. Singh, N. Thakur, and A. Sharma, "A review of supervised machine learning algorithms," in *2016 3rd International Conference on Computing for Sustainable Global Development (INDIACom)*, pp. 1310–1315, IEEE, 2016.

[55] B. C. Love, "Comparing supervised and unsupervised category learning," *Psychonomic bulletin & review*, vol. 9, no. 4, pp. 829–835, 2002.

[56] M. Khalaf, A. J. Hussain, D. Al-Jumeily, T. Baker, R. Keight, P. Lisboa, P. Fergus, and A. S. Al Kafri, "A data science methodology based on machine learning algorithms for flood severity prediction," in *2018 IEEE Congress on Evolutionary Computation (CEC)*, pp. 1–8, IEEE, 2018.

[57] T. Han, D. Jiang, Q. Zhao, L. Wang, and K. Yin, "Comparison of random forest, artificial neural networks and support vector machine for intelligent diagnosis of rotating machinery," *Transactions of the Institute of Measurement and Control*, vol. 40, no. 8, pp. 2681–2693, 2018.

[58] K. H. Raj, R. S. Sharma, S. Srivastava, and C. Patvardhan, "Modeling of manufacturing processes with anns for intelligent manufacturing," *International Journal of Machine Tools and Manufacture*, vol. 40, no. 6, pp. 851–868, 2000.

[59] A. M. Zain, H. Haron, and S. Sharif, "Prediction of surface roughness in the end milling machining using artificial neural network," *Expert Systems with Applications*, vol. 37, no. 2, pp. 1755–1768, 2010.

[60] X. Wang, M. Kang, X. Fu, and C. Li, "Predictive modeling of surface roughness in lenses precision turning using regression and support vector machines," *The International Journal of Advanced Manufacturing Technology*, vol. 87, no. 5-8, pp. 1273–1281, 2016.

[61] N. Gangadhar, H. Kumar, S. Narendranath, and V. Sugumaran, "Fault diagnosis of single point cutting tool through vibration signal using decision tree algorithm," *Procedia Materials Science*, vol. 5, pp. 1434–1441, 2014.

[62] T. Hastie, S. Rosset, J. Zhu, and H. Zou, "Multi-class adaboost," *Statistics and its Interface*, vol. 2, no. 3, pp. 349–360, 2009.

[63] T.-K. An and M.-H. Kim, "A new diverse adaboost classifier," in *2010 International Conference on Artificial Intelligence and Computational Intelligence*, vol. 1, pp. 359–363, IEEE, 2010.

[64] D. Wu, C. Jennings, J. Terpenny, R. X. Gao, and S. Kumara, "A comparative study on machine learning algorithms for smart manufacturing: tool wear prediction using random forests," *Journal of Manufacturing Science and Engineering*, vol. 139, no. 7, pp. 1–9, 2017.

APPENDIX A: SUPPORTING DOCUMENTS

The documents provided here are proof of permission to reuse "Application of machine learning to the prediction of surface roughness in diamond machining" in this dissertation. The contents from this paper are the original source and were used in Chapters 1, 2, 3, 5, and 7. Figures A.1 and A.2 are the supporting documents that state permission for reusing previously copyrighted material.
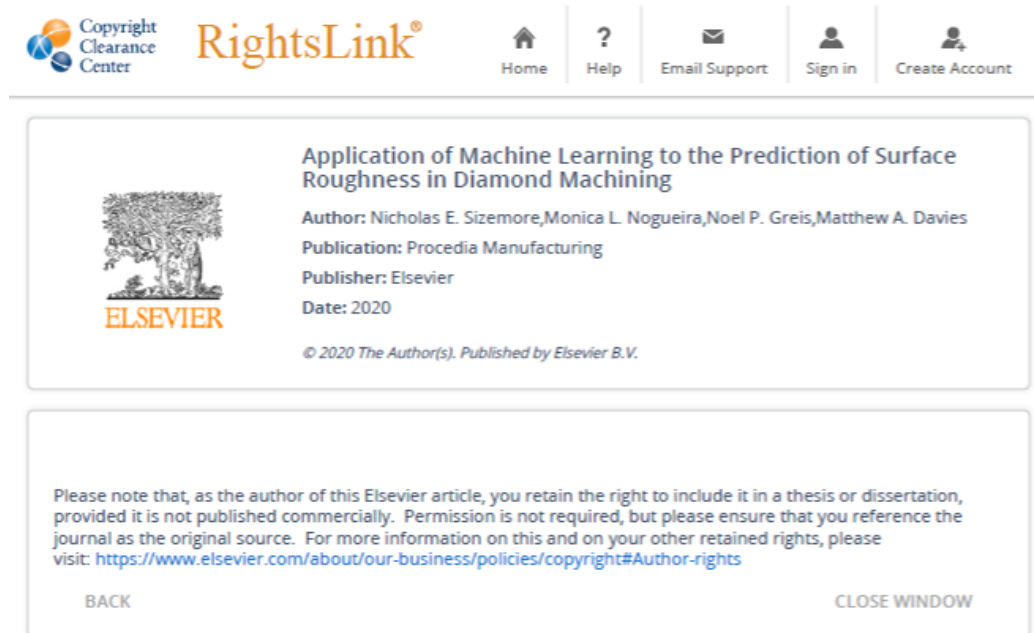
Figure A.1: Science Direct - copyright clearance.

Nicholas Sizemore <nsizemo1@uncc.edu>

Re: ScienceDIrect - Rights for Dissertation [201005-012311]
1 message

US Info <usinfo@elsevier.com>   Mon, Oct 5, 2020 at 10:47 AM
Reply-To: US Info <usinfo@elsevier.com>
To: nsizemo1@uncc.edu

How was our service today? 👍 👎

Dear Dr. Nicholas E. Sizemore,

Thank you for contacting Elsevier Helpdesk.

This e-mail will serve as your reference for the phone conversation regarding: Permission to reuse "*Application of machine learning to the prediction of surface roughness in diamond machining*":

As a summary, Please see image and attached file below for the reference as the author of this Elsevier article, you retain the right to include it in a thesis or dissertation, provided it is not published commercially. Permission is not required, but please ensure that you reference the journal as the original source.

Figure A.2: Science Direct - email confirmation.

APPENDIX B: MATLAB CODE

B.1   Monte Carlo STR Code

```matlab
1  %% Main code
2  %   Nicholas Sizemore
3  %   Dec 2019
4
5  %% This code is for the Mx file type datx
6  % form will be removed
7
8  %%
9  clear all
10 clc
11 close all
12
13 %% Load .dat files
14 addpath(genpath('nans'));
15 addpath(genpath('Files'));
16 % Extracting data
17 h = dir('Files\*.datx');
18
19 for i = 1:1:length(h)
20       pn= h(i).folder;
21       fn = h(i).name;
22       Dswli(i).name = fn(1:end-5);
23       [X,Y,Data] = impData(pn,fn);
24       d(i).phase_data = Data;
25       d(i).X = X*10^6;
26       d(i).Y = Y*10^6;
27 end
28
```

```matlab
29  %% FoV
30  for file = 1:length(d)
31      x = d(file).X;
32      y = d(file).Y;
33      %% Convert to micron
34      z = (d(file).phase_data)*10^6;
35      %% Form removal - plane fitting
36      [FR,GR] = Fit(x,y,z);
37      z_p = FR(x,y);
38      d(file).form = z - z_p;
39      z = d(file).form;
40      Hmap(file).data = z;
41      % surface roughness
42      para(file).Sa = mean(nanmean(abs(z)));
43      para(file).Sq = sqrt(nanmean(z(:).^2));
44      para(file).Sz = max(max(z)) - min(min(z));
45  end
46
47  %% Estimation of surface topography repeatability
48  clc;
49  [STR_Sa_MC, STR_Sq_MC, STR_Sz_MC] = STR_error(Hmap);
50
51  %% Histogram
52  figure()
53  Sa_Hist = histogram(STR_Sa_MC);
54  figure()
55  Sq_Hist = histogram(STR_Sq_MC);
56  figure()
57  Sz_Hist = histogram(STR_Sz_MC);
58
59  %%
60  save('STR_MonteCarlo_result.mat')
```

B.1.1   Function: Importing DATx Files

```matlab
function [X,Y,Data] = impData(pn,fn)
%clear all
%close all

%%
cd DATx_Files;
if isequal(fn,0)
    return
end
filename = [pn '\' fn];
Data = [];
i_Data = [];
cData=[];
qData=[];
info = h5info(filename);
try
    Data = rot90(h5read(filename,..
    '/Measurement/Surface'));
    NanVal = h5readatt(filename,...
    '/Measurement/Surface','No Data');
    x_Convert = h5readatt(filename,...
    '/Measurement/Surface','X Convert');
    y_Convert = h5readatt(filename,...
    '/Measurement/Surface','Y Convert');
    z_Convert = h5readatt(filename,...
    '/Measurement/Surface','Z Convert');
    Data(Data >= NanVal)=NaN;
    switch z_Convert.BaseUnit{:}
        case 'NanoMeters'
```

```matlab
30          zScale = 1e-9;
31      case 'MicroMeters'
32          zScale = 1e-6;
33      end
34      Data = Data*zScale;
35      x_Res = x_Convert.Para{:}(2);
36      y_Res = y_Convert.Para{:}(2);
37      [size_Y,size_X]=size(Data);
38      x=(0:sizeX-1)*x_Res;
39      y=(0:sizeY-1)*y_Res;
40      [Y,X]=ndgrid(y,x);
41      catch
42      disp('No surface data')
43      return
44  end
45  try
46      qData = rot90(h5read(filename,...
47      '/Measurement/Quality'));
48      qNanVal = h5readatt(filename,...
49      '/Measurement/Quality','No Data');
50      qData(qual_Data >= qNanVal)=NaN;
51  catch
52  end
53  try
54      cData = rot90(h5read(filename,...
55      '/Measurement/ColorData'));
56      [sizeY,sizeX]=size(cData);
57
58      r=cData(:,1:3:end);
59      g=cData(:,2:3:end);
60      b=cData(:,3:3:end);
61      cData = zeros(sizeY,sizeX/3,3);
62      cData(:,:,1)=r;
```

```
63      cData(:,:,2)=g;

64      cData(:,:,3)=b;

65      cData = cData/max(max(max(abs(cData))));

66  catch

67  end

68  cd ..

69  end
```

B.1.2   Function: Create Fit

```matlab
1  function [FR,GR] = Fit(x,y,z)
2      % Function to perform Least squares Plane fit
3      [x_Data,y_Data,z_Data] = prepSData(x,y,z);
4      % fit type
5      f = fittype('poly11');
6      % Fit model to data.
7      [FR, GR] = fit([x_Data, y_Data],...
8      z_Data, f, 'Normalize', 'on' );
9  end
```

B.1.3 Function: STR Error

```matlab
1  function [Sa_error_MC,Sq_error_MC,Sz_error_MC]=STR_error(Hmap)
2  % Determines error for Sa, Sq, and Sz
3  [xp,yp] = size(Hmap(1).data);
4  files = length(Hmap);
5  sum_Hmap = zeros(xp,yp);
6  for i = 1:files
7      sum_Hmap = sum_Hmap + Hmap(i).data;
8  end
9  avg_Hmap = sum_Hmap/files; % Average map
10 for i = 1:files
11     z = Hmap(i).data - avg_Hmap; % Difference map
12     diff_Hmap(i).data = z;
13 end
14 for i = 1:10000 % number of iterations for the MC simulation
15     STR_Hmap_MC = zeros(xp,yp);
16     % selects random index for deviation maps
17     temp = randi([1 files]);
18     for j = 1:(xp*yp)
19         STR_Hmap_MC(j) = avg_Hmap(j) +...
20         diff_Hmap(temp).data(j);
21     end
22     Sa_error_MC(i) = mean(nanmean(abs(STR_Hmap_MC)));
23     Sq_error_MC(i) = sqrt(nanmean(STR_Hmap_MC(:).^2));
24     Sz_error_MC(i) = max(max(STR_Hmap_MC)) -...
25     min(min(STR_Hmap_MC));
26 end
27 end
```

B.2   Monte Carlo STR Histogram Code

```matlab
1  %% Histogram Analysis
2  %  Nicholas Sizemore
3  %  Dec 2019
4  %%
5  clc
6  clear all
7  close all
8  %% Define file names
9  files = ["STR_MC_SiC-CVD.mat"; "STR_MC_1umSO.mat";...
10     "STR_MC_10umSO_clocked22p5.mat"; "STR_MC_10umSO.mat";...
11     "STR_MC_25umSO.mat"];
12 names = ["STR MC SiC CVD"; "STR MC 1 um SO";...
13     "STR MC 10 um SO clocked 22.5 wrt <011>";...
14     "STR MC 10 um SO wrt <011>"; "STR MC 25 um SO"];
15 %% Plot histogram
16 n = 15; % number of bins
17 Hscale = 0.005; % scale for X-axis
18 for i = 1:length(files)
19     load(files(i));
20     figure
21     sgtitle(names(i))
22     minSa = min(STR_Sa_MC*1000) - min(STR_Sa_MC*1000)*Hscale;
23     maxSa = max(STR_Sa_MC*1000) + max(STR_Sa_MC*1000)*Hscale;
24     % Sa Plot
25     subplot(2,1,1)
26     histogram(STR_Sa_MC*1000,n,'FaceColor','k',...
27     'EdgeColor','k','FaceAlpha',0.2)
28     pbaspect([1 1 1])
29     set(gca,'LineWidth',1.5,'TickLength',[0.02 0.02]);
```

```matlab
30      set(gca,'FontName','Cambria')
31      xlim([minSa maxSa])
32      ylim([0 5000])
33      xtickformat('%.1f');
34      xlabel('Sa (nm)','FontWeight','bold','FontSize',12)
35      ylabel('Count','FontWeight','bold','FontSize',12)
36      minSq = min(STR_Sq_MC*1000) - min(STR_Sq_MC*1000)*Hscale;
37      maxSq = max(STR_Sq_MC*1000) + max(STR_Sq_MC*1000)*Hscale;
38      % Sq Plot
39      subplot(2,1,2)
40      histogram(STR_Sq_MC*1000,n,'FaceColor','k',...
41      'EdgeColor','k','FaceAlpha',0.2)
42      pbaspect([1 1 1])
43      set(gca,'LineWidth',1.5,'TickLength',[0.02 0.02]);
44      set(gca,'FontName','Cambria')
45      xlim([minSq maxSq])
46      ylim([0 6000])
47      xtickformat('%.1f');
48      xlabel('Sq (nm)','FontWeight','bold','FontSize',12)
49      ylabel('Count','FontWeight','bold','FontSize',12)
50      Mean_Sa(i) = mean(STR_Sa_MC)*1000;
51      Mean_Sq(i) = mean(STR_Sq_MC)*1000;
52      StdDev_Sa(i) = std(STR_Sa_MC)*1000;
53      StdDev_Sq(i) = std(STR_Sq_MC)*1000;
54      Skew_Sa(i) = skewness(STR_Sa_MC);
55      Skew_Sq(i) = skewness(STR_Sq_MC);
56      Kurt_Sa(i) = kurtosis(STR_Sa_MC);
57      Kurt_Sq(i) = kurtosis(STR_Sq_MC);
58  end
```

B.3   Prescription Comparison Code

```matlab
1  %% RPO - Compare prescription to Mahr trace
2  %  Nicholas Sizemore
3  %  July 30, 2020
4
5  %%
6  clc
7  clear all
8  close all
9
10 %% Load data and assign variables
11 load('RawMahr_FA_2.mat')
12 X = RawMahr_FA_1(:,1);
13 Z_Mahr = RawMahr_FA_1(:,2)*1000;
14 X_min = 132.291082; % start of trace
15 X_max = 133.670082; % end of trace
16 jj = find(X>X_min&X<X_max);
17 X_new = X(jj);
18 Z_new = Z_Mahr(jj);
19
20
21 %% Plot raw and prescription data
22 figure(1)
23 plot(X_new,Z_new)
24 xlabel('x (\mum)')
25 ylabel('z (\mum)')
26 hold on
27 grid
28
29 %% Find peak of raw and trim
```

```matlab
30  jj_1 = find(Z_new == max(Z_new));
31  X_new = X_new - X_new(jj_1);
32  figure
33  plot(X_new,Z_new)
34  xlabel('x (\mum)')
35  ylabel('z (\mum)')
36  hold on
37  grid
38  jj_2 = find(X_new>-0.6341&X_new<0.6341);
39  X_new = X_new(jj_2);
40  Z_new = Z_new(jj_2);
41
42  figure
43  plot(X_new,Z_new)
44  xlabel('x (\mum)')
45  ylabel('z (\mum)')
46  hold on
47  grid
48
49  %% Level data
50  p1z = Z_new(1,1);
51  p2z = Z_new(length(Z_new),1);
52  p1x = X_new(1,1);
53  p2x = X_new(length(Z_new),1);
54  X1 = [p1x p2x];
55  Z1 = [p1z p2z];
56  P = polyfit(X1,Z1,1);
57  Zfit = P(1)*X_new;
58  Z_new = Z_new - Zfit;
59
60  figure
61  plot(X_new,Z_new)
62  xlabel('x (\mum)')
```

```matlab
63  ylabel('z (\mum)')
64  hold on
65  grid
66
67  %% Prescription data
68  % This information cannot be provided here
69
70  %% Shift raw data to match prescription
71  Z_new = Z_new-max(Z_new)-25.0;
72
73  figure
74  plot(X_new,Z_new,X_new,Z_Pres)
75  xlabel('x (\mum)')
76  ylabel('z (\mum)')
77  hold on
78  grid
79
80  %% Calculate error
81  diff_Z = Z_Pres-Z_new;
82  Mean_Z_error = mean(diff_Z)
83  Std_Z_error = std(diff_Z)
84
85  figure
86  plot(X_new,diff_Z)
87  xlabel('x (\mum)')
88  ylabel('z (\mum)')
89  hold on
90  grid
```

APPENDIX C: TOOLING FOR APPLICATION

The following sections provide the technical drawings for the FACs and SACs tooling used in testing and manufacturing.

C.1   Fast-axis Lens Tooling

Figure C.1: Fast-axis cutting tool.

C.2 Slow-axis Lens Tooling

Figure C.2: Slow-axis cutting tool.